Available online at www.sciencedirect.com

ScienceDirect

Microporous and Mesoporous Materials 109 (2008) 91–108

MICROPOROUS AND MESOPOROUS MATERIALS

www.elsevier.com/locate/micromeso

Insights into diffusion of gases in zeolites gained from molecular dynamics simulations

R. Krishna [*], J.M. van Baten

Van't Hoff Institute for Molecular Sciences, University of Amsterdam, Nieuwe Achtergracht 166, 1018 WV Amsterdam, The Netherlands

Received 24 February 2007; received in revised form 13 April 2007; accepted 20 April 2007
Available online 3 May 2007

Abstract

The Maxwell–Stefan (M–S) diffusivities Đ_i of a variety of gases (He, Ne, Ar, Kr, H_2, N_2, CO_2, CH_4) in six different all-silica zeolite structures (MFI, AFI, FAU, CHA, DDR, and LTA) have been determined using molecular dynamics (MD) simulations for a range of molar loadings, q_i. In all cases the Đ_i are strongly dependent on q_i. For a given molecule the Đ_i vs. q_i behavior depends on the zeolite structure and can exhibit either a decreasing or increasing trend, dictated by molecular dimensions. For diffusion within the AFI, FAU, and MFI the Đ_i commonly decreases with q_i for all molecules. For zeolites such as CHA, DDR and LTA that consist of cages separated by narrow windows the Đ_i for strongly confined molecules, such as Kr and CH_4, commonly shows an increase with q_i, reaching a maximum before decreasing by a few orders of magnitude as saturation loading is approached.

For binary mixtures, correlation effects cause the more mobile species to be slowed down, and the tardier species to be speeded-up; the Maxwell–Stefan equations provide a convenient framework for quantifying these effects. For a given molecule, correlation effects are dependent on the zeolite structure, pore size and connectivity. Correlation effects are particularly strong in AFI, FAU and MFI; they are relatively weak in LTA, CHA, and DDR because the narrow windows allow the passage of only one molecule at a time. Correlation effects also depend on the degree of confinement within a given zeolite. For weak confinement, as is the case for small molecules such as He, Ne, and H_2, correlation effects are significant even for LTA, CHA and DDR.

Keywords: Zeolites; Molecular dynamics; Maxwell–Stefan diffusivity; Self-diffusivity; Loading dependence; Correlation effects; Mixture diffusion; Gases

---

1. Introduction

Zeolite based adsorption and membrane separation processes are being considered for separation of gaseous mixtures such as CO_2/CH_4, CO_2/N_2, CH_4/N_2, O_2/N_2, CH_4/H_2, and CO_2/H_2. For the development of design of such processes a proper description of diffusion of molecules within zeolites is required and it is generally accepted in the literature that the Maxwell–Stefan (M–S) equations are the most convenient to use in process design [1,2]. In the M–S formulation the flux of any species in a mixture with n components is related to its chemical potential gradient by [3]

$$-\rho\frac{\theta_i}{RT}\frac{\mathrm{d}\mu_i}{\mathrm{d}x} = \sum_{\substack{j=1\\ j\neq i}}^{n}\frac{q_jN_i - q_iN_j}{q_{i,\mathrm{sat}}q_{j,\mathrm{sat}}\text{Đ}_{ij}} + \frac{N_i}{q_{i,\mathrm{sat}}\text{Đ}_i};\quad i = 1,\ldots,n \tag{1}$$

where N_i is the molar flux, ρ is the zeolite framework density, q_i is the molar loading, $q_{i,\mathrm{sat}}$ is the saturation capacity, $\mathrm{d}\mu_i/\mathrm{d}x$ is the chemical potential gradient, R is the gas constant, T is the absolute temperature, Đ_i is the M–S diffusivity, and Đ_{ij} are the binary exchange coefficients. Conformity with the Onsager Reciprocal Relations demands that

$$q_{j,\mathrm{sat}}\text{Đ}_{ij} = q_{i,\mathrm{sat}}\text{Đ}_{ji} \tag{2}$$

In Eq. (1) the fractional occupancies θ_i are defined by

$$\theta_i \equiv q_i/q_{i,\mathrm{sat}}\quad i = 1,2,\ldots,n \tag{3}$$

---

[*] Corresponding author. Tel.: +31 20 257007; fax: +31 20 5255604.
E-mail address: r.krishna@uva.nl (R. Krishna).

1387-1811/$ - see front matter © 2007 Elsevier Inc. All rights reserved.
doi:10.1016/j.micromeso.2007.04.036

Nomenclature

Notation

a_i	constants describing self-exchange in Eq. (11), dimensionless
b_i	constants describing self-exchange in Eq. (11), dimensionless
c_i	molar loading of species *i* based on pore volume, mol m^{-3}
$D_{i,\mathrm{self}}$	self-diffusivity, $m^2\ s^{-1}$
$Đ_i$	Maxwell–Stefan diffusivity of species *i*, $m^2\ s^{-1}$
$Đ_i(0)$	zero-loading M–S diffusivity of species *i*, $m^2\ s^{-1}$
$Đ_{ii}$	self-exchange diffusivity, $m^2\ s^{-1}$
$Đ_{ij}$	binary exchange diffusivity, $m^2\ s^{-1}$
f_i	fugacity of species *i*, Pa
N_i	molar flux of species *i* mol $m^{-2}\ s^{-1}$
n	number of species
q	total mixture loading, mol kg^{-1}
q_i	molar loading of species *i*, mol kg^{-1}
$q_{i,\mathrm{sat}}$	saturation loading of species *i*, mol kg^{-1}
R	gas constant, 8.314 J $mol^{-1}\ K^{-1}$
T	absolute temperature, K
V_p	pore volume, $m^3\ kg^{-1}$
x	spatial distance, m
z	coordination number, dimensionless

Greek letters

β_i	Reed–Ehrlich parameter, dimensionless
Γ_{ij}	thermodynamic factors, dimensionless
δ	thickness of zeolite membrane, m
δE_i	reduction in energy barrier for diffusion, J mol^{-1}
$[\Delta]$	matrix of Maxwell–Stefan diffusivities, $m^2\ s^{-1}$
ε_i	Reed–Ehrlich parameter, dimensionless
ϕ_i	Reed–Ehrlich parameter, dimensionless
θ_i	fractional occupancy of component *i*, dimensionless
μ_i	molar chemical potential, J mol^{-1}
ρ	density of zeolite, kg m^{-3}

Subscripts

i,j	referring to species *i* and *j*
sat	referring to saturation conditions
up	referring to conditions at upstream face of membrane

Vector and matrix notation

( )	$(n-1)$ dimensional column matrix
[ ]	$(n-1)\times(n-1)$ dimensional square matrix

For single component diffusion, Eq. (1) reduces to

$$N_i = -\rho Đ_i \frac{q_i}{RT}\frac{\mathrm{d}\mu_i}{\mathrm{d}x} \quad \text{(unary)} \tag{4}$$

In the literature the pure component $Đ_i$ are also referred to as the "corrected" diffusivity [4]. The major advantage of the M–S formulation is that the $Đ_i$ in both Eqs. (1) and (4) are expected to be the same, opening up the possibility of predicting the diffusion characteristics of *n*-component mixtures on the basis of information on the individual pure components.

In recent years there has been increasing experimental evidence [2,5–10] that the $Đ_i$ are generally strongly dependent on the loading q_i. Recent work of Li et al. [9,10] has demonstrated the need to take account of the loading dependence of the M–S diffusivity $Đ_i$ in interpreting unary and multicomponent permeation of a variety of molecules across a SAPO-34 (an isotype of CHA zeolite) membrane. Their data on the transport coefficient coefficients $(\rho Đ_i/\delta)$, backed out from unary permeation experiments, are presented in Fig. 1 as a function of the loading at the upstream face $q_{i,\mathrm{up}}$. We note from Fig. 1a that for He and H_2 the $(\rho Đ_i/\delta)$ are practically independent of loading. On the other hand, from Fig. 1c we note that for CH_4 there is a four-fold increase of $(\rho Đ_i/\delta)$ with $q_{i,\mathrm{up}}$. The data in Fig. 1b for CO_2, N_2, and Ar shows that the loading dependence of $(\rho Đ_i/\delta)$ is intermediate between that exhibited by (a) He, and H_2, and (c) CH_4.

For the interpretation of membrane permeation experiments and breakthrough curves in adsorptive separations it is desirable to have *a priori* knowledge of the $Đ_i$–q_i relation for any molecule–zeolite combination. The first major objective of the present paper is to gain insights into the $Đ_i$–q_i relation for a variety of gases (He, Ne, Ar, Kr, H_2, N_2, CO_2, CH_4) in six selected all-silica zeolite structures (MFI, AFI, FAU, CHA, DDR, and LTA); these insights are gained by use of molecular dynamics (MD) simulations. The six zeolites have been chosen on the basis of their practical importance. Fig. 2 shows snapshots of the location of a mixture of CO_2 and CH_4 molecules within the *one-dimensional* (1D) channel structure of AFI, *intersecting channels* of MFI, *cages separated by large windows* of FAU, and *cages separated by narrow windows* of LTA, CHA, and DDR. Our second objective is to provide clues on how to *anticipate* the loading dependence for any given guest–host combination based on information on the molecular configuration and dimensions along with zeolite structural details. Table 1 gives the characteristic sizes of channels or windows for zeolite structures. Fig. 3 presents cartoons showing approximate molecular dimensions of the gases investigated in this work; these dimensions were estimated using published force fields for molecule-molecule interactions [11–15]. The indicated dimensions are only used in a *qualitative* sense in the discussions below.

Mixture diffusion is strongly influenced by the binary exchange coefficients $Đ_{ij}$ in Eq. (1); these coefficients reflect

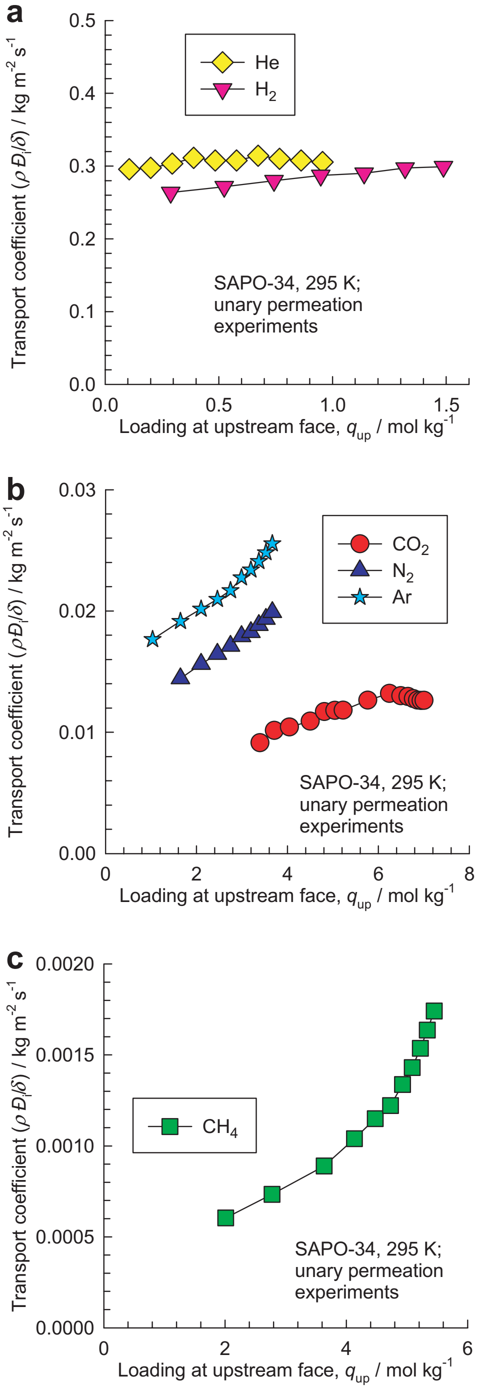

Fig. 1. Pure component transport coefficients, $\rho Đ_i/\delta$, for (a) He, H_2, (b) CO_2, N_2, Ar, and (c) CH_4 for transport across SAPO-34 membrane. The data is taken from Li et al. [9,10].

correlation effects which cause slowing-down of the more mobile species and speeding-up of the tardier ones. Our third major objective is to gain insights, using MD simulations, into the mixture diffusion characteristics of various zeolites.

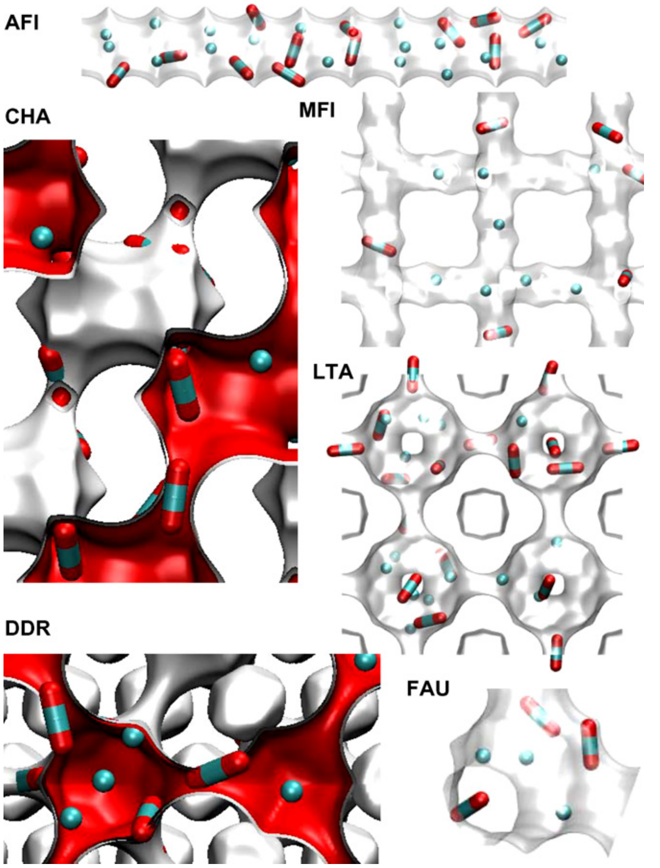

Fig. 2. Snapshots of the location of a mixture of CO_2 and CH_4 molecules within the *one-dimensional* channel structure of AFI, *intersecting channels* of MFI, *cages separated by large windows* of FAU, and *cages separated by narrow windows* of LTA, CHA, and DDR. Note that the zeolites are not all drawn to the same scale.

Table 1
Characteristic sizes of channels or windows for zeolite structures

Zeolite	Channel or window size/Å
MFI	10 T-ring intersecting channels of 5.1–5.6 Å size
AFI	12 T-ring 1D channels of 7.3 Å size
FAU	12 T-ring window of 7.4 Å size
LTA	8 T-ring window of 5 Å size
CHA	8 T-ring window of 3.8 Å size
DDR	8 T-ring window of 3.6–4.4 Å size

The MD simulation methodology, including a description of the force field, is given in Supplementary material, that includes the complete set of information on the adsorption isotherms, required for estimation of the saturation loadings, $q_{i,\text{sat}}$, along with snapshots showing the location of the molecules. A selection from the complete set of diffusivity data, for pure components and for mixtures presented in Supplementary material, is discussed below to draw a range of conclusions.

2. Loading dependence of the M–S diffusivity

Fig. 4 summarizes the MD simulation results for $Đ_i$ of the eight different gases in the six chosen zeolites. For discussion purposes we define the “degree of confinement” as the ratio of a characteristic size of the molecule with respect to the characteristic pore, or window, size of the zeolite as

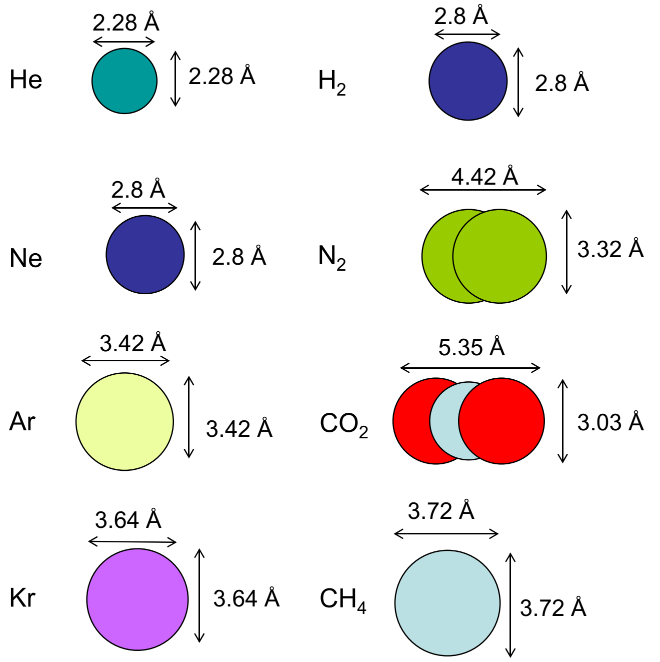

Fig. 3. Cartoon showing the approximate molecular dimensions of He, Ne, Ar, Kr, H_2, N_2, CO_2, and CH_4. The molecular diameters are estimated on the basis of the Lennard-Jones size parameters σ for molecule–molecule interactions. The molecular lengths are estimated on the basis of the bond lengths.

specified in Table 1. For "spherical" molecules the characteristic size is the diameter, as indicated in Fig. 3. For diffusion of linear molecules such as CO_2 and N_2 through narrow windows of CHA, LTA, and DDR the molecular diameter is again the relevant characteristic size in view of the fact that the molecular lengths are larger than the window openings (see Fig. 2). For diffusion of CO_2 and N_2 inside large pore and medium pore zeolites (AFI, FAU and MFI), the molecular length is also a consideration and the concept of molecular "size" becomes a tenuous concept.

Small molecules such as He, H_2, and Ne, having molecular diameters smaller than 2.8 Å are very weakly confined in all the zeolites investigated. The M–S diffusivity $Đ_i$ can be expected to be substantially independent of the molar loading q_i; the results presented in Fig. 4a–c confirm this expectation. The hierarchy of $Đ_i$ values in the various zeolites is dictated by the size of the channels or windows. Fig. 4d–h presents the simulation results for molecules with increasing degree of confinement: CO_2, N_2, Ar, Kr, and CH_4. The stronger the degree of confinement the more severe is the $Đ_i$–q_i dependence. The diffusivities of CO_2, N_2, Ar, Kr, and CH_4 in AFI, FAU, and MFI decrease with increasing loading in a nearly monotonous fashion. The $Đ_i$–q_i relation of N_2, Ar, Kr, and CH_4 in LTA, CHA, and DDR that consists of cage structures separated by narrow windows is particularly noteworthy; in all cases the $Đ_i$–q_i relation exhibits a maximum. This maximum is not observed for CO_2 in LTA, CHA and DDR because the inter-cage hopping rate of CO_2 molecules is dictated by the molecular diameter, and not the molecular length; CO_2 has only a slightly larger molecular diameter than Ne. For CO_2, N_2, Ar, Kr, and CH_4, the hierarchy of the *zero-loading* $Đ_i(0)$ values are dictated by the size of the channels or windows and follows the sequence: AFI, FAU, MFI, LTA, CHA and DDR.

For AFI, FAU, and MFI, Fig. 5a–c compares $Đ_i$–q_i relation for different gases. Generally speaking, for each of these zeolites, the severity of the loading dependence of $Đ_i$ increases with the size of the molecules. At saturation capacity $q_{i,\mathrm{sat}}$ the $Đ_i$ approaches near-zero values; the saturation capacities $q_{i,\mathrm{sat}}$ are determined from Grand Canonical Monte Carlo (GCMC) simulations of adsorption isotherms that are presented in Supplementary material accompanying this publication.

Consider diffusion within the 1D channels of AFI; see Fig. 5a. The diffusivities of He, H_2 and Ne are practically independent of loading, at least up to the range of loadings considered, i.e. $q_i < 5\ \mathrm{mol\ kg^{-1}}$. The saturation capacities of He, H_2 and Ne are too large to attain in practice under realistic operating pressures and that is the reason that their $Đ_i$ appear to be loading independent. For Ar and CH_4 diffusion in AFI the $Đ_i$–q_i relation closely mirrors that of $1/\Gamma_i$ vs. q_i, where Γ_i is the thermodynamic factor:

$$\Gamma_i \equiv \frac{\mathrm{d}\ln f_i}{\mathrm{d}\ln q_i} \tag{5}$$

as is evidenced in Fig. 6a and b. The inflection in the $Đ_i$–q_i relation has its origins in the corresponding inflection in the $1/\Gamma_i$ vs. q_i data [16]. An important consequence of the results presented in Fig. 5a is that the Fick diffusivity D_i, that is a product of $Đ_i$ and Γ_i, is loading independent. There is no experimental evidence available as yet to test this conclusion.

The $Đ_i$–q_i behavior in FAU (cf. Fig. 5b), that consists of cages separated by large 7.4 Å windows, is analogous to that within AFI. The inflection in the CH_4 diffusivity in FAU corresponds to that of $1/\Gamma_i$ vs. q_i; see Fig. 6c. Though the $Đ_i$–q_i behavior in MFI (cf. Fig. 5c) is *qualitatively* similar to that within AFI and FAU, the $Đ_i$ appears to decrease less sharply with q_i, at least for low loadings, than in the AFI and FAU topologies.

In the context of separating CO_2/CH_4 mixtures exploiting diffusivity differences [17] we note that in CHA and DDR the $Đ_i$ of CO_2 is higher than that of CH_4; see Fig. 4e and f. The reason for this is that the inter-cage hopping rates are dictated by the molecular diameters, as pictured in Fig. 2. However, in FAU and MFI the $Đ_i$ of CH_4 is higher than that of CO_2; apparently the molecular length also plays a role in determining the diffusivity hierarchy in medium and large pore size structures.

The $Đ_i$–q_i behavior in zeolite structures CHA, DDR and LTA that consist of cages separated by *narrow* windows requires a different explanation and analysis. The most convenient and practical physical model to quantify the $Đ_i$–q_i relation is that developed by Reed and Ehrlich for surface diffusion of adsorbed molecules [18]. In the Reed

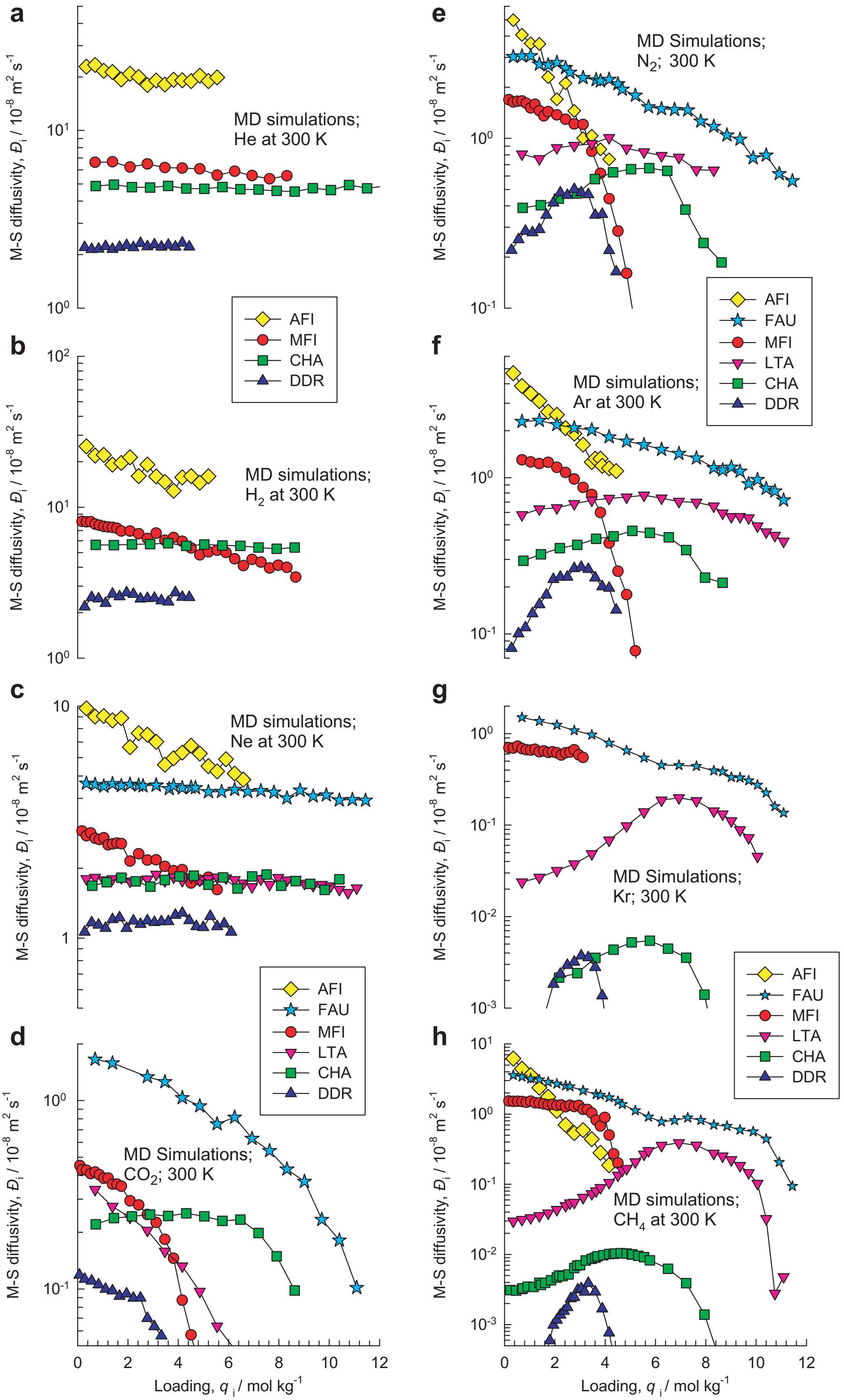

Fig. 4. M–S diffusivity $Đ_i$ of He, H$_2$, Ne, CO$_2$, N$_2$, Ar, Kr, and CH$_4$ in different zeolites as a function of the molar loading q_i.

and Ehrlich model, as applied earlier by Krishna and van Baten [3] for zeolites, the intermolecular interactions *within* a cage is assumed to influence the hopping frequencies of molecules *between* cages, by a factor $\phi_i = \exp\left(\frac{\delta E_i}{RT}\right)$, where

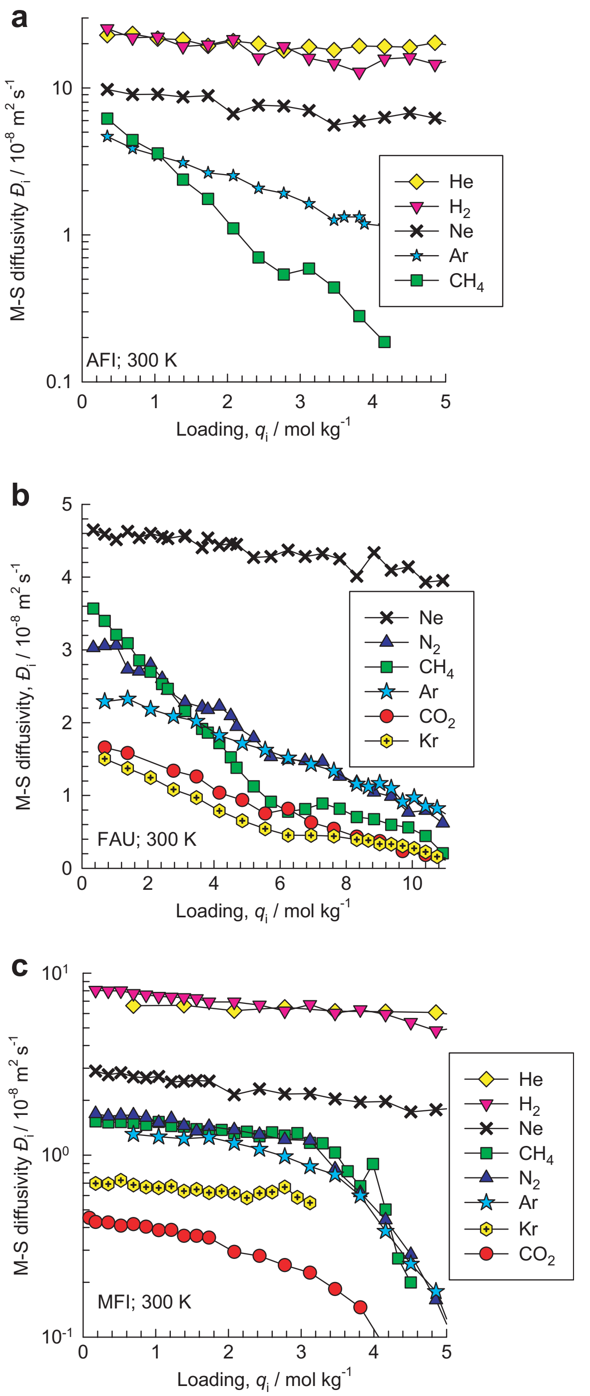

Fig. 5. M–S diffusivity $Đ_i$ of different gases in AFI, FAU, and MFI as a function of the molar loading q_i.

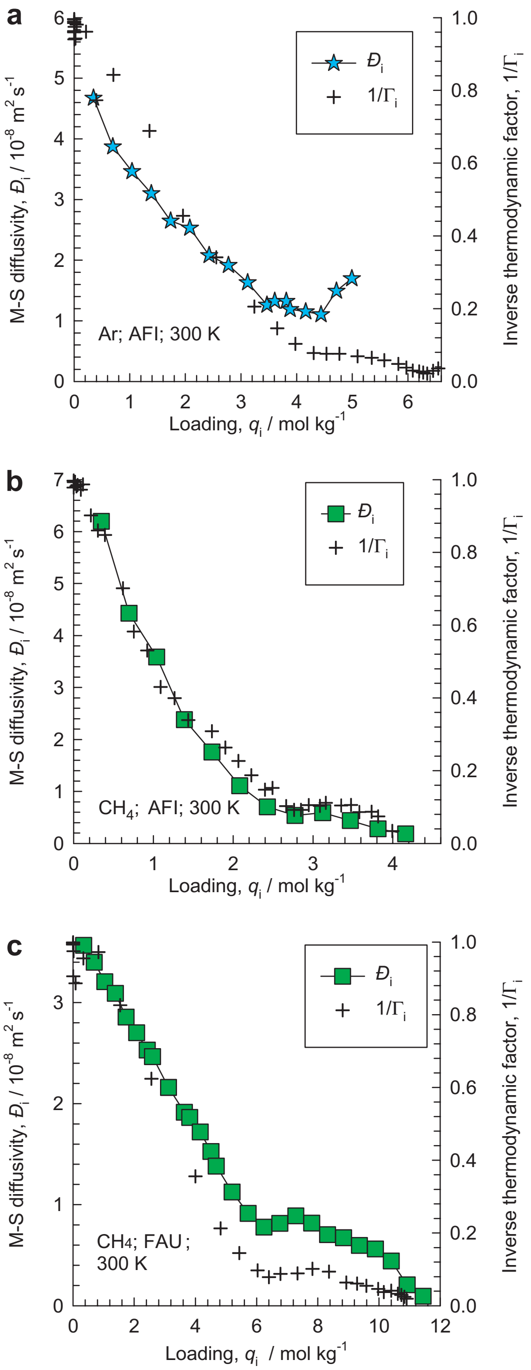

Fig. 6. Comparison of the loading dependence of $Đ_i$ with that of the inverse thermodynamic factor, $1/\Gamma_i$, for (a) Ar in AFI, (b) CH_4 in AFI, and (b) CH_4 in FAU. The Γ_i data are obtained from the GCMC simulations using the Reed and Ehrlich fluctuation formula [16].

δE_i represents the reduction in the energy barrier for diffusion. The values of δE_i can be estimated from molecular simulations of the free energy profiles [19,20]. The Reed and Ehrlich model leads to the following expression for the M–S diffusivity as a function of the fractional occupancy, θ_i:

$$Đ_i = Đ_i(0)\frac{(1+\varepsilon_i)^{z-1}}{(1+\varepsilon_i/\phi_i)^{z}} \tag{6}$$

where z is the coordination number, representing the maximum number of nearest neighbors within a cage. From an engineering point of view the precise choice of the value of z is not crucial, as the *combination* of z and ϕ_i prescribes the loading dependence. For both CHA and DDR we choose a value $z = 5$ for all molecules. The other parameters are defined as follows (see [3,21] for more detailed discussions and derivations)

$$\varepsilon_i = \frac{(\beta_i - 1 + 2\theta_i)\phi_i}{2(1-\theta_i)}; \quad \beta_i = \sqrt{1 - 4\theta_i(1-\theta_i)(1-1/\phi_i)} \tag{7}$$

The MD simulated $Đ_i$ values for various molecules in CHA and DDR are used to fit ϕ_i; the fitted values are reported in Table 2. The continuous solid lines in Figs. 7 and 8 represent the calculations following Eq. (6) with the fitted parameter values.

Firstly, we note that the $Đ_i$–q_i data for CHA in Fig. 7 shows remarkable similarities with the loading dependence of the transport coefficient $\rho Đ_i/\delta$ across a SAPO-34 membrane presented in Fig. 1. The experiments were not, however, conducted with high enough $q_{i,\mathrm{up}}$ values to exhibit the maxima observed by MD for N_2, Ar, and CH_4. Nonetheless, MD simulations provide a good *qualitative* guide to the description of the loading dependence of $Đ_i$. The actual diffusivity values are, however, very sensitive to the Lennard-Jones parameters representing atom–atom and atom–zeolite interactions. In order to illustrate this we carried out a sensitivity analysis on the influence of the Lennard-Jones size parameters on the $Đ_i$ of Ar in CHA. The values of $\sigma_{\mathrm{Ar-Ar}} = 3.42$ Å and $\sigma_{\mathrm{Ar-zeo}} = 3.17$ Å were subject to a 10% increase or decrease; the results are presented in Fig. 9a and b. These perturbations in the $\sigma_{\mathrm{Ar-Ar}}$ and $\sigma_{\mathrm{Ar-zeo}}$ parameters also result in different isotherm behaviors; the GCMC simulated isotherms are presented alongside in Fig. 9c and d. The $Đ_i$–q_i dependence is severely affected by both $\sigma_{\mathrm{Ar-Ar}}$ and $\sigma_{\mathrm{Ar-zeo}}$. Increasing either $\sigma_{\mathrm{Ar-Ar}}$ or $\sigma_{\mathrm{Ar-zeo}}$ results in increased severity of the dependence of $Đ_i$ on q_i, leading to a sharper maximum. There is also a significant corresponding decrease in the saturation capacity, $q_{i,\mathrm{sat}}$. The 10% increase in $\sigma_{\mathrm{Ar-zeo}}$ results in a reduction of the $Đ_i$ values by two orders of magnitude; this emphasizes the difficulty of obtaining good *quantitative* agreement between MD simulations and experimental diffusivity data as the Lennard-Jones parameters are invariably fitted to *equilibrium* adsorption data. Decreasing either $\sigma_{\mathrm{Ar-Ar}}$ or $\sigma_{\mathrm{Ar-zeo}}$ results in an increase in the satura-

Table 2
Reed–Ehrlich parameters for variety of molecules in different zeolites

Zeolite	Molecule	Saturation capacity, $q_{i,\mathrm{sat}}$/ mol kg^{-1}	$Đ_i(0)$/ 10^{-8} m^2 s^{-1}	z	ϕ_i
CHA	He	41.6	4.8	5	1.26
CHA	H_2	31.9	5.71	5	1.23
CHA	Ne	27.7	1.74	5	1.31
CHA	CO_2	9.71	0.21	5	1.47
CHA	N_2	9.71	0.274	5	$2.74\exp(-0.6\theta_i)$
CHA	Kr	8.32	2.7×10^{-3}	5	$3.45\exp(-0.72\theta_i)$
CHA	Ar	9.71	0.285	5	1.64
CHA	CH_4	8.32	2.1×10^{-3}	5	$4.55\exp(-0.98\theta_i)$
DDR	He	15	3.17	5	1.36
DDR	H_2	12	2.4	5	1.36
DDR	Ne	14	1.1	5	$1.46\exp(-0.2\theta_i)$
DDR	CO_2	4.58	0.113	5	1.19
DDR	N_2	4.58	0.2	5	1.94
DDR	Ar	5.5	0.076	5	$3.26\exp(-0.65\theta_i)$
DDR	CH_4	4.16	4.76×10^{-5}	5	$6\exp(-0.2\theta_i)$
DDR	Kr	4.16	1.15×10^{-4}	5	$5.97\exp(-0.47\theta_i)$
AFI	Ne	16	9.9	2	0.73
AFI	Ar	6.6	5.1	2	0.56
MFI	Ne	20	2.94	2.5	0.68
MFI	Ar	6	1.15	2.5	$3.36\exp(-1.54\theta_i)$
FAU	Ne	34	4.64	5	1.17
FAU	Ar	15	2.44	5	1.04
LTA	Ne	34.7	1.83	5	1.22
LTA	Ar	12.5	0.58	5	1.53

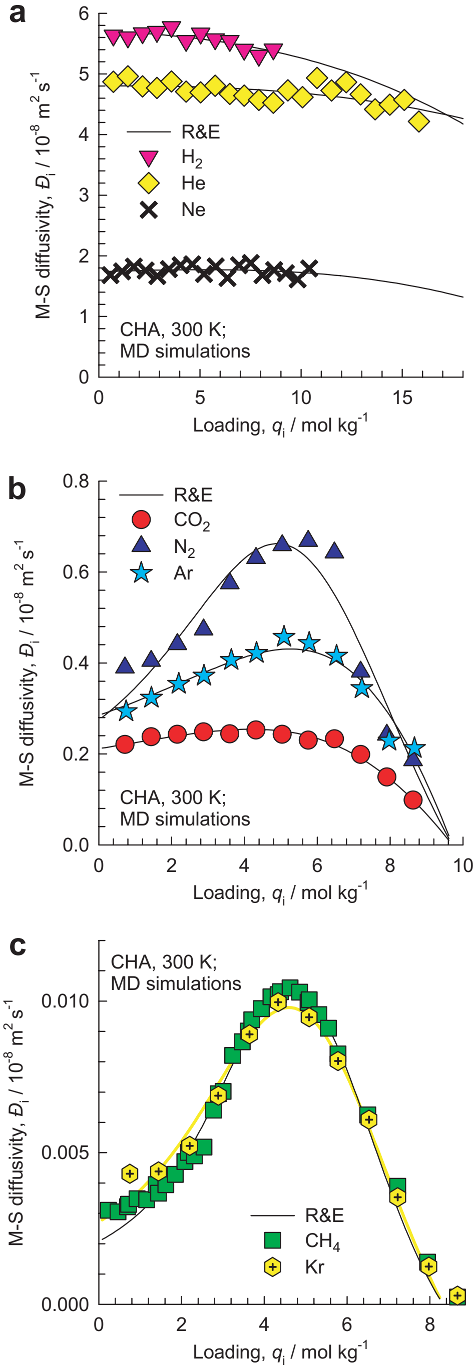

Fig. 7. M–S diffusivity $Đ_i$ in CHA of (a) He, H_2, Ne, (b) Ar, CO_2, N_2, and (c) Kr, CH_4. The continuous solid lines represent the Reed and Ehrlich model fits of the data with parameters specified in Table 2.

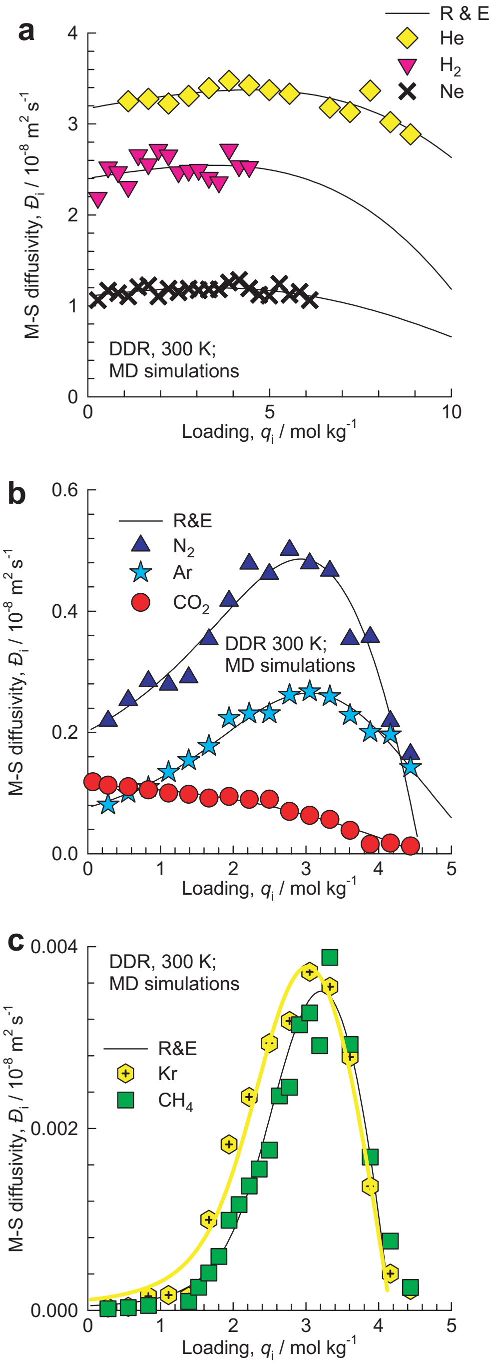

Fig. 8. M–S diffusivity $Đ_i$ in DDR of (a) He, H_2, Ne, (b) Ar, CO_2, N_2, and (c) Kr, CH_4. The continuous solid lines represent the Reed and Ehrlich model fits of the data with parameters specified in Table 2.

tion capacity, $q_{i,\mathrm{sat}}$, and leads to a milder dependence of $Đ_i$ on q_i. The 10% decrease in $\sigma_{\mathrm{Ar-zeo}}$, for example, causes the maximum in the $Đ_i$–q_i relation to nearly disappear.

We shall now attempt to rationalize the fitted Reed and Ehrlich parameter values for CHA. The values of the zero-loading diffusivities $Đ_i(0)$ appear to decrease sharply as the molecular diameter approaches the window size, which has a value of 3.8 Å; see Fig. 10a. For N_2 and CO_2, the $Đ_i$ appear to decrease with increasing molecular *length*; see Fig. 10b. The ϕ_i reflects the severity of the loading dependence; a larger value will lead to a sharper increase in the $Đ_i$ with occupancy. The ϕ_i also appears to correlate with the molecular diameter; see Fig. 10c. The stronger the confinement within the windows of CHA, the stronger is the loading dependence of the M–S diffusivity. For an interpretation of the loading dependence of the $Đ_i$ in terms of the free energy barrier for hopping of molecules between cages see the papers of Beerdsen et al. [19,20]. It is interesting to note that Li et al. [9] have interpreted their experimental data on transport coefficients in a similar manner and arrive at the same conclusions.

The Reed and Ehrlich parameter fits for DDR can be rationalized in an analogous manner; see Fig. 11a–c. The windows in DDR are elliptic in shape with the smallest dimension of 3.6 Å. Therefore, a molecule is more strongly confined within DDR than within CHA. This leads to significantly *lower* $Đ_i(0)$ values and, generally speaking, a *higher* ϕ_i as compared to the corresponding values for CHA.

The $Đ_i$ data of Ne, N_2, Ar, CH_4, and Kr in LTA can be fitted with the Reed and Ehrlich model in a manner similar to that described above for CHA and DDR; these fits are shown in Fig. 12a. The maxima in the $Đ_i$ vs. q_i data for CH_4, and Kr are particularly noteworthy.

Within the framework of a quasi-chemical mean-field approximation, Reed and Ehrlich [18] have derived the following expression relating the thermodynamic factor Γ_i to the parameters z, and β_i

$$\Gamma_i = \frac{1}{(1-\theta_i)}\left(1+\frac{z}{2}\frac{(1-\beta_i)}{\beta_i}\right) \tag{8}$$

Papadopoulos et al. [8] have used this expression to estimate the parameter δE_i from GCMC simulations of isotherms. We subjected Eq. (8) to a test for the system Ar/CHA at 300 K. From the GCMC simulated isotherm, shown in Fig. 13a along with dual-site Langmuir fit, we calculated Γ_i by differentiation of the isotherm using Eq. (5). The isotherm has an inflection point, and this is reflected in the Γ_i. These results are compared to the values calculated from Eqs. (7) and (8) along with the fits in Table 2; see Fig. 13b. The agreement between the two *independent* calculation methods for Γ_i is reasonably good. This suggests that the GCMC equilibrium q_i vs. f_i simulations and the MD $Đ_i$ vs. q_i simulations complement each other. Backing out the parameter ϕ_i from Eq. (8) and the fitted isotherm yields a variation of ϕ_i with q_i as indicated by the dashed line in Fig. 13c. Direct fitting of the MD simulated the $Đ_i$ yields a constant value of $\phi_i = 1.64$, that is within the range of values backed out from the isotherm fit. This indicates that Eq. (8) provides an alternative method for estimating ϕ_i. Further investigations are required to determine the accuracy of this method in practice.

3. Self-diffusivity and self-exchange coefficients

In several experimental studies, the self-diffusivity ($D_{i,\mathrm{self}}$) data are found to be loading dependent. The exper-

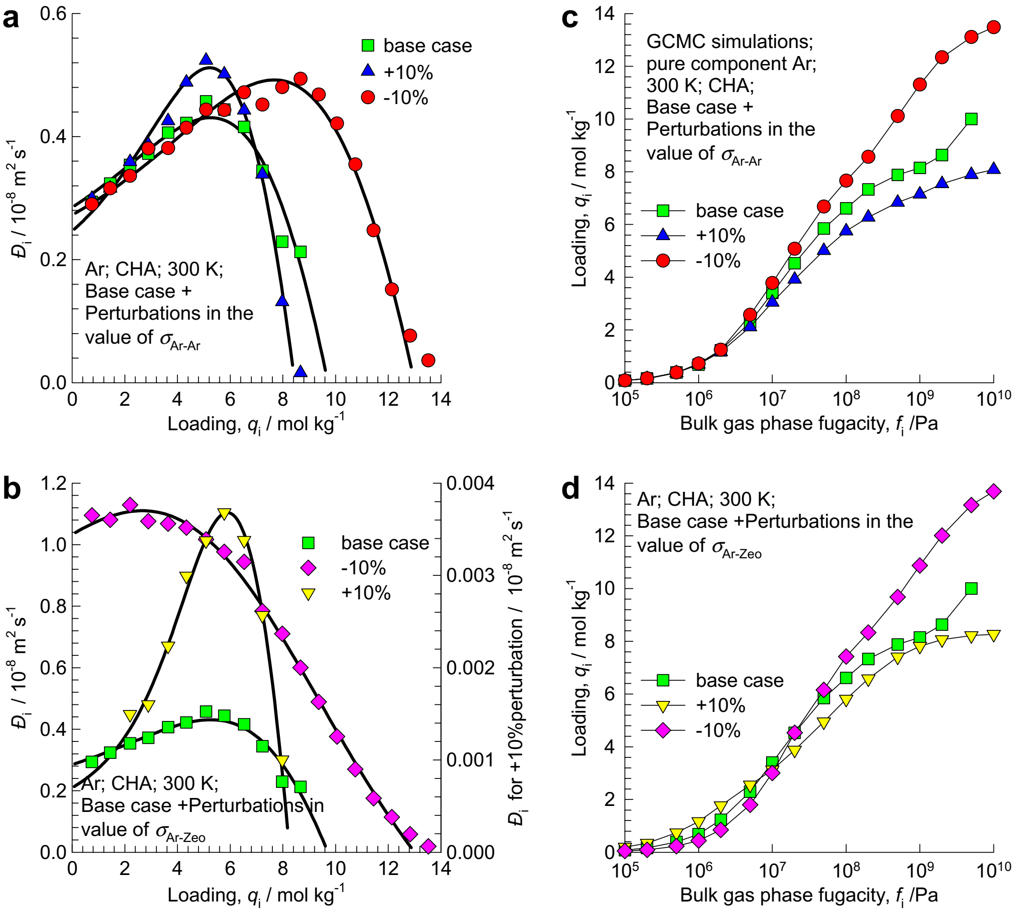

Fig. 9. Sensitivity of MD simulation results of the M–S diffusivity $Đ_i$ of Ar in CHA to the perturbations in the Lennard-Jones size parameters $\sigma_{\mathrm{Ar-Ar}}$ and $\sigma_{\mathrm{Ar-zeo}}$. (a) Results for 10% increase or decrease in $\sigma_{\mathrm{Ar-Ar}}$, and (b) 10% increase or decrease in $\sigma_{\mathrm{Ar-zeo}}$. For the base case the Lennard-Jones size parameters are $\sigma_{\mathrm{Ar-Ar}} = 3.42$ Å and $\sigma_{\mathrm{Ar-zeo}} = 3.17$ Å. The continuous solid lines in (a) and (b) reprint fits with the Reed and Ehrlich model. Sensitivity of the adsorption isotherms of Ar in CHA to the perturbations in the Lennard-Jones size parameters $\sigma_{\mathrm{Ar-Ar}}$ and $\sigma_{\mathrm{Ar-zeo}}$ are shown in (c) and (d).

imental data of Cao et al. [22] for the $D_{i,\mathrm{self}}$ of N_2, CH_4, and Kr in LTA-4A, show that while the $D_{i,\mathrm{self}}$ of N_2 is practically constant for the loading range $0 < q_i < 1.5$ mol kg^{-1}, the $D_{i,\mathrm{self}}$ for CH_4 and Kr show an increasing trend with q_i. Cao et al. [22] state in their paper "No clear explanation of these behaviors can be given at this time". To rationalize the experimental data we have plotted in Fig. 12b the MD simulated $D_{i,\mathrm{self}}$ for various gases in LTA as a function of loading. We note the sharp increase in the $D_{i,\mathrm{self}}$ of CH_4, and Kr in the range $0 < q_i < 6$ mol kg^{-1}, consistent with the experimental observations. Also in agreement with the experiments, MD simulations show that the $D_{i,\mathrm{self}}$ for N_2 is practically constant for loadings below 3 mol kg^{-1}.

PFG NMR measurement data of Caro et al. [23] for diffusivity of CH_4, C_2H_6, and C_3H_8 also confirms the increasing trend of $D_{i,\mathrm{self}}$ with q_i for LTA-5A zeolite. Interestingly, for FAU (NaX) and MFI zeolites, the experimental data of Caro et al. show that $D_{i,\mathrm{self}}$ for the three alkanes *decreases* with q_i. Let us compare the loading dependence of MD simulated $D_{i,\mathrm{self}}$ of CH_4 in the FAU, MFI and LTA. For a fairer comparison of different zeolites we plot $D_{i,\mathrm{self}}$ against c_i, defined as

$$c_i = q_i/V_\mathrm{p} \tag{9}$$

where V_p is the pore volumes; its value is estimated as 22.7, 8.3, and 20.3×10^{-5} m^3 kg^{-1}, respectively for FAU, MFI, LTA; see Fig. 14. Also included are the $D_{i,\mathrm{self}}$ data for pure liquid CH_4 at different densities [24,25]. The first point to note is that even for pure liquid $D_{i,\mathrm{self}}$ decreases with c_i and therefore, there is no reason to expect $D_{i,\mathrm{self}}$ within zeolites to be independent of loading. A further point to note with increased loading, the $D_{i,\mathrm{self}}$ in all zeolites approach one another and appear to follow the same asymptotic trend dictated by that of $D_{i,\mathrm{self}}$ in the pure fluid. Due to stronger confinement of CH_4 in LTA than in MFI and FAU, a sharp maximum is detected. The comparative trends $D_{i,\mathrm{self}}$–c_i trends for MFI, FAU and LTA are in qualitative agreement with the experiments of Caro et al. [23]. A further point to be noted from Fig. 14 is that at the highest loadings the $D_{i,\mathrm{self}}$ reduces to a value that is about two orders of magnitude lower than that of pure liquid. In the Reed and Ehrlich model discussed in the foregoing section, the diffusivity reduces to zero at $q_{i,\mathrm{sat}}$. In reality there is a reduction by a few orders of magnitude from the zero-loading diffusivity value.

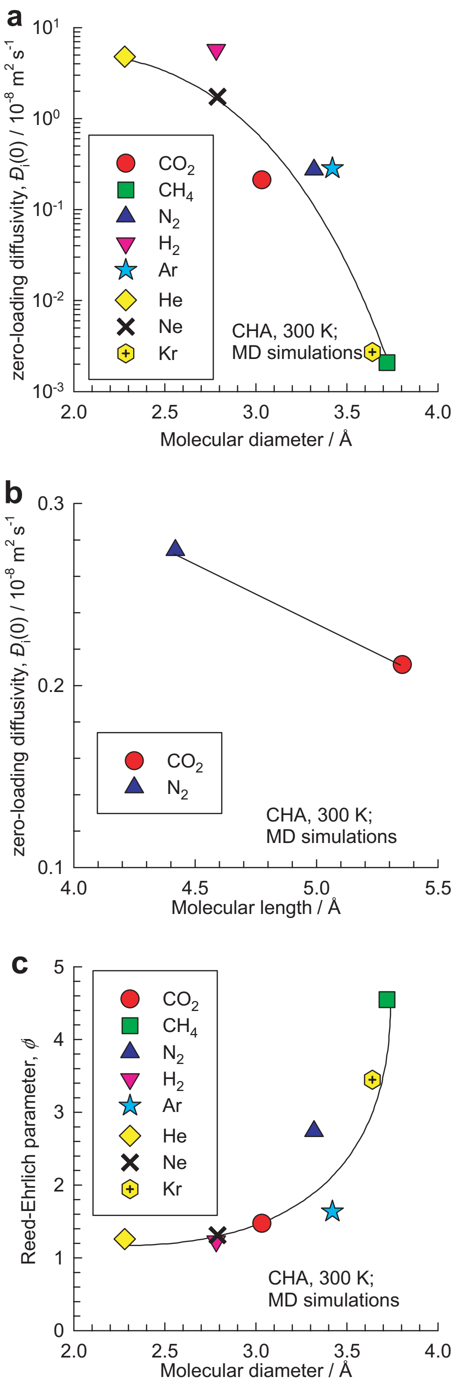

Fig. 10. Reed and Erlich parameters of CHA. The dependence of the (a) $Đ_i(0)$ on the molecular diameter, (b) $Đ_i(0)$ on the molecular length, and (c) ϕ_i on the molecular diameter.

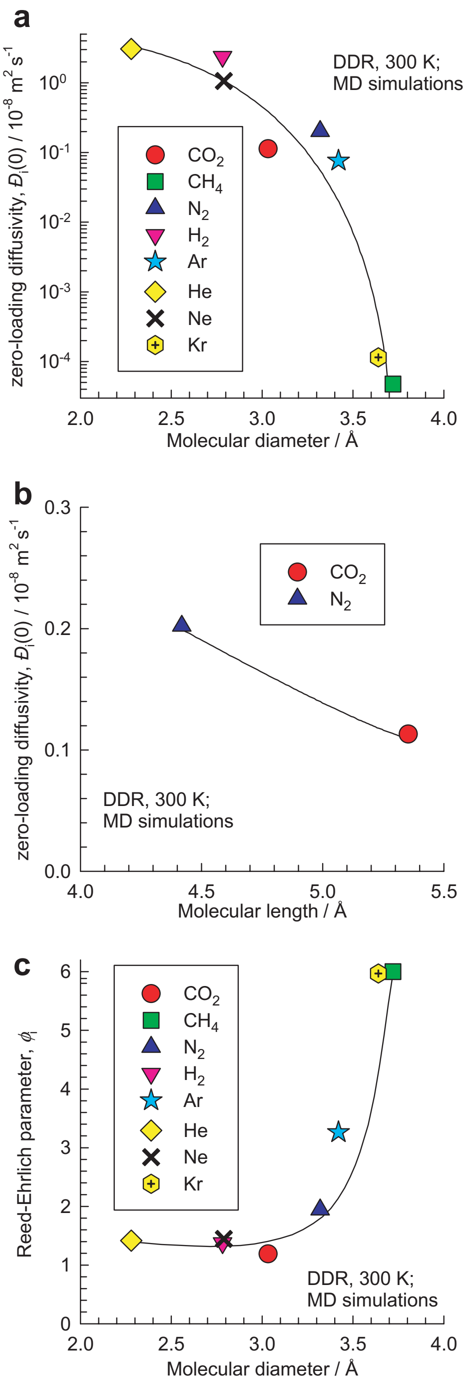

Fig. 11. Reed and Erlich parameters of DDR. The dependence of the (a) $Đ_i(0)$ on the molecular diameter, (b) $Đ_i(0)$ on the molecular length, and (c) ϕ_i on the molecular diameter.

Application of Eq. (1) to describe diffusion in a binary mixture made up of a species i along with "tagged" or "traced" species i allows us to relate the self-diffusivity $D_{i,\mathrm{self}}$ with $Đ_i$ [26]:

$$D_{i,\mathrm{self}} = \frac{1}{\frac{1}{Đ_i} + \frac{\theta_i}{Đ_{ii}}} \quad \text{(unary)} \tag{10}$$

The $Đ_{ii}$ in Eq. (10) are the self-exchange coefficients that quantify correlation effects for a unary system. The $D_{i,\mathrm{self}}$ is usually lower than the $Đ_i$; these two approach each other as $q_i \rightarrow q_{i,\mathrm{sat}}$. Fig. 15 shows the MD simulation results of $Đ_{ii}/Đ_i$ as a function of θ_i for Ne, Ar, and CH_4 in different zeolites. For all three molecules, we note that the $Đ_{ii}/Đ_i$ values for LTA, CHA and DDR are significantly higher than those for the corresponding molecules in AFI, FAU and AFI. This suggests that correlation effects are much stronger in AFI, FAU and MFI and significantly weaker in LTA, CHA and DDR. For any given zeolite, $Đ_{ii}/Đ_i$ values

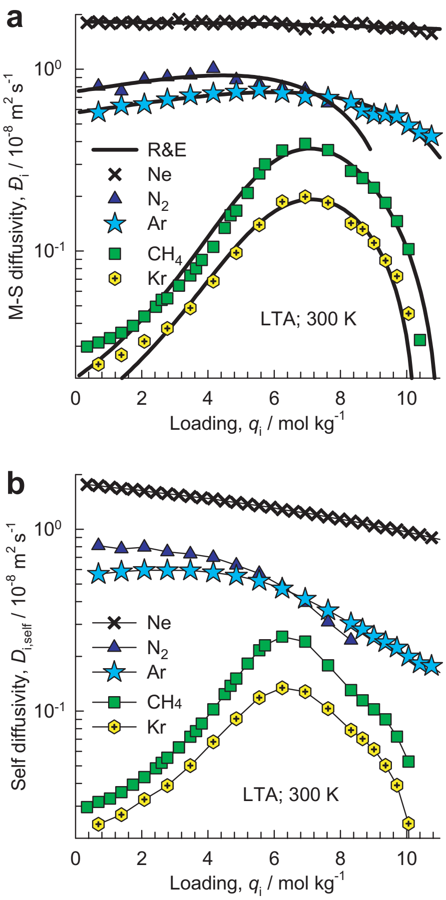

Fig. 12. (a) M–S diffusivity $Đ_i$ and (b) self-diffusivity in LTA of Ne, N_2, Ar, CH_4, and Kr. The continuous solid lines in (a) represent the Reed and Ehrlich model fits of the data. In these fits we take $z = 5$.

follow the hierarchy the Ne < Ar < CH_4, as is exemplified in Fig. 15d for LTA. This suggests that the *degree of confinement* also determines correlation effects; the stronger the confinement, the weaker are the correlation effects. The $Đ_{ii}/Đ_i$ is also loading dependent and an empirical expression suggested earlier is [27]

$$\frac{Đ_{ii}}{Đ_i} = a_i \exp(-b_i\theta_i) \tag{11}$$

As illustration, the fitted values of a_i and b_i for Ne and Ar in different zeolites are given in Table 3; these will be used in the next section for predicting the diffusion behavior of Ne/Ar mixtures.

4. Mixture diffusion in zeolites

From a practical point of view, the mutual influence of different molecules within zeolites is one of the most challenging aspects that needs to be quantified. To get a flavor of mixture diffusion, let us consider *self*-diffusivities in 50–50 Ar/Ne mixtures in various zeolites as a function of the *total* mixture loading, q; see Fig. 16. In AFI, FAU, and MFI the $D_{i,\text{self}}$ of Ne, the more mobile species, is considerably lower in the mixture than for pure Ne. This slowing-down effect appears to increase with increasing q. On the other hand, the $D_{i,\text{self}}$ of Ar, the tardier species, is higher in the mixture than for pure Ar. This speeding-up effect appears to also increase with increasing q. Ar/Ne mixture diffusion in LTA, CHA and DDR has a different character. When q is sufficiently low, the $D_{i,\text{self}}$ in the mixture are practically the same as for the pure components. Only at

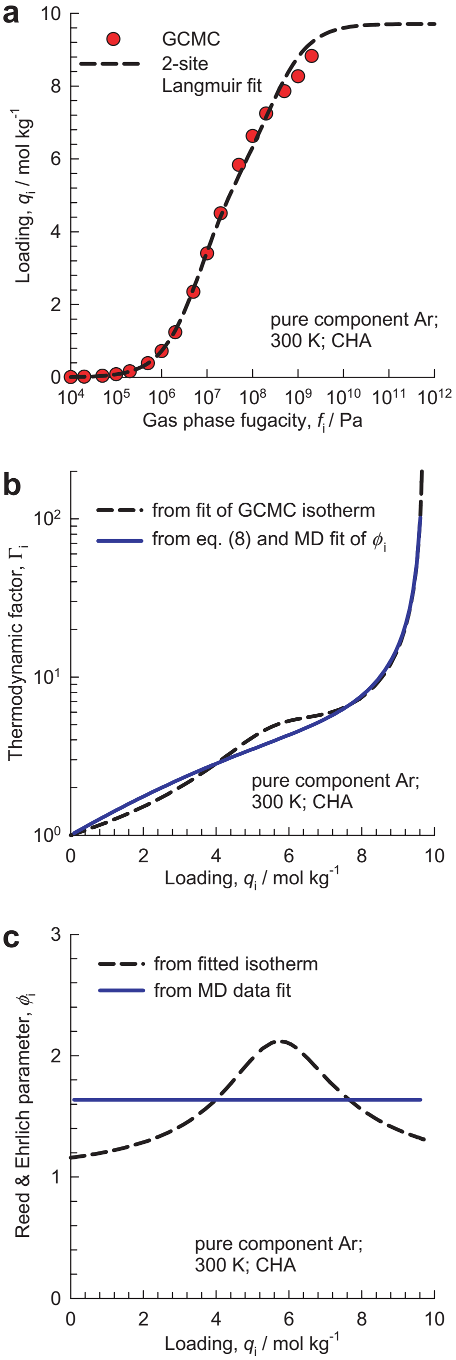

Fig. 13. (a) GCMC simulations of the isotherm for Ar in CHA at 300 K, along with 2-site Langmuir fit (continuous solid line). (b) Comparison of the thermodynamic factor Γ_i, calculated by differentiation of the 2-site Langmuir fit using Eq. (5) with calculations from Eqs. (7) and (8) along with the fits in Table 2. (c) Comparison of ϕ_i, backed out from isotherm fit with the value from Table 2.

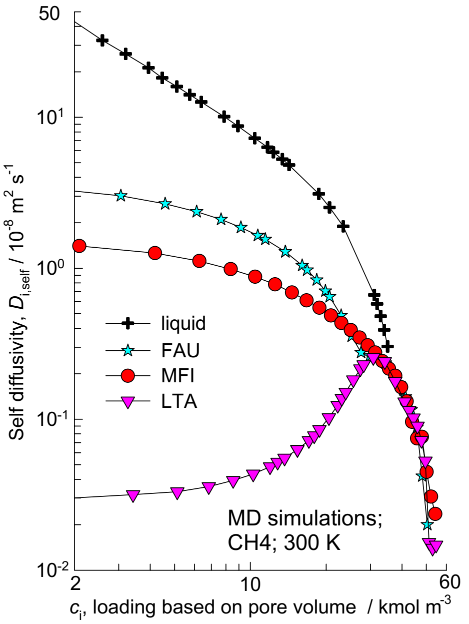

Fig. 14. Self-diffusivities $D_{i,\mathrm{self}}$, as a function of c_i, the molar loading based on pore volume, of CH_4 in various zeolites. Also shown are the $D_{i,\mathrm{self}}$ in pure liquid CH_4.

Table 3
Correlation parameters a_i and b_i describing self-exchange coefficients $Đ_{ii}$ defined by Eq. (11) for Ne and Ar in various zeolites determined from MD simulations of pure component $Đ_i$ and $D_{i,\mathrm{self}}$

Component	Zeolite	a_i	b_i
Ne	CHA	0.7	1.3
Ar	CHA	2.6	1.6
Ne	DDR	1	2.5
Ar	DDR	4	3
Ne	LTA	0.65	1.7
Ar	LTA	2.4	2
Ne	AFI	0.13	−0.9
Ar	AFI	0.15	−1.4
Ne	MFI	0.14	0
Ar	MFI	1	3
Ne	FAU	0.26	1
Ar	FAU	0.38	0.4

higher values of q is there evidence of slowing-down and speeding-up. So for sufficiently low loadings in LTA, CHA and DDR individual species can be taken to diffuse independently of one another. A similar picture emerges for self-diffusion in CO_2/CH_4, CO_2/H_2, CH_4/H_2, N_2/H_2,

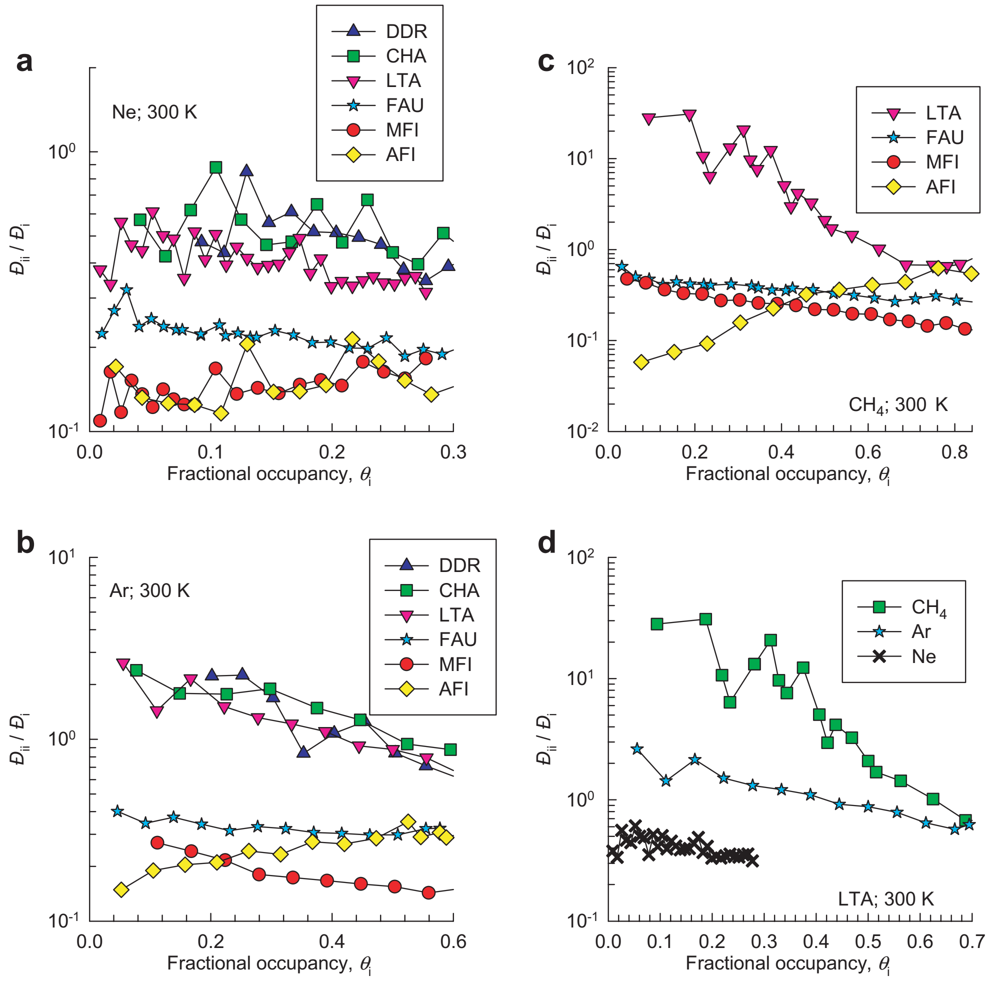

Fig. 15. Occupancy dependencies of the ratio of the self-exchange coefficient to the M–S diffusivity $Đ_{ii}/Đ_i$ for (a) Ne, (b) Ar and (c) CH_4 in different zeolites, and (d) different molecules in LTA.

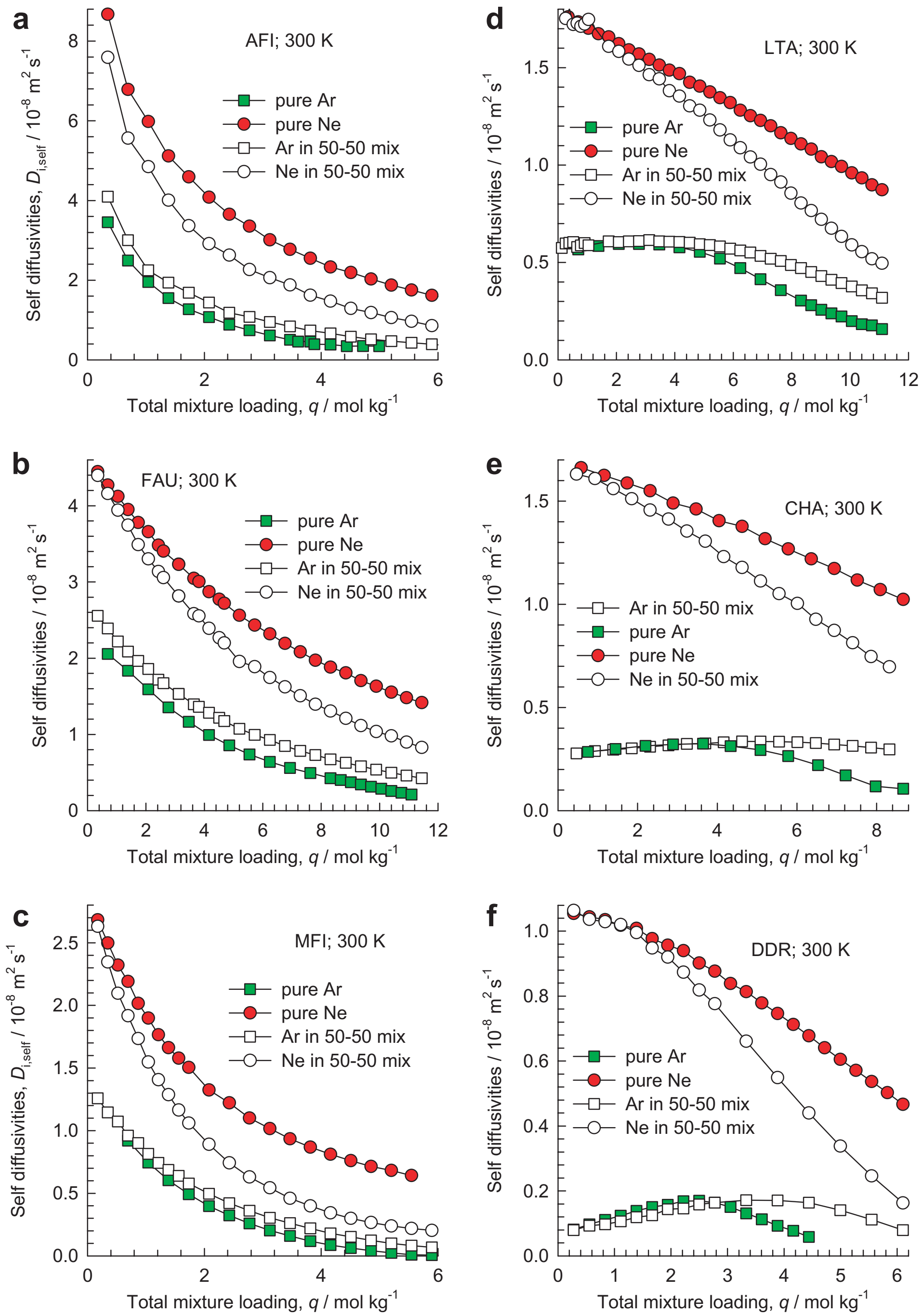

Fig. 16. Self-diffusivities of pure Ne and Ar, and in 50–50 Ne/Ar mixtures in various zeolites as a function of the total mixture loading q.

CH_4/He, CH_4/N_2, CO_2/N_2, Ar/CH_4 and Ar/H_2 mixtures; see Supplementary material accompanying this publication.

For engineering process design the $D_{i,\mathrm{self}}$ are not directly usable and for a *quantitative* analysis of mixture diffusion we proceed in a different manner. The first step is to separate the mutual influences on *thermodynamics* and on *diffusion*. Towards this end we need to "factor out" the thermodynamics. We begin by casting Eq. (1) into $(n-1)$ dimensional matrix notation. The gradient of the chemical potentials in Eq. (1) can be related to the gradients in the loadings by defining a $(n-1)\times(n-1)$ dimensional matrix of thermodynamic factors $[\Gamma]$

$$\frac{q_i}{RT}\frac{\mathrm{d}\mu_i}{\mathrm{d}x} = \sum_{j=1}^{n} \Gamma_{ij}\frac{\mathrm{d}q_j}{\mathrm{d}x}; \quad \Gamma_{ij} \equiv \frac{q_i}{f_i}\frac{\partial f_i}{\partial q_j}; \qquad i,j=1,\ldots,n \tag{12}$$

The elements Γ_{ij} in Eq. (12) can be estimated, for example, using the Ideal Adsorbed Solution Theory of Myers and Prausnitz [28] and the fits of the pure component isotherm data. The fluxes N_i can be explicitly expressed as functions of the gradients in the loading

$$(N) = -\rho[\Delta][\Gamma]\frac{\mathrm{d}(q)}{\mathrm{d}x} \tag{13}$$

where $[\Delta]$ is a square matrix of M–S diffusivities. Compliance with the Onsager Reciprocal Relations demands that

$$q_j\Delta_{ij} = q_i\Delta_{ji}; \quad i,j = 1,2,\ldots,n \tag{14}$$

In our earlier publications the Onsager Reciprocal Relations (14) were incorrectly printed [3,29,30]. The elements Δ_{ij} can be determined from MD simulations and the simulation results for Ne/Ar, CO_2/CH_4, CO_2/H_2, CH_4/H_2, N_2/H_2, CH_4/He, CH_4/N_2, CO_2/N_2, Ar/CH_4 and Ar/H_2 mixtures are given in Supplementary material. We focus here on estimating Δ_{ij} from pure component diffusion data.

For a binary mixture Eq. (13) can be written explicitly for the two species

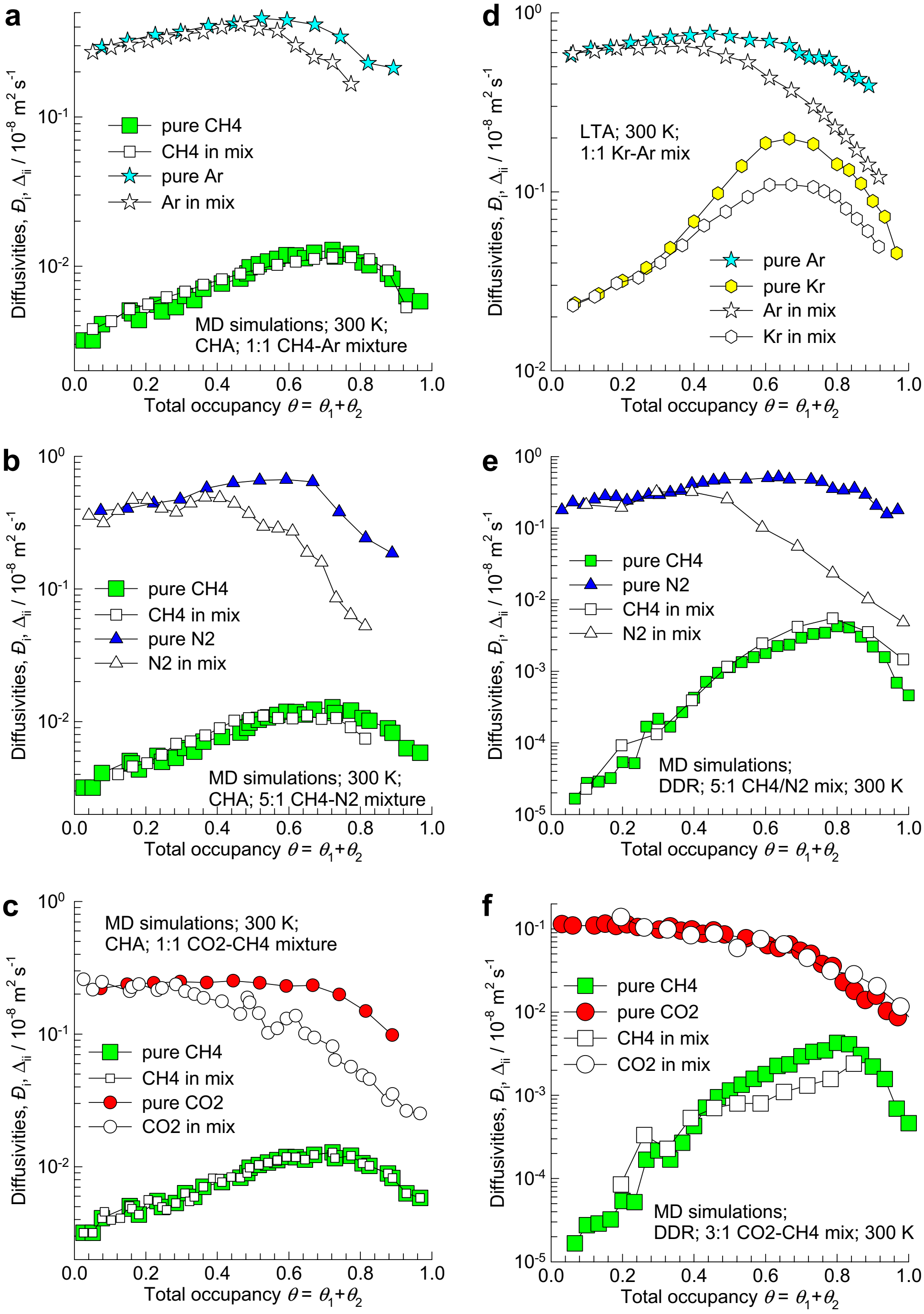

Fig. 17. M–S diffusivities Δ_{ii} and the pure component $Đ_i$ as a function of occupancy θ in various mixtures: (a) Ar/CH_4 in CHA, (b) N_2/CH_4 in CHA, (c) CO_2/CH_4 in CHA, (d) Ar/Kr in LTA, (e) N_2/CH_4 in DDR, and (f) CO_2/CH_4 in DDR.

$$\begin{aligned}N_1 &= -\rho\varDelta_{11}\left(\Gamma_{11}\frac{\mathrm{d}q_1}{\mathrm{d}x}+\Gamma_{12}\frac{\mathrm{d}q_2}{\mathrm{d}x}\right)-\rho\varDelta_{12}\left(\Gamma_{22}\frac{\mathrm{d}q_2}{\mathrm{d}x}+\Gamma_{21}\frac{\mathrm{d}q_1}{\mathrm{d}x}\right)\\ N_2 &= -\rho\varDelta_{21}\left(\Gamma_{11}\frac{\mathrm{d}q_1}{\mathrm{d}x}+\Gamma_{12}\frac{\mathrm{d}q_2}{\mathrm{d}x}\right)-\rho\varDelta_{22}\left(\Gamma_{22}\frac{\mathrm{d}q_2}{\mathrm{d}x}+\Gamma_{21}\frac{\mathrm{d}q_1}{\mathrm{d}x}\right)\end{aligned} \tag{15}$$

The diagonal elements $\varDelta_{11}$ and $\varDelta_{22}$ are related the M–S diffusivities

$$\varDelta_{11} = \frac{\text{Đ}_1}{1+\frac{\frac{\theta_2}{\text{Đ}_{12}/\text{Đ}_1}}{1+\frac{\theta_1}{\text{Đ}_{21}/\text{Đ}_2}}};\quad \varDelta_{22} = \frac{\text{Đ}_2}{1+\frac{\frac{\theta_1}{\text{Đ}_{21}/\text{Đ}_2}}{1+\frac{\theta_2}{\text{Đ}_{12}/\text{Đ}_1}}} \tag{16}$$

The denominators in Eq. (16) quantify the slowing-down effects; indeed, both the diagonal elements $\varDelta_{ii}$ will be lower than the corresponding pure component M–S diffusivities Đ_i. Clearly, the slowing-down will be significant only at high occupancies θ_i. At sufficiently low occupancies we have $\varDelta_{ii} \approx \text{Đ}_i$.

The cross-coefficients $\varDelta_{12}$ and $\varDelta_{21}$ are

$$\varDelta_{12} = \frac{\frac{q_{1,\mathrm{sat}}}{q_{2,\mathrm{sat}}}\frac{\theta_1}{\text{Đ}_{12}/\text{Đ}_1}\text{Đ}_2}{1+\frac{\theta_1}{\text{Đ}_{21}/\text{Đ}_2}+\frac{\theta_2}{\text{Đ}_{12}/\text{Đ}_1}};\quad \varDelta_{21} = \frac{q_2}{q_1}\varDelta_{12} \tag{17}$$

Due to coupling of the flux of component 1 with that of component 2, and vice-versa, as expressed in Eq. (15), speeding-up is effectuated. Speeding-up is caused by cross-coefficients with finite and significant values. A tardy species 2, will be speeded-up by the more mobile species 1 due to a finite cross-term $\varDelta_{21}$. In view of the presence of the occupancies θ_i in the numerator in Eq. (17), it is clear that speeding-up is only effective at reasonably high occupancies. Another requirement of a significant speeding-up of species 2 is that ratio

$$\frac{\left(\Gamma_{11}\frac{\mathrm{d}q_1}{\mathrm{d}x}+\Gamma_{12}\frac{\mathrm{d}q_2}{\mathrm{d}x}\right)}{\left(\Gamma_{22}\frac{\mathrm{d}q_2}{\mathrm{d}x}+\Gamma_{21}\frac{\mathrm{d}q_1}{\mathrm{d}x}\right)} \gg 1 \tag{18}$$

should exceed unity to a significant extent. This ratio will be significantly larger than unity only when species 1 is much more strongly adsorbed than species 2, i.e. $q_1 \gg q_2$. The combination of the two requirements: (a) higher mobility of species 1, i.e. $\text{Đ}_1 > \text{Đ}_2$, and (b) higher adsorption strength for species 1 is rare and for this reason speeding-up is also rare. It is more common to find that the more mobile species is also more poorly adsorbed; speeding-up will usually be of negligible importance.

In order to *predict* the elements $\varDelta_{ij}$ we need to be able to estimate the binary exchange coefficients Đ_{12} and Đ_{21}. The following interpolation formula has been suggested earlier [3,27]:

$$q_{2,\mathrm{sat}}\text{Đ}_{12} = \left[q_{2,\mathrm{sat}}\text{Đ}_{11}\right]^{q_1/(q_1+q_2)}\left[q_{1,\mathrm{sat}}\text{Đ}_{22}\right]^{q_2/(q_1+q_2)} = q_{1,\mathrm{sat}}\text{Đ}_{21} \tag{19}$$

allowing the estimation of Đ_{12} and Đ_{21} from the self-exchange coefficients Đ_{11} and Đ_{22}.

Let us consider a special, limiting, case in which $\text{Đ}_{ii}/\text{Đ}_i \to \infty$; when this approximation applies to each of the n species in the mixture we obtain the following simplification of Eq. (1):

$$N_i = -\rho\text{Đ}_i\frac{q_i}{RT}\frac{\mathrm{d}\mu_i}{\mathrm{d}x};\quad i = 1,\ldots,n \tag{20}$$

which relations were used by Habgood [31] to described N_2/CH_4 mixture diffusion in LTA. Eq. (20) implies

$$\varDelta_{11} = \text{Đ}_1;\quad \varDelta_{22} = \text{Đ}_2;\quad \varDelta_{12} = \varDelta_{21} = 0 \tag{21}$$

The Habgood model does not anticipate any speeding-up or slowing-down processes and the flux N_1 is coupled with N_2 only via the thermodynamic factors Γ_{ij}. Eq. (6) can be applied to estimate the $\varDelta_{ii}$ from pure Đ_i fits; this estimation should be based on the total occupancy in the *mixture*:

$$\theta = \theta_1 + \theta_2 = \frac{q_1}{q_{1,\mathrm{sat}}} + \frac{q_2}{q_{2,\mathrm{sat}}} \tag{22}$$

Eqs. (20) and (21) can be expected to hold, as an approximation, for mixtures of molecules that are strongly confined within zeolite structures such as LTA, CHA and DDR. In order to test this conclusion we present a set of representative mixture simulation results for $\varDelta_{ii}$ in Fig. 17, along with the pure component Đ_i data, both as a function of the θ. For CH_4/Ar diffusion in CHA (see Fig. 17a), Eq. (21) holds up to a total occupancy of 0.5; for higher θ values, there is a slight slowing-down of Ar. For CH_4/N_2 and CO_2/CH_4 diffusion in CHA the Habgood model is a good approximation for $\theta < 0.4$; see Fig. 17b and c. These results underpin the findings of Li et al. [9,10] who concluded that the Habgood model provided a good description for experimental permeation data for CO_2/CH_4, CO_2/N_2, and N_2/CH_4 mixtures across a SAPO-34 membrane.

For Ar/Kr diffusion in LTA (see Fig. 17d), and CH_4/N_2 and CO_2CH_4 diffusion in DDR (Fig. 17e and f), a similar conclusion holds: the Habgood model is a good approximation for occupancies lower than 0.4, but becomes progressively worse for $\theta > 0.4$.

In the context of zeolite membrane separation of CO_2(1)–CH_4(2) mixtures, CHA and DDR are good struc-

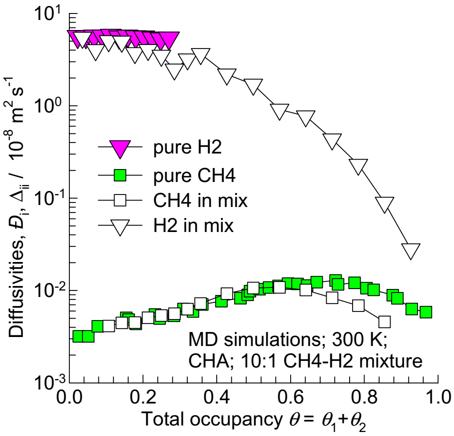

Fig. 18. M–S diffusivities $\varDelta_{ii}$ and the pure component Đ_i as a function of occupancy θ in 10:1 CH_4/H_2 mixture in CHA at 300 K.

tural choices because $\Delta_{11} \gg \Delta_{22}$, and there is no significant slowing-down of the mobile CO_2. Furthermore, CO_2 also has a higher adsorption strength than CH_4, and therefore diffusion selectivity complements adsorption selectivity leading to high permeation selectivity [17].

A different picture emerges for diffusion of mixtures in CHA, LTA and DDR containing weakly confined molecules such as Ne, He, and H_2. From data in Fig. 15 we should expect correlation effects to strongly influence the mobilities of Ne, He, and H_2 in the mixture because $Đ_{ii}/Đ_i$ of these molecules are significantly lower than unity. To verify this we compare Δ_{ii} with the pure component $Đ_i$ for CH_4/H_2 mixture diffusion in CHA; see Fig. 18. We note that there is a steady reduction in the Δ_{ii} for H_2 for $\theta > 0.1$. This provides an explanation for the permeation data for N_2/H_2, and CH_4/H_2 mixtures across SAPO-34 membrane, for which Li et al. [9] found that the Habgood model *over*-estimates the H_2 fluxes. For more accurate modeling the slowing-down of the highly mobile H_2 needs to be accounted for.

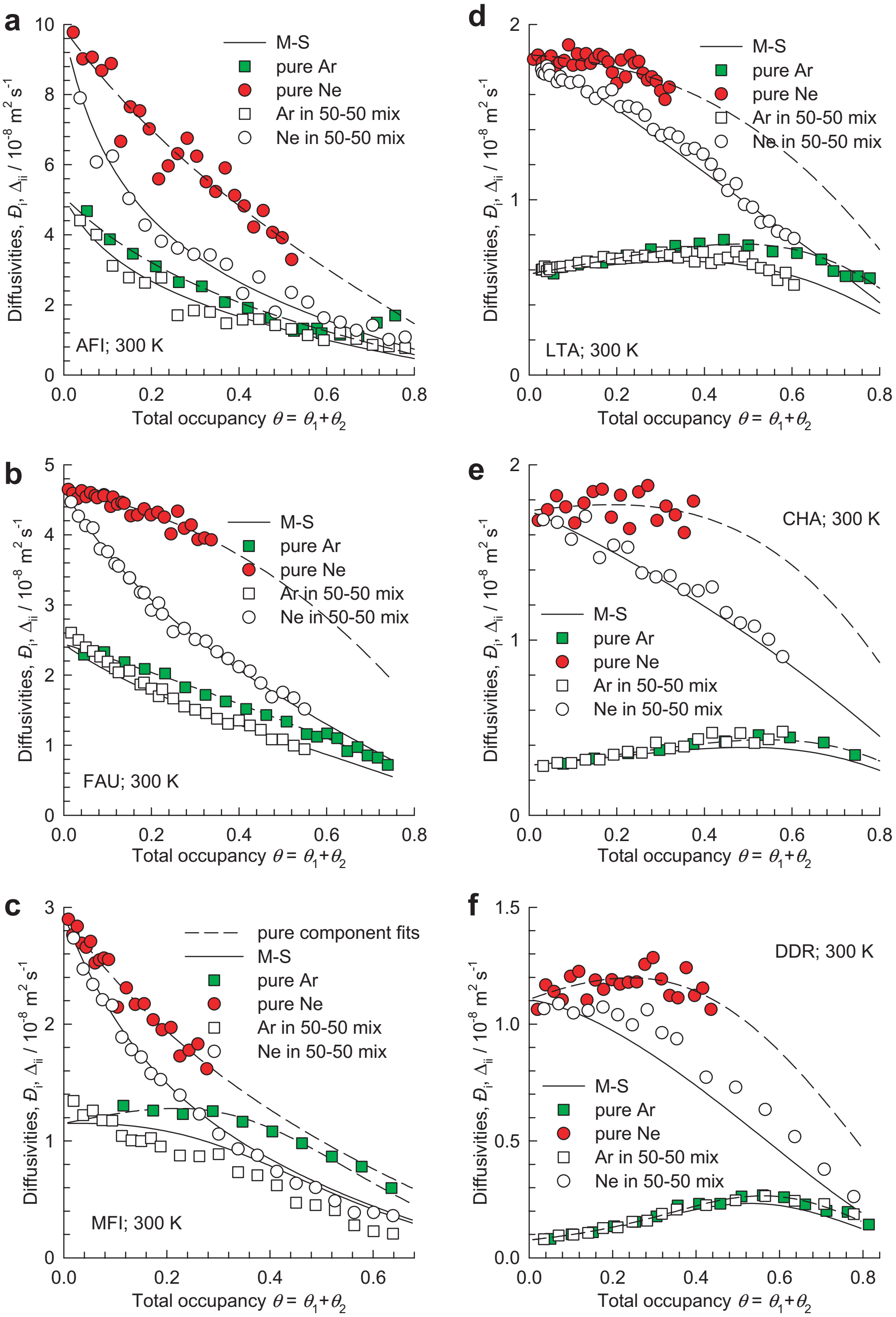

Fig. 19. M–S diffusivities Δ_{ii} in 50–50 Ne/Ar mixtures in various zeolites, as a function of the total mixture loading q. Also plotted are the pure component $Đ_i$ for Ne and Ar. The continuous solid lines are the calculations of Δ_{ii} using Eqs. (16) and (19), with the parameter fits specified in Tables 2 and 3. The dashed lines are the calculation of pure component $Đ_i$ using Eq. (6), based on total occupancy in the mixture.

We now examine the accuracy of the interpolation formula (19) for quantifying the slowing-down effects by considering diffusion of an equimolar Ne(1)/Ar(2) mixture in various zeolites; the MD simulation results for Δ_{ii} are plotted along with the pure component $Đ_i$ in Fig. 19. The dashed lines are the $Đ_i$ calculated from Eq. (6) with parameter fits given in Table 2. For Ne(1)/Ar(2) mixture, $Đ_1 > Đ_2$ *and* $\theta_2 > \theta_1$ in all zeolites; consequently, $1 + \frac{\frac{\theta_2}{Đ_{12}/Đ_1}}{1+\frac{\theta_1}{Đ_{21}/Đ_2}}$ is significantly larger than unity, while $1 + \frac{\frac{\theta_1}{Đ_{21}/Đ_2}}{1+\frac{\theta_2}{Đ_{12}/Đ_1}}$ is only slightly larger than unity. This results in a significant slowing-down of Ne, $\Delta_{11} \ll Đ_1$, with increasing occupancy. The corresponding slowing-down of Ar is considerably smaller; and in LTA, CHA, and DDR we note that $\Delta_{22} \approx Đ_2$ is a good approximation, even at high occupancies. The continuous solid lines are the calculations of Δ_{ii} using Eqs. (16) and (19), with the parameter fits specified in Tables 2 and 3. The good agreement between the simulated and calculated Δ_{ii} provides validation of interpolation formula (19). However, this procedure is difficult to use in practice as it requires a considerable amount of data that is often unavailable. The slowing-down effect on Ne is particularly severe in AFI, and MFI. In these two zeolites, Ne and Ar have nearly the same Δ_{ii} for $\theta > 0.4$. In the context of separation processes relying on diffusion selectivity, it is clear that structures such as AFI and MFI are not attractive zeolites [17].

5. Conclusions

MD simulations of the diffusivities of both pure components He, H_2, Ne, CO_2, Ar, N_2, Kr, and CH_4 and in several binary mixtures containing these molecules have been carried out for a range of molar loadings in six different zeolites. The following major conclusions can be drawn from the data:

(1) The M–S diffusivity $Đ_i$ is generally a strong function of loading and decreases by a few orders of magnitude as the saturation loading, $q_{i,\text{sat}}$ is approached.
(2) The $Đ_i$ in AFI, FAU, and MFI often show a decreasing trend with loading q_i. For AFI and FAU the $Đ_i$–q_i trend mirrors the variation of $1/\Gamma_i$ with q_i.
(3) In zeolite structures consisting of cages separated by narrow windows (CHA, DDR, LTA) the $Đ_i$ of strongly confined molecules such as Kr and CH_4 increases sharply with loading before decreasing as the loading approaches $q_{i,\text{sat}}$. The increase of $Đ_i$ is due to the reduction in the free energy barrier for inter-cage hops with increasing q_i. The Reed–Ehrlich model [18] is a particularly simple and useful model to describe the $Đ_i$–q_i dependence in CHA, LTA and DDR. The Reed and Ehrlich parameters appear to depend on the molecular dimensions, offering the possibility of anticipating the loading dependence for a guest–host combination.
(4) MD simulation results for the self-exchange coefficients $Đ_{ii}$ for a variety of molecules show that correlation effects are particularly significant for AFI, FAU and MFI zeolites. For a given species, correlation effects tend to be weaker for LTA, CHA and DDR zeolites. Correlation effects tend to become more significant at higher loadings. For weakly confined molecules such as Ne, H_2, and He, correlation effects are significant in all zeolites.
(5) For zeolite structures such as LTA, CHA and DDR consisting of cages separated by *narrow* windows, Eqs. (20) and (21) can be used as reasonable approximations for mixtures of strongly confined molecules provided the total occupancy is less than about 0.4. However, even for these zeolites, the slowing-down effect is significant for weakly confined molecules such as Ne, He, and H_2 that have high mobilities. Generally speaking, slowing-down effects will be significant for highly mobile, poorly adsorbing, molecules in mixtures with tardy, strongly adsorbing molecules.
(6) The interpolation formula (19) provides a reasonable estimation procedure for the binary exchange coefficient $Đ_{ij}$.

Acknowledgments

R.K. and J.M.v.B. acknowledge the grant of a TOP subsidy from the Netherlands Foundation for Fundamental Research (NWO-CW) for intensification of reactors and NWO/NCF for provision of high performance computing resources. The GCMC simulations were carried out with the BIGMAC program developed by Dr. T.J.H. Vlugt.

Appendix A. Supplementary material

Appendix A1 presents some details of the GCMC and MD simulation methodologies, including the force fields used. Appendix A2 contains complete data on the GCMC and MD simulation results for sorption and diffusion of pure components in different zeolites. This also includes snapshots of the location of the molecules in various frameworks. Appendix A3 presents data on $D_{i,\text{self}}$ and Δ_{ii} for a variety of binary mixtures. Supplementary data associated with this article can be found, in the online version, at doi:10.1016/j.micromeso.2007.04.036.

References

[1] R. Krishna, R. Baur, Sep. Purif. Technol. 33 (2003) 213–254.
[2] R. Krishna, J.M. van Baten, E. García-Pérez, S. Calero, Ind. Eng. Chem. Res. 46 (2007) 2974–2986.
[3] R. Krishna, J.M. van Baten, J. Phys. Chem. B 109 (2005) 6386–6396.
[4] J. Kärger, D.M. Ruthven, Diffusion in Zeolites and Other Microporous Solids, John Wiley, New York, 1992.
[5] H. Jobic, J. Kärger, M. Bée, Phys. Rev. Lett. 82 (1999) 4260–4263.
[6] S.S. Chong, H. Jobic, M. Plazanet, D.S. Sholl, Chem. Phys. Lett. 408 (2005) 157–161.

[7] H. Jobic, C. Laloué, C. Laroche, J.M. van Baten, R. Krishna, J. Phys. Chem. B 110 (2006) 2195–2201.
[8] G.K. Papadopoulos, H. Jobic, D.N. Theodorou, J. Phys. Chem. B 108 (2004) 12748–12756.
[9] S. Li, J.L. Falconer, R.D. Noble, R. Krishna, J. Phys. Chem. C 111 (2007) 5075–5082.
[10] S. Li, J.L. Falconer, R.D. Noble, R. Krishna, Ind. Eng. Chem. Res. 46 (2007) 3904–3911.
[11] D. Dubbeldam, S. Calero, T.J.H. Vlugt, R. Krishna, T.L.M. Maesen, B. Smit, J. Phys. Chem. B 108 (2004) 12301–12313.
[12] K. Makrodimitris, G.K. Papadopoulos, D.N. Theodorou, J. Phys. Chem. B 105 (2001) 777–788.
[13] A.I. Skoulidas, D.S. Sholl, J. Phys. Chem. B 106 (2002) 5058–5067.
[14] O. Talu, A.L. Myers, Colloids Surf. A 187–188 (2001) 83–93.
[15] A.V.A. Kumar, H. Jobic, S.K. Bhatia, J. Phys. Chem. B 110 (2006) 16666–16671.
[16] R. Krishna, J.M. van Baten, Chem. Phys. Lett. 420 (2006) 545–549.
[17] R. Krishna, J.M. Van Baten, Chem. Eng. J. (2007), doi:10.1016/j.cej.2007.02.01.
[18] D.A. Reed, G. Ehrlich, Surf. Sci. 102 (1981) 588–609.
[19] E. Beerdsen, D. Dubbeldam, B. Smit, Phys. Rev. Lett. 95 (2005) 164505.
[20] E. Beerdsen, D. Dubbeldam, B. Smit, Phys. Rev. Lett. 96 (2006) 044501.
[21] R. Krishna, D. Paschek, R. Baur, Micropor. Mesopor. Mater. 76 (2004) 233–246.
[22] D.V. Cao, R.J. Mohr, M.B. Rao, S. Sircar, J. Phys. Chem. B 104 (2000) 10498–10501.
[23] J. Caro, M. Bülow, W. Schirmer, J. Kärger, W. Heink, H. Pfeifer, J. Chem. Soc., Faraday Trans. 81 (1985) 2541.
[24] R. Krishna, J.M. van Baten, Ind. Eng. Chem. Res. 44 (2005) 6939–6947.
[25] R. Krishna, J.M. van Baten, Chem. Eng. Technol. 29 (2006) 761–765.
[26] R. Krishna, D. Paschek, Phys. Chem. Chem. Phys. 4 (2002) 1891–1898.
[27] A.I. Skoulidas, D.S. Sholl, R. Krishna, Langmuir 19 (2003) 7977–7988.
[28] A.L. Myers, J.M. Prausnitz, A.I.Ch.E.J. 11 (1965) 121–130.
[29] J.M. van Baten, R. Krishna, Micropor. Mesopor. Mater. 84 (2005) 179–191.
[30] R. Krishna, J.M. van Baten, Ind. Eng. Chem. Res. 45 (2006) 2084–2093.
[31] H.W. Habgood, Can. J. Chem. 36 (1958) 1384–1397.

Supplementary Material to accompany:

Insights into diffusion of gases in zeolites gained from molecular dynamics simulations

R. Krishna*, J.M. van Baten

Van 't Hoff Institute for Molecular Sciences, University of Amsterdam, Nieuwe Achtergracht 166,

1018 WV Amsterdam, The Netherlands

Appendix A1 presents some details of the GCMC and MD simulation methodologies, including the force fields used.

Appendix A2 contains complete data on the GCMC and MD simulation results for sorption and diffusion of pure components in different zeolites. This also includes snapshots of the location of the molecules in various frameworks.

Appendix A3 presents data on on $D_{\mathrm{i,self}}$ and Δ_{ii} for a variety of binary mixtures.

Appendix A1: Simulation methodologies

1. GCMC simulation methodology

The adsorption isotherms for the eight different gases He, Ne, Ar, Kr, H_2, N_2, CO_2, and CH_4 in six different all-silica zeolite structures (MFI, AFI, FAU, CHA, DDR, and LTA) were computed using Monte Carlo (MC) simulations in the grand canonical (GC) ensemble. The crystallographic data are available elsewhere.[1] The zeolite lattices are rigid during simulations, with static atomic charges that are assigned by choosing $q_{\mathrm{Si}} = +2.05$ and $q_{\mathrm{O}} = -1.025$, following the works of Jaramillo and Auerbach and Calero e al. [2, 3]. CH_4 molecules are described with a united atom model, in which each molecule is treated as a single interaction center.[4] CO_2 molecules are taken linear and rigid, with bond length C-O of 1.16Å and partial charges distributed around each molecule to reproduce experimental quadrupole moment. The interaction between adsorbed molecules is described with Coulombic and Lennard-Jones terms. The Coulombic interactions in the system are calculated by Ewald summation for periodic systems[5]. The parameters for CH_4 are taken from Dubbeldam et al[6] and Calero et al.[3]. CO_2 molecules are taken linear and rigid with bond length C–O of 1.16Å according to the 3LJ3CB.EPM2 model developed by Harris and Young [7]. We use the 2LJ3CB.MSKM model for N_2 dumbbell molecules with a rigid interatomic bond of 1.098Å[8, 9]. The partial charges of N_2 and CO_2 are distributed around each molecule to reproduce experimental quadrupole moment. The interactions between adsorbed molecules and the zeolite are dominated by dispersive forces between the pseudo-atoms and the oxygen atoms of the zeolite [10, 11] and the interactions of silicon and aluminium are considered through an effective potential with only the oxygen atoms. The Lennard-Jones parameters for CH_4-zeolite interactions are taken from Dubbeldam et al.[6]. The Lennard-Jones parameters for CO_2-zeolite and N_2-zeolite interactions are essentially those of Makrodimitris et al.[9, 12]. The force fields for He, Ne and Ar are taken from the paper by Skoulidas and Sholl[13]. The force field for Kr is from Talu and Myers [14]. The force field for H_2 corresponds to that given by Kumar et al.[15] In implementing this force field, quantum effects for H_2 have been ignored because the work of Kumar et al.[15] has shown that quantum effects are of negligible importance for temperatures above 200 K; all our simulations were performed at 300 K. The force field of Kumar et al.[15] is quite similar to that used by Gallo et al. [16]. Table 1 summarizes the information on the force field for all gases.

The Lennard-Jones potentials are shifted and cut at 12 Å. The number of unit cells in the simulation box was chosen such that the minimum length in each of the coordinate directions was larger than 24 Å. Periodic boundary conditions were employed. Further GCMC simulation details are available in earlier publications[3, 6, 17].

The GCMC simulations were performed using the BIGMAC code developed by T.J.H. Vlugt[18] as basis. The code was modified to handle rigid molecular structures and charges. S. Calero is gratefully acknowledged for her technical inputs in this regard. Detailed validation of the force fields used for CH_4, CO_2 and N_2 is available elsewhere[6, 12]. Comparisons between experimental data and GCMC simulations for CH_4, CO_2, N_2, Ar, and Kr in a variety of zeolites are given in Figures 1, 2, 3, 4, 5, 6, 7, 8, and 9. These data give an indication of the validity of the force fields.

2. MD simulation methodology

Diffusion is simulated using Newton's equations of motion until the system properties, on average, no longer change in time. The Verlet algorithm is used for time integration. A time step of 1 fs was used in all simulations. For each simulation, *initializing* GCMC moves are used to place the molecules in the domain, minimizing the energy. Next, follows an *equilibration* stage. These are essentially the same as the production cycles, only the statistics are not yet taken into account. This removes any initial large disturbances in the system do not affect statistics. After a fixed number of initialization and equilibrium steps, the MD simulation *production* cycles start. For every cycle, the statistics for determining the mean square displacements (MSDs) are updated. The MSDs are determined for time intervals ranging from 2 fs to 1 ns. In order to do this, an order-*N* algorithm, as detailed in Chapter 4 of Frenkel and Smit[5] is implemented. The Nosé-Hoover thermostat is applied to all the diffusing particles.

The DLPOLY code[19] was used along with the force field implementation as described in the previous section. DL_POLY is a molecular dynamics simulation package written by W. Smith, T.R. Forester and I.T. Todorov and has been obtained from CCLRCs Daresbury Laboratory via the website.[19]

The MD simulations were carried out for a variety of molecular loadings. All simulations were carried out on clusters of PCs equipped with Intel Xeon processors running at 3.4 GHz on the Linux operating system. Each MD simulation, for a specified loading, was run for 120 h, determined to be long enough to obtain reliable statistics for determination of the diffusivities. Several independent MD simulations were run and the results averaged.

The self-diffusivities, $D_{\mathrm{i,self}}$, were computed by analyzing the mean square displacement of each species *i* for each of the coordinate directions:

$$D_{i,self} = \frac{1}{2n_i} \lim_{\Delta t \to \infty} \frac{1}{\Delta t} \left\langle \left(\sum_{l=1}^{n_i} \left(\mathbf{r}_{l,i}(t+\Delta t) - \mathbf{r}_{l,i}(t) \right)^2 \right) \right\rangle \tag{1}$$

In this expression n_{i} represents the number of molecules of species *i* respectively, and $\mathbf{r}_{\mathrm{l,i}}(t)$ is the position of molecule *l* of species *i* at any time *t*. The expression (1) also defines the self-diffusivity in a *n*-component mixture.

For single component diffusion, the Maxwell-Stefan diffusivity was determined for each of the coordinate directions from

$$Đ_i = \frac{1}{2} \lim_{\Delta t \to \infty} \frac{1}{n_i} \frac{1}{\Delta t} \left\langle \left(\sum_{l=1}^{n_i} \left(\mathbf{r}_{l,i}(t+\Delta t) - \mathbf{r}_{l,i}(t) \right) \right)^2 \right\rangle \tag{2}$$

For 1D channel structures of AFI, the reported diffusivities are along the z-direction. For DDR the reported diffusivities are the averages in x- and y- directions $Đ = \left(Đ_x + Đ_y\right)/2$. For all other cases (MFI, FAU, LTA, CHA) the average values calculated according to $Đ = \left(Đ_x + Đ_y + Đ_z\right)/3$ are presented. In all cases reported here, the MSD values were linear in t for t > 10 ps (used in data regression analysis to determine the diffusivities) and we found no evidence of single file diffusion characteristics.

The self-exchange coefficient $Đ_{ii}$ were calculated from

$$Đ_{ii} = \frac{\theta_i}{\frac{1}{D_{i,self}} - \frac{1}{Đ_i}} \tag{3}$$

where θ_i is the fractional occupancy:

$$\theta_i = \frac{q_i}{q_{i,sat}} \tag{4}$$

The values of the saturation capacities $q_{i,sat}$ were determined from GCMC simulations of the isotherms. The isotherm data are reported for each molecule/zeolite in the Appendix A2 of Supplementary Data this publication, along with data on $D_{i,self}$ and $Đ_i$ for pure components.

For binary mixtures the elements of the matrix [Δ], defined by

$$(N) = -\rho[\Delta][\Gamma]\frac{d(q)}{dx} \tag{5}$$

are obtained in each coordinate direction from

$$\Delta_{ij} = \frac{1}{2}\lim_{\Delta t\to\infty}\frac{1}{n_j}\frac{1}{\Delta t}\left\langle\left(\sum_{l=1}^{n_i}\left(\mathbf{r}_{l,i}(t+\Delta t)-\mathbf{r}_{l,i}(t)\right)\right)\bullet\left(\sum_{k=1}^{n_j}\left(\mathbf{r}_{k,j}(t+\Delta t)-\mathbf{r}_{k,j}(t)\right)\right)\right\rangle \tag{6}$$

In this expression n_i and n_j represent the number of molecules of species i and j respectively, and $\mathbf{r}_{l,i}(t)$ is the position of molecule l of species i at any time t. In this context we note a typographical error in eq (6) as printed in earlier publications [20-22] wherein the denominator in the right member had n_i instead of n_j. The simulation results presented in these publications are, however, correct as the proper formula given in eq (6) was used. Compliance with the Onsager Reciprocal Relations demands that

$$n_j\Delta_{ij} = n_i\Delta_{ji}; \quad i,j = 1,2,....n \tag{7}$$

For Ne/Ar, CO_2/CH_4, CO_2/H_2, CH_4/H_2, N_2/H_2, CH_4/He, CH_4/N_2, CO_2/N_2, Ar/CH_4 and Ar/H_2 mixtures the data on the self-diffusivities $D_{i,self}$ along with diagonal elements Δ_{ii} are reported in graphical form in Appendix A3 for the six all-silica zeolites.

Animations of MD simulations showing the motion of molecules, of both pure components and in mixtures, in a variety of zeolites can be viewed on our website[23].

3. References

[1] C. Baerlocher, L.B. McCusker, Database of Zeolite Structures, International Zeolite Association, http://www.iza-structure.org/databases/, 26 June 2001.

[2] E. Jaramillo, S.M. Auerbach, New force field for Na cations in faujasite-type zeolites, J. Phys. Chem. B 103 (1999) 9589-9594.

[3] S. Calero, D. Dubbeldam, R. Krishna, B. Smit, T.J.H. Vlugt, J.F.M. Denayer, J.A. Martens, T.L.M. Maesen, Understanding the role of sodium during adsorption. A force field for alkanes in sodium exchanged faujasites, J. Am. Chem. Soc. 126 (2004) 11377-11386.

[4] J.P. Ryckaert, A. Bellemans, Molecular dynamics of liquid alkanes, Faraday Discuss. Chem. Soc. 66 (1978) 95-106.

[5] D. Frenkel, B. Smit, Understanding molecular simulations: from algorithms to applications, Academic Press, 2nd Edition, San Diego, 2002.

[6] D. Dubbeldam, S. Calero, T.J.H. Vlugt, R. Krishna, T.L.M. Maesen, B. Smit, United Atom Forcefield for Alkanes in Nanoporous Materials, J. Phys. Chem. B 108 (2004) 12301-12313.

[7] J.G. Harris, K.H. Yung, Carbon Dioxide's Liquid-Vapor Coexistence Curve And Critical Properties as Predicted by a Simple Molecular Model, J. Phys. Chem. 99 (1995) 12021-12024.

[8] C.S. Murthy, K. Singer, M.L. Klein, I.R. McDonald, Pairwise additive effective potentials for nitrogen, Mol. Phys. 41 (1980) 1387-1399.

[9] K. Makrodimitris, G.K. Papadopoulos, D.N. Theodorou, Prediction of permeation properties of CO_2 and N_2 through silicalite via molecular simulations, J. Phys. Chem. B 105 (2001) 777-788.

[10] A.G. Bezus, A.V. Kiselev, A.A. Lopatkin, P.Q. Du, Molecular statistical calculation of the thermodynamic adsorption characteristics of zeolites using the atom-atom approximation. Part 1. Adsorption of methane by zeolite sodium-X, J.Chem.Soc., Faraday Trans. II 74 (1978) 367-379.

[11] A.V. Kiselev, A.A. Lopatkin, A.A. Shul'ga, Molecular statistical calculation of gas adsorption by silicalite, Zeolites 5 (1985) 261-267.

[12] E. García-Pérez, J.B. Parra, C.O. Ania, A. García-Sánchez, J.M. Van Baten, R. Krishna, D. Dubbeldam, S. Calero, A computational study of CO_2, N_2 and CH_4 adsorption in zeolites, Adsorption 13 (2007) 469-476.

[13] A.I. Skoulidas, D.S. Sholl, Transport diffusivities of CH_4, CF_4, He, Ne, Ar, Xe, and SF_6 in silicalite from atomistic simulations, J. Phys. Chem. B 106 (2002) 5058-5067.

[14] O. Talu, A.L. Myers, Reference potentials for adsorption of helium, argon, methane and krypton in high-silica zeolites, Colloids Surf., A 187-188 (2001) 83-93.

[15] A.V.A. Kumar, H. Jobic, S.K. Bhatia, Quantum effects on adsorption and diffusion of hydrogen and deuterium in microporous materials, J. Phys. Chem. B 110 (2006) 16666-16671.

[16] M. Gallo, T.M. Nenoff, M.C. Mitchell, Selectivities for binary mixtures of hydrogen/methane and hydrogen/carbon dioxide in silicalite and ETS-10 by Grand Canonical Monte Carlo techniques, Fluid Phase Equilib. 247 (2006) 135-142.

[17] T.J.H. Vlugt, R. Krishna, B. Smit, Molecular simulations of adsorption isotherms for linear and branched alkanes and their mixtures in silicalite, J. Phys. Chem. B 103 (1999) 1102-1118.

[18] T.J.H. Vlugt, BIGMAC, University of Amsterdam, http://molsim.chem.uva.nl/bigmac/, 1 November 2000.

[19] W. Smith, T.R. Forester, I.T. Todorov, The DL_POLY Molecular Simulation Package, Warrington, England, http://www.cse.clrc.ac.uk/msi/software/DL_POLY/index.shtml, March 2006.

[20] R. Krishna, J.M. van Baten, Diffusion of alkane mixtures in zeolites. Validating the Maxwell-Stefan formulation using MD simulations, J. Phys. Chem. B 109 (2005) 6386-6396.

[21] J.M. van Baten, R. Krishna, Entropy effects in adsorption and diffusion of alkane isomers in mordenite: An investigation using CBMC and MD simulations, Microporous Mesoporous Mater. 84 (2005) 179-191.

[22] R. Krishna, J.M. van Baten, Describing binary mixture diffusion in carbon nanotubes with the Maxwell-Stefan equations. An investigation using molecular dynamics simulations, Ind. Eng. Chem. Res. 45 (2006) 2084-2093.

[23] J.M. van Baten, R. Krishna, MD animations of diffusion in zeolites, University of Amsterdam, Amsterdam, http://www.science.uva.nl/research/cr/animateMD/, 21 December 2007.

[24] J. van den Bergh, W. Zhu, J.C. Groen, F. Kapteijn, J.A. Moulijn, K. Yajima, K. Nakayama, T. Tomita, S. Yoshida, Natural Gas Purification with a DDR Zeolite Membrane; Permeation Modelling with Maxwell-Stefan Equations, 15th International Zeolite Conference, Beijing, China, 2007.

[25] S. Himeno, T. Tomita, K. Suzuki, S. Yoshida, Characterization and selectivity for methane and carbon dioxide adsorption on the all-silica DD3R zeolite, Microporous Mesoporous Mater. 98 (2007) 62-69.

[26] W. Zhu, P. Hrabanek, L. Gora, F. Kapteijn, J.A. Moulijn, Role of Adsorption in the Permeation of CH_4 and CO_2 through a Silicalite-1Membrane, Ind. Eng. Chem. Res. 45 (2006) 767-776.

[27] M.S. Sun, D.B. Shah, H.H. Xu, O. Talu, Adsorption equilibria of C_1 to C_4 alkanes, CO_2, and SF_6 on silicalite, J. Phys. Chem. B 102 (1998) 1466-1473.

[28] T.C. Golden, S. Sircar, Gas Adsorption on Silicalite, J. Colloid Interface Sci. 162 (1994) 182-188.

[29] M. Kishima, H. Mizuhata, T. Okubo, Effects of Confinement on the Adsorption Behavior of Methane in High-Silica Zeolites, J. Phys. Chem. B 110 (2006) 13889-13896.

[30] C. Martin, N. Tosi-Pellenq, J. Patarin, J.P. Coulomb, Sorption Properties of $AlPO_4$-5 and SAPO-5 Zeolite-like Materials, Langmuir 14 (1998) 1774-1778.

[31] A. Hirotani, K. Mizukami, R. Miura, H. Takaba, T. Miya, A. Fahmi, A. Stirling, M. Kubo, A. Miiyamoto, Grand canonical Monte Carlo simulation of the adsorption of CO_2 on silcalite and NaZSM-5, App. Surf. Sci. 120 (1997) 81-84.

[32] T. Yamazaki, M. Katoh, S. Ozawa, Y. Ogino, Adsorption of CO_2 over univalent cation-exchanged ZSM-5 zeolites, Mol. Phys. 80 (1993) 313-324.

[33] J.A. Dunne, R. Mariwala, M. Rao, S. Sircar, R.J. Gorte, A.L. Myers, Calorimetric Heats of Adsorption and Adsorption Isotherms. 1. O_2, N_2, Ar, CO_2, CH_4, C_2H_6, and SF_6 on Silicalite, Langmuir 12 (1996) 5888-5895.

Table 1. Summary of force field used in GCMC and MD simulations

The interaction between adsorbates was calculated using Lennard-Jones potentials and electrostatic interactions using an Ewald summation method. For adsorbate-adsorbate interactions, Lorentz-Berthelot mixing rules were applied for σ and ε/k_B. Leonard-Jones interaction with the zeolite was only taken σ and ε/k_B and epsilon for the adsorbates and for the interaction with the adsorbates and with the zeolites. The charges are also shown for the pseudo atoms.

(pseudo-) atom	Atom-atom σ / Å	Atom-atom ε/k_B / K	Atom - O in zeolite σ / Å	Atom - O in zeolite ε/k_B / K	charge
CH_4	3.72	158.5	3.47	115	0
C (CO_2)	2.757	28.129	2.7815	50.2	0.6512
O (CO_2)	3.033	80.507	2.9195	84.93	-0.3256
N (N_2)	3.32	36.4	3.06	58.25	-0.40484
He	2.28	10.223	2.62	51.235	0
Ar	3.42	124.07	3.17	95.61	0
Ne	2.789	35.7	2.798	56.87	0
Kr	3.636	166.4	3.45	109.6	0
H_2	2.782	38.7	2.713	79.914	0

The molecule geometries were fixed. The bond angle for CO_2 is 180°. For N_2, a point charge is located in the middle between the two atoms, that is twice the magnitude of the charges on N, and opposite in sign, so that the total molecule charge is zero. The following table shows the bond lengths that were used:

bond	bond length / Å
N-N (N_2)	1.098
C-O (CO_2)	1.16

The zeolite atoms are considered immobile. The following table shows the charges used for the zeolite atoms:

atom	charge
$O_{Zeolite}$	-1.025
$Si_{Zeolite}$	2.05

4. Captions for Figures

Figure 1. Comparison of GCMC simulations for pure component isotherms for CH_4 in DDR with experimental data of Van den Bergh et al.[24] and Himeno [25].

Figure 2. Comparison of GCMC simulations for pure component isotherms for CH_4 in MFI with experimental data of Zhu et al.[26], Sun et al.[27], Golden and Sircar[28] and Kishima et al.[29].

Figure 3. Comparison of GCMC simulations for pure component isotherms for CH_4 in AFI with experimental data of Martin et al.[30]

Figure 4. Comparison of GCMC simulations for pure component isotherms for CO_2 in DDR with experimental data of Van den Bergh et al.[24] and Himeno [25].

Figure 5. Comparison of GCMC simulations for pure component isotherms for CO_2 in MFI with experimental data of Zhu et al.[26], Sun et al.[27], Choudhary and Mayadevi[27], Hirotani et al.[31], Yamazaki et al.[32], Golden and Sircar[28], and Dunne et al.[33].

Figure 6. Comparison of GCMC simulations for pure component isotherms for N_2 in DDR with experimental data of Van den Bergh et al.[24].

Figure 7. Comparison of GCMC simulations for pure component isotherms for N_2 in MFI with experimental data of Golden and Sircar[28] and Dunne et al.[33].

Figure 8. Comparison of GCMC simulations for pure component isotherms for Ar in MFI with experimental data of Golden and Sircar[28] and Dunne et al.[33].

Figure 9. Comparison of GCMC simulations for pure component isotherms for Kr in MFI with experimental data of Golden and Sircar[28].

DDR, CH4

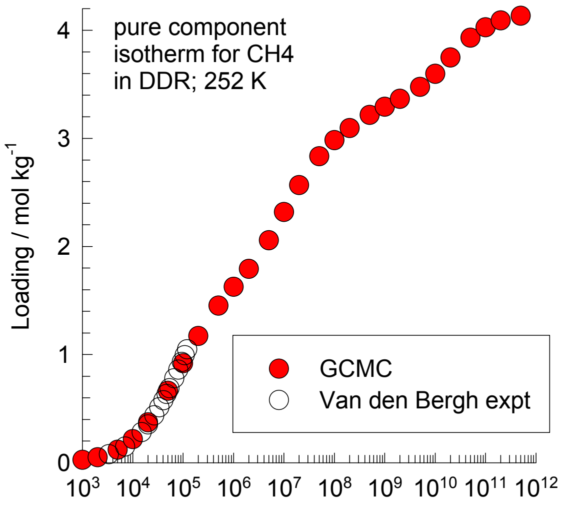
pure component
isotherm for CH4
in DDR; 252 K
Loading / mol kg^{-1}
0
1
2
3
4
10^3 10^4 10^5 10^6 10^7 10^8 10^9 10^{10} 10^{11} 10^{12}
GCMC
Van den Bergh expt

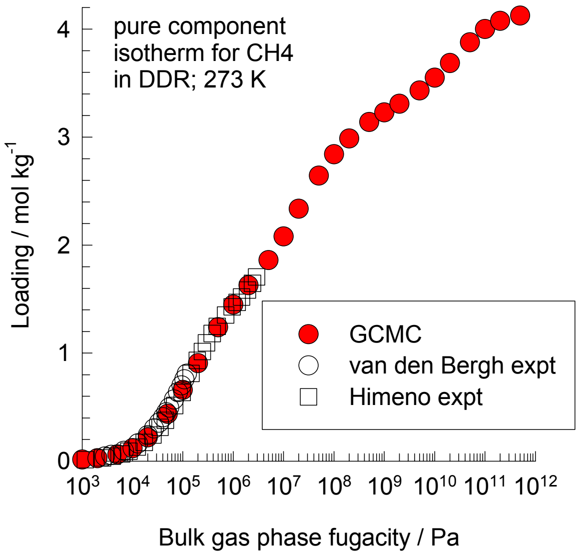
pure component
isotherm for CH4
in DDR; 273 K
Loading / mol kg^{-1}
0
1
2
3
4
10^3 10^4 10^5 10^6 10^7 10^8 10^9 10^{10} 10^{11} 10^{12}
Bulk gas phase fugacity / Pa
GCMC
van den Bergh expt
Himeno expt

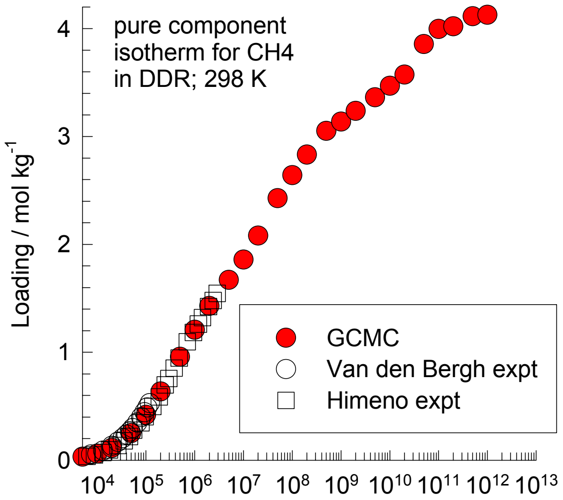
pure component
isotherm for CH4
in DDR; 298 K
Loading / mol kg^{-1}
0
1
2
3
4
10^4 10^5 10^6 10^7 10^8 10^9 10^{10} 10^{11} 10^{12} 10^{13}
GCMC
Van den Bergh expt
Himeno expt

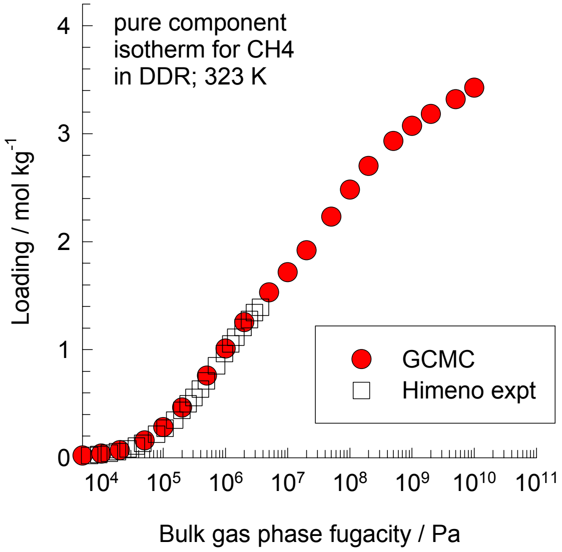
pure component
isotherm for CH4
in DDR; 323 K
Loading / mol kg^{-1}
0
1
2
3
4
10^4 10^5 10^6 10^7 10^8 10^9 10^{10} 10^{11}
Bulk gas phase fugacity / Pa
GCMC
Himeno expt

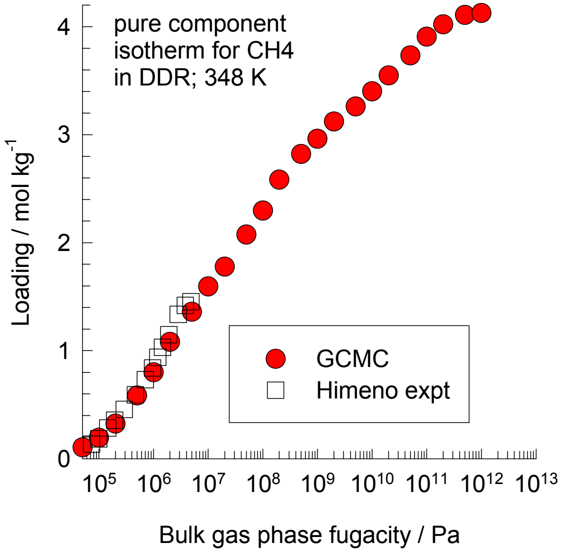
pure component
isotherm for CH4
in DDR; 348 K
Loading / mol kg^{-1}
0
1
2
3
4
10^5 10^6 10^7 10^8 10^9 10^{10} 10^{11} 10^{12} 10^{13}
Bulk gas phase fugacity / Pa
GCMC
Himeno expt

MFI, CH4

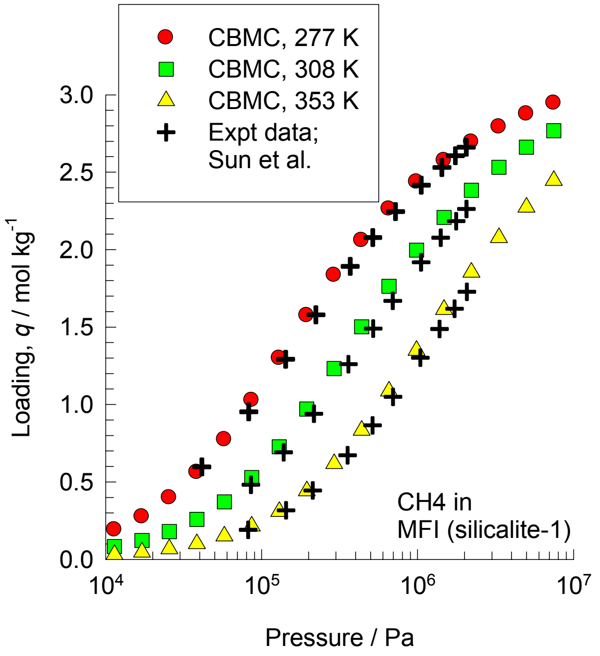
CBMC, 277 K
CBMC, 308 K
CBMC, 353 K
Expt data;
Sun et al.
CH4 in
MFI (silicalite-1)
Loading, q / mol kg^{-1}
0.0
0.5
1.0
1.5
2.0
2.5
3.0
10^4
10^5
10^6
10^7
Pressure / Pa

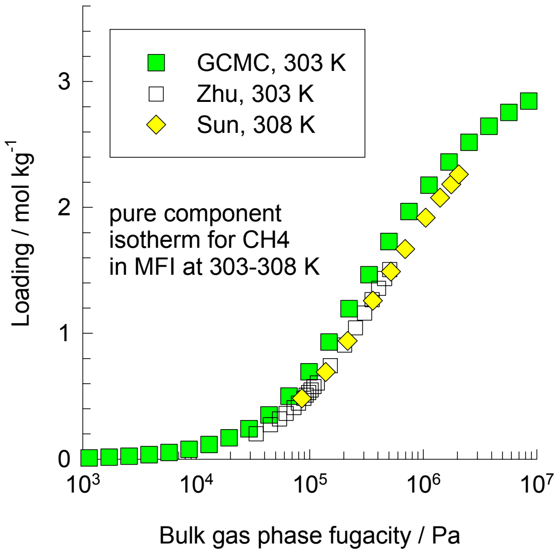
GCMC, 303 K
Zhu, 303 K
Sun, 308 K
pure component
isotherm for CH4
in MFI at 303-308 K
Loading / mol kg^{-1}
0
1
2
3
10^3
10^4
10^5
10^6
10^7
Bulk gas phase fugacity / Pa

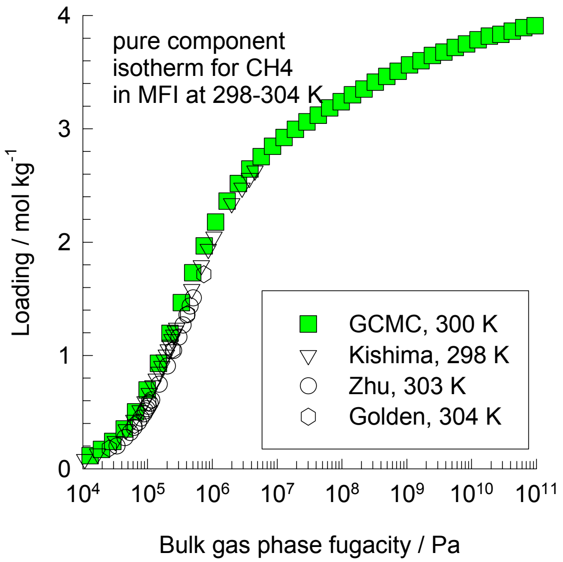
pure component
isotherm for CH4
in MFI at 298-304 K
GCMC, 300 K
Kishima, 298 K
Zhu, 303 K
Golden, 304 K
Loading / mol kg^{-1}
0
1
2
3
4
10^4
10^5
10^6
10^7
10^8
10^9
10^{10}
10^{11}
Bulk gas phase fugacity / Pa

AFI, CH4

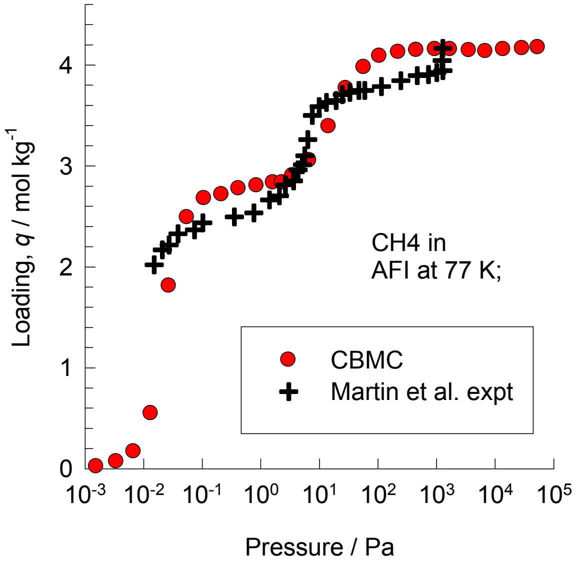
Loading, q / mol kg-1
0
1
2
3
4
10-3
10-2
10-1
100
101
102
103
104
105
Pressure / Pa
CH4 in
AFI at 77 K;
CBMC
Martin et al. expt

DDR, CO2

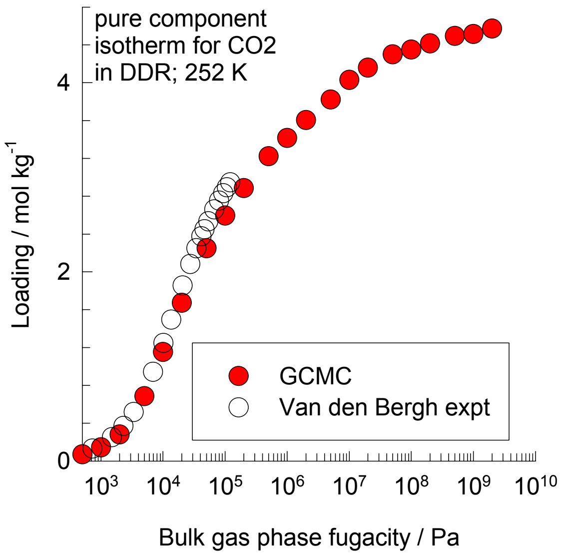
pure component
isotherm for CO2
in DDR; 252 K
Loading / mol kg^{-1}
0
2
4
GCMC
Van den Bergh expt
10^3
10^4
10^5
10^6
10^7
10^8
10^9
10^{10}
Bulk gas phase fugacity / Pa

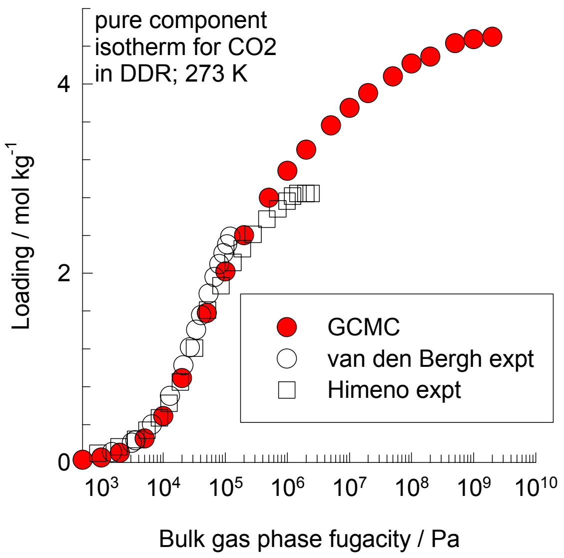
pure component
isotherm for CO2
in DDR; 273 K
Loading / mol kg^{-1}
0
2
4
GCMC
van den Bergh expt
Himeno expt
10^3
10^4
10^5
10^6
10^7
10^8
10^9
10^{10}
Bulk gas phase fugacity / Pa

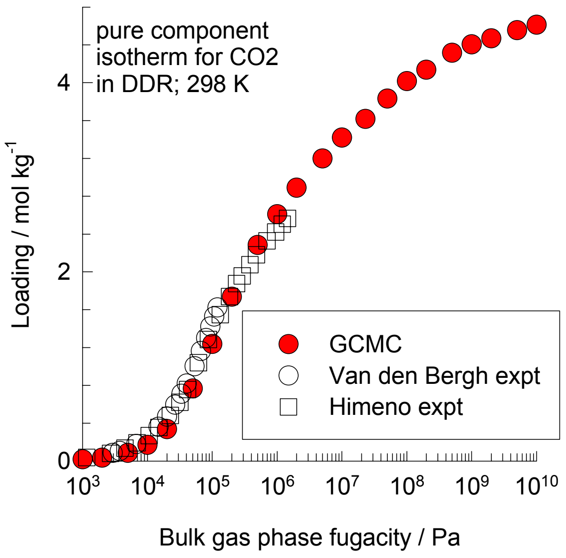
pure component
isotherm for CO2
in DDR; 298 K
Loading / mol kg^{-1}
0
2
4
GCMC
Van den Bergh expt
Himeno expt
10^3
10^4
10^5
10^6
10^7
10^8
10^9
10^{10}
Bulk gas phase fugacity / Pa

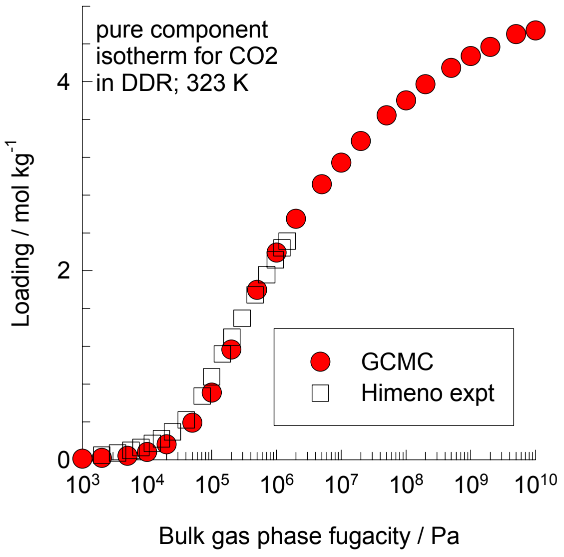
pure component
isotherm for CO2
in DDR; 323 K
Loading / mol kg^{-1}
0
2
4
GCMC
Himeno expt
10^3
10^4
10^5
10^6
10^7
10^8
10^9
10^{10}
Bulk gas phase fugacity / Pa

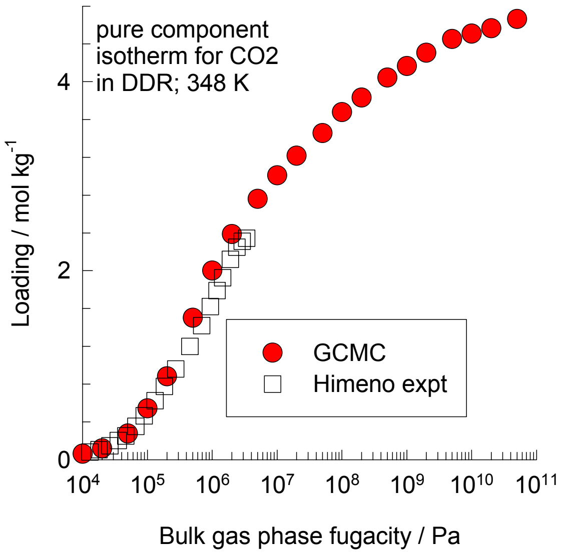
pure component
isotherm for CO2
in DDR; 348 K
Loading / mol kg^{-1}
0
2
4
GCMC
Himeno expt
10^4
10^5
10^6
10^7
10^8
10^9
10^{10}
10^{11}
Bulk gas phase fugacity / Pa

MFI, CO2

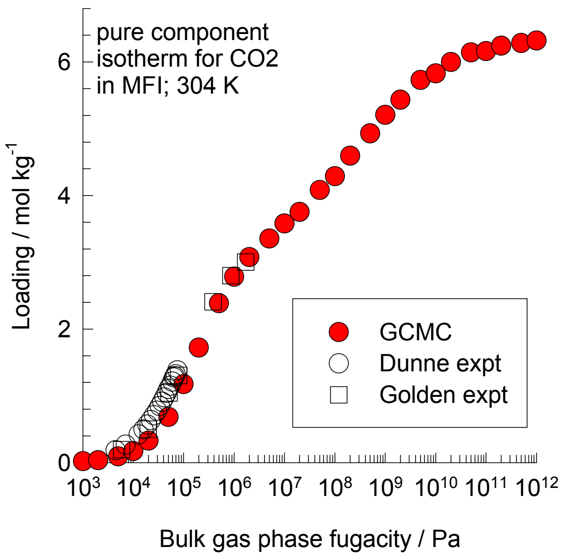
pure component
isotherm for CO2
in MFI; 304 K
GCMC
Dunne expt
Golden expt
Loading / mol kg^{-1}
0
2
4
6
10^3 10^4 10^5 10^6 10^7 10^8 10^9 10^{10} 10^{11} 10^{12}
Bulk gas phase fugacity / Pa

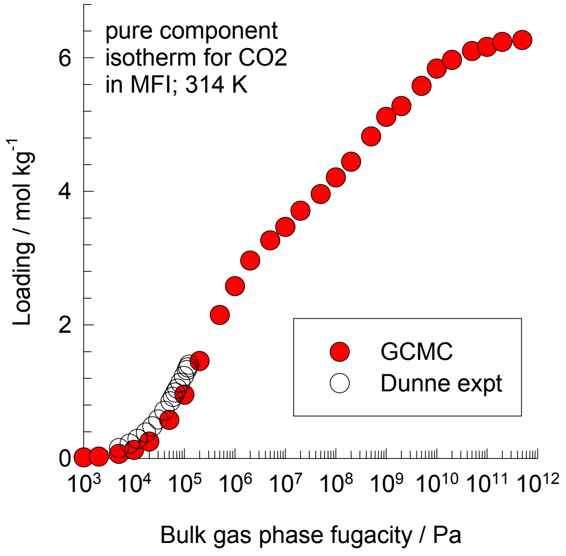
pure component
isotherm for CO2
in MFI; 314 K
GCMC
Dunne expt
Loading / mol kg^{-1}
0
2
4
6
10^3 10^4 10^5 10^6 10^7 10^8 10^9 10^{10} 10^{11} 10^{12}
Bulk gas phase fugacity / Pa

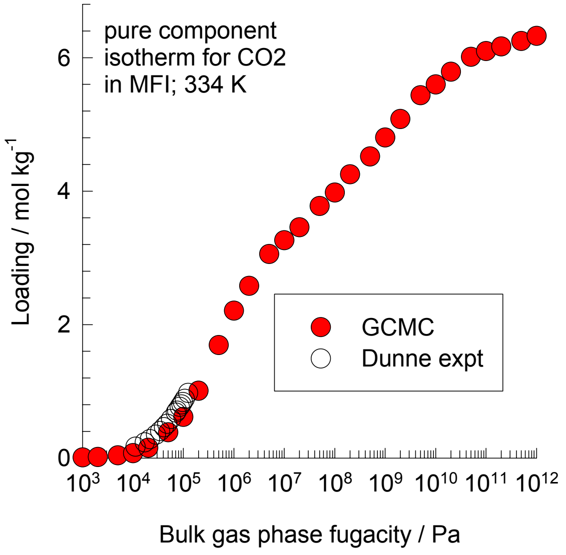
pure component
isotherm for CO2
in MFI; 334 K
GCMC
Dunne expt
Loading / mol kg^{-1}
0
2
4
6
10^3 10^4 10^5 10^6 10^7 10^8 10^9 10^{10} 10^{11} 10^{12}
Bulk gas phase fugacity / Pa

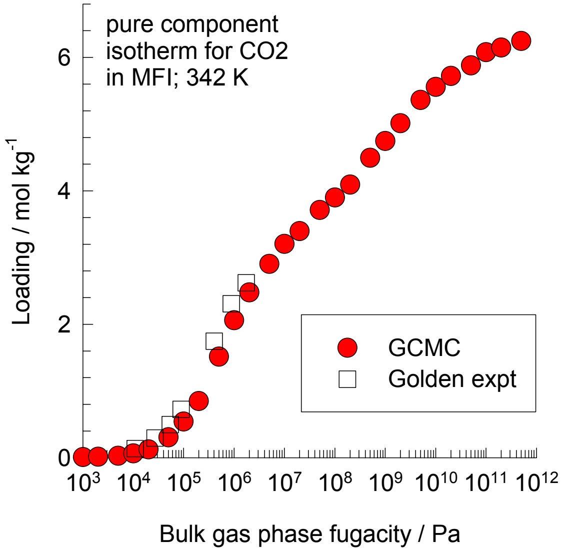
pure component
isotherm for CO2
in MFI; 342 K
GCMC
Golden expt
Loading / mol kg^{-1}
0
2
4
6
10^3 10^4 10^5 10^6 10^7 10^8 10^9 10^{10} 10^{11} 10^{12}
Bulk gas phase fugacity / Pa

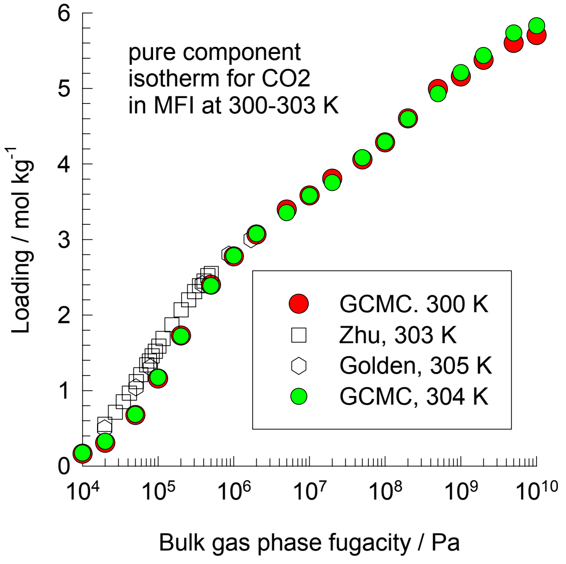
pure component
isotherm for CO2
in MFI at 300-303 K
GCMC. 300 K
Zhu, 303 K
Golden, 305 K
GCMC, 304 K
Loading / mol kg^{-1}
0
1
2
3
4
5
6
10^4 10^5 10^6 10^7 10^8 10^9 10^{10}
Bulk gas phase fugacity / Pa

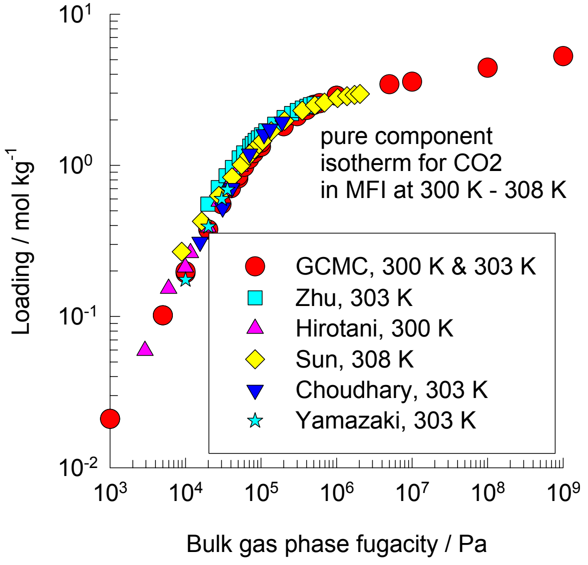
pure component
isotherm for CO2
in MFI at 300 K - 308 K
GCMC, 300 K & 303 K
Zhu, 303 K
Hirotani, 300 K
Sun, 308 K
Choudhary, 303 K
Yamazaki, 303 K
Loading / mol kg^{-1}
10^{-2}
10^{-1}
10^0
10^1
10^3 10^4 10^5 10^6 10^7 10^8 10^9
Bulk gas phase fugacity / Pa

DDR, N2

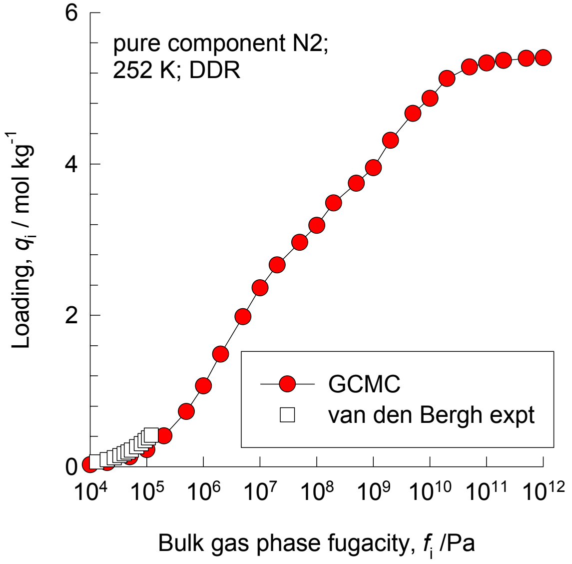

pure component N2;
252 K; DDR
Loading, q_i / mol kg^{-1}
0
2
4
6
GCMC
van den Bergh expt
10^4 10^5 10^6 10^7 10^8 10^9 10^{10} 10^{11} 10^{12}
Bulk gas phase fugacity, f_i /Pa

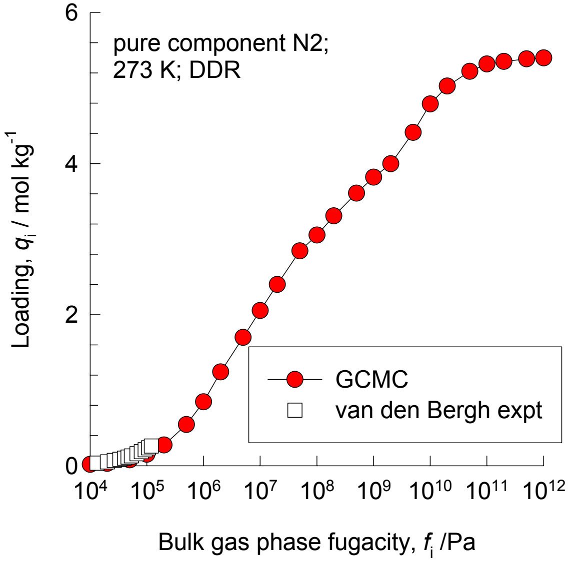

pure component N2;
273 K; DDR
Loading, q_i / mol kg^{-1}
0
2
4
6
GCMC
van den Bergh expt
10^4 10^5 10^6 10^7 10^8 10^9 10^{10} 10^{11} 10^{12}
Bulk gas phase fugacity, f_i /Pa

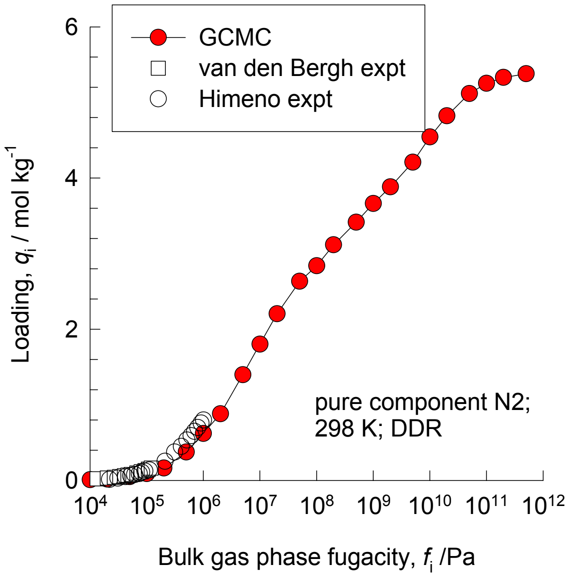

GCMC
van den Bergh expt
Himeno expt
Loading, q_i / mol kg^{-1}
0
2
4
6
pure component N2;
298 K; DDR
10^4 10^5 10^6 10^7 10^8 10^9 10^{10} 10^{11} 10^{12}
Bulk gas phase fugacity, f_i /Pa

MFI, N2

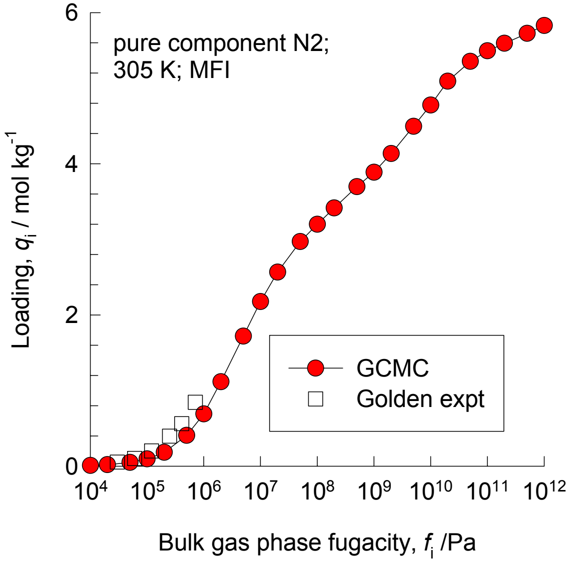
pure component N2;
305 K; MFI
GCMC
Golden expt
Loading, q_i / mol kg^{-1}
Bulk gas phase fugacity, f_i /Pa
0
2
4
6
10^4
10^5
10^6
10^7
10^8
10^9
10^{10}
10^{11}
10^{12}

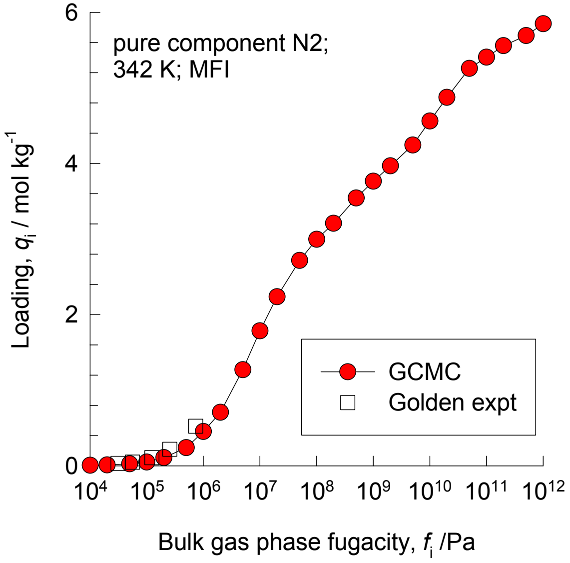
pure component N2;
342 K; MFI
GCMC
Golden expt
Loading, q_i / mol kg^{-1}
Bulk gas phase fugacity, f_i /Pa
0
2
4
6
10^4
10^5
10^6
10^7
10^8
10^9
10^{10}
10^{11}
10^{12}

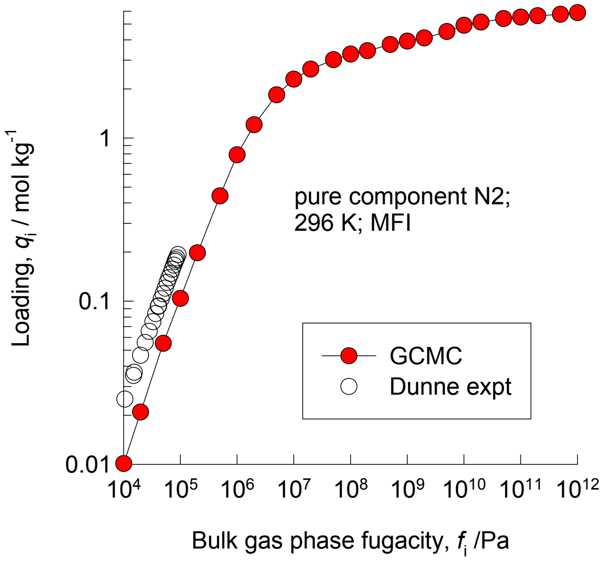
pure component N2;
296 K; MFI
GCMC
Dunne expt
Loading, q_i / mol kg^{-1}
Bulk gas phase fugacity, f_i /Pa
0.01
0.1
1
10^4
10^5
10^6
10^7
10^8
10^9
10^{10}
10^{11}
10^{12}

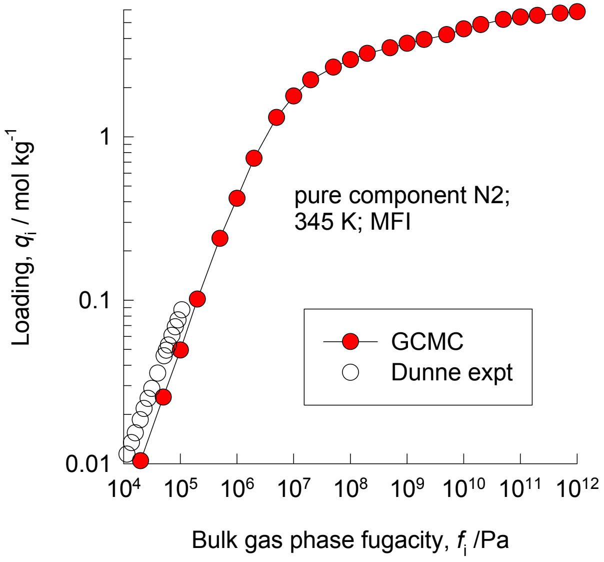
pure component N2;
345 K; MFI
GCMC
Dunne expt
Loading, q_i / mol kg^{-1}
Bulk gas phase fugacity, f_i /Pa
0.01
0.1
1
10^4
10^5
10^6
10^7
10^8
10^9
10^{10}
10^{11}
10^{12}

MFI, Ar

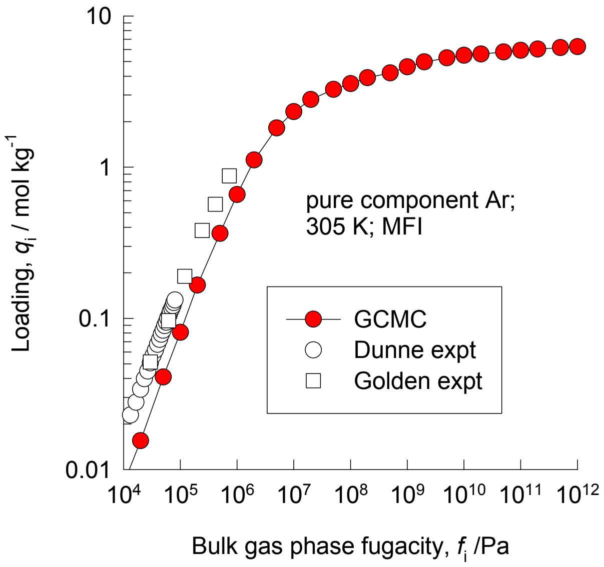

pure component Ar;
305 K; MFI
GCMC
Dunne expt
Golden expt
Loading, q_i / mol kg^{-1}
10
1
0.1
0.01
10^4
10^5
10^6
10^7
10^8
10^9
10^{10}
10^{11}
10^{12}
Bulk gas phase fugacity, f_i /Pa

MFI, Kr

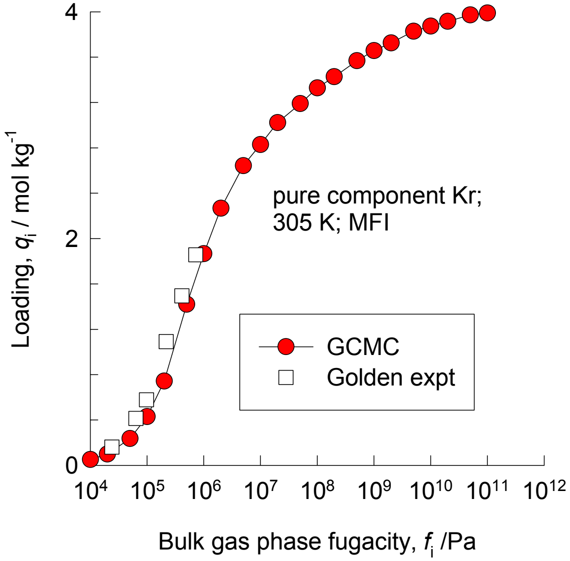
Loading, q_i / mol kg^{-1}
0
2
4
10^4
10^5
10^6
10^7
10^8
10^9
10^{10}
10^{11}
10^{12}
Bulk gas phase fugacity, f_i /Pa
pure component Kr;
305 K; MFI
GCMC
Golden expt

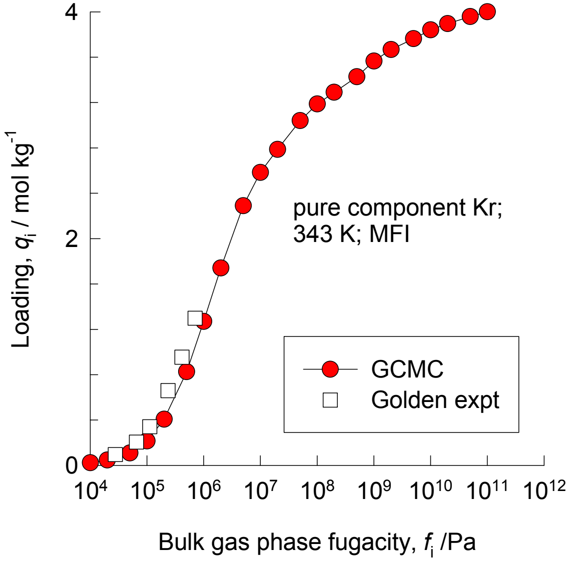
Loading, q_i / mol kg^{-1}
0
2
4
10^4
10^5
10^6
10^7
10^8
10^9
10^{10}
10^{11}
10^{12}
Bulk gas phase fugacity, f_i /Pa
pure component Kr;
343 K; MFI
GCMC
Golden expt

Appendix A2

GCMC and MD simulation results for adsorption and diffusion of variety of molecules in different zeolite structures

CHA, 300 K, CH4

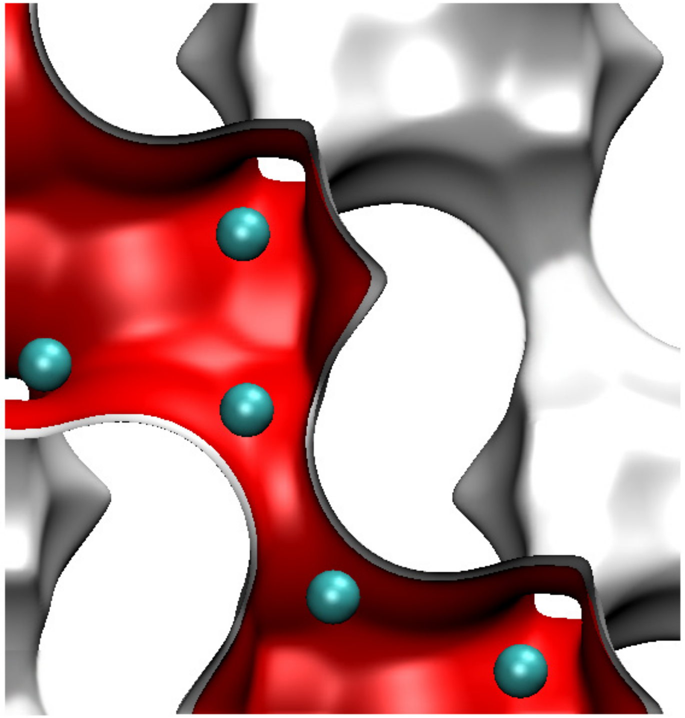

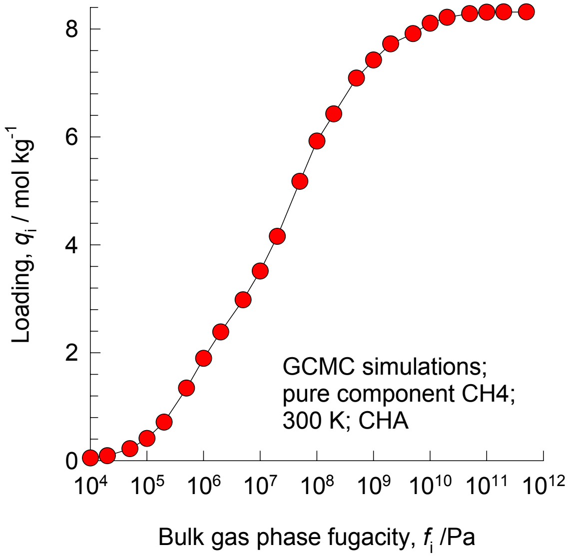
8
6
4
2
0
Loading, q_i / mol kg^{-1}
10^4
10^5
10^6
10^7
10^8
10^9
10^{10}
10^{11}
10^{12}
Bulk gas phase fugacity, f_i /Pa
GCMC simulations;
pure component CH4;
300 K; CHA

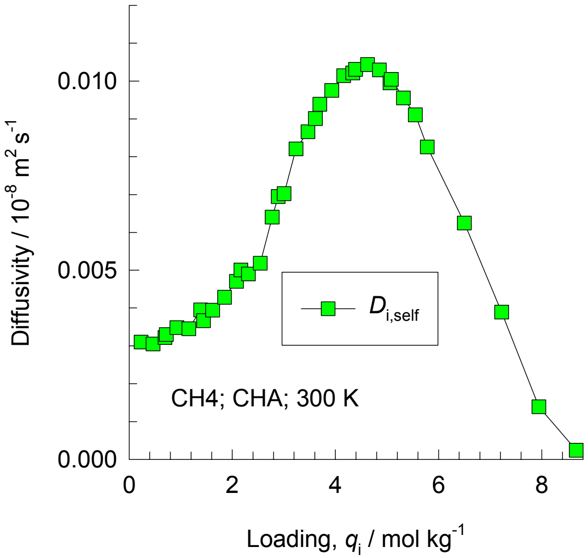
0.010
0.005
0.000
Diffusivity / 10^{-8} m^2 s^{-1}
0
2
4
6
8
Loading, q_i / mol kg^{-1}
$D_{i,self}$
CH4; CHA; 300 K

CHA, 300 K, CO2

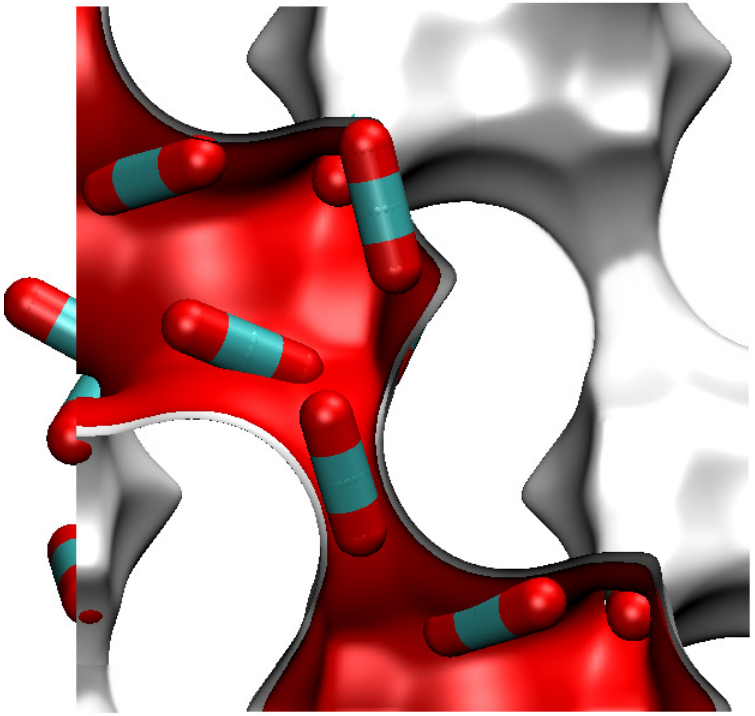

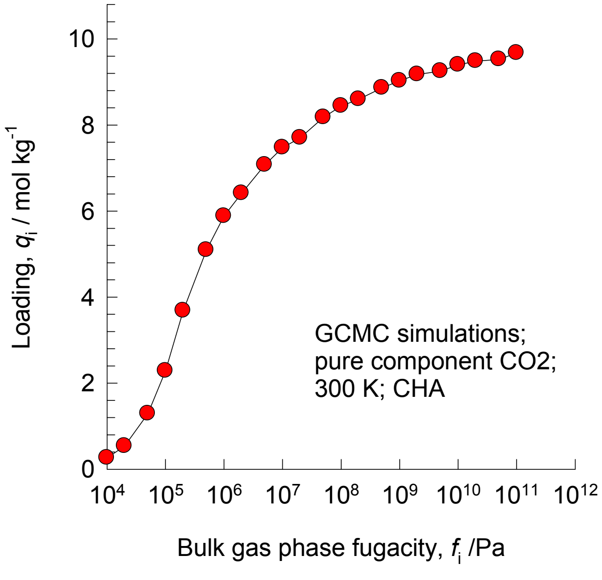

Loading, q_i / mol kg^{-1}
0
2
4
6
8
10
10^4
10^5
10^6
10^7
10^8
10^9
10^{10}
10^{11}
10^{12}
Bulk gas phase fugacity, f_i /Pa
GCMC simulations;
pure component CO2;
300 K; CHA

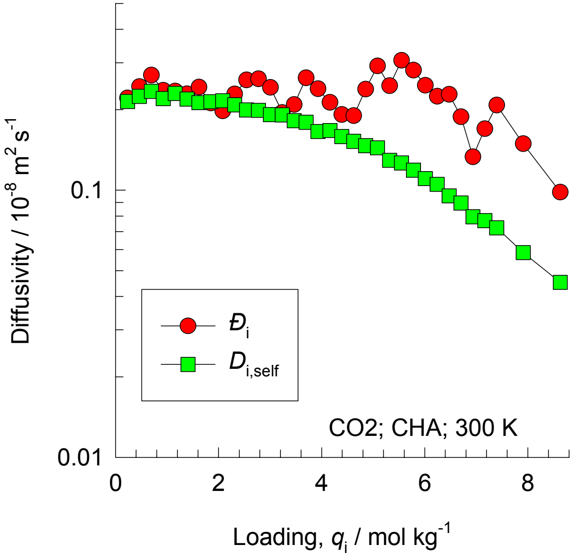

Diffusivity / 10^{-8} m^2 s^{-1}
0.01
0.1
$Đ_i$
$D_{i,self}$
CO2; CHA; 300 K
0
2
4
6
8
Loading, q_i / mol kg^{-1}

CHA, 300 K, N2

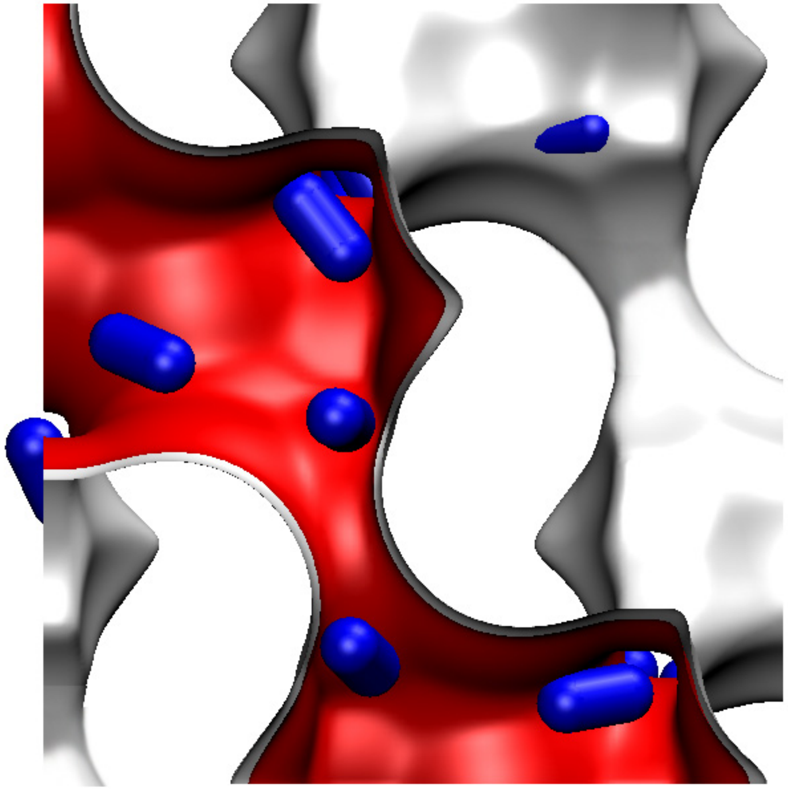

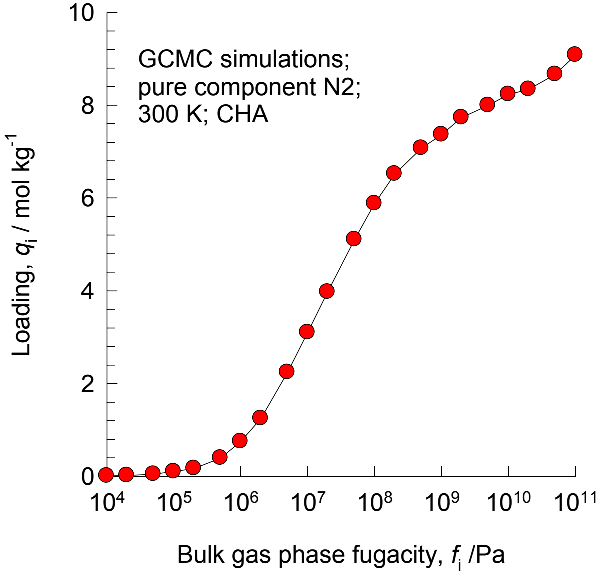
GCMC simulations;
pure component N2;
300 K; CHA
Loading, q_i / mol kg^{-1}
0
2
4
6
8
10
10^4
10^5
10^6
10^7
10^8
10^9
10^{10}
10^{11}
Bulk gas phase fugacity, f_i /Pa

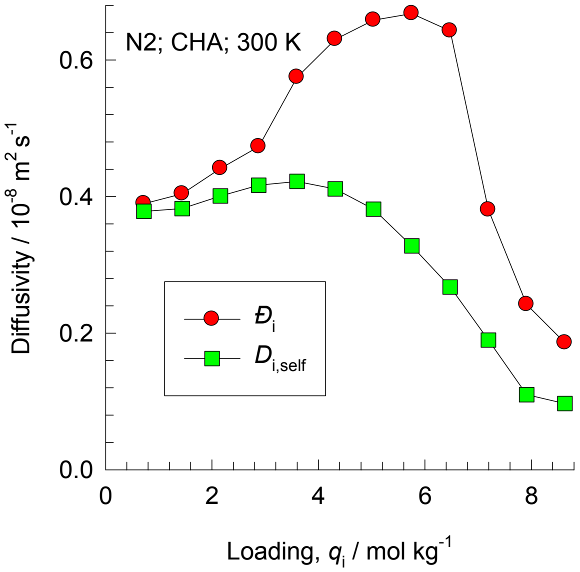
N2; CHA; 300 K
Diffusivity / 10^{-8} m^2 s^{-1}
0.0
0.2
0.4
0.6
0
2
4
6
8
$Đ_i$
$D_{i,self}$
Loading, q_i / mol kg^{-1}

CHA, 300 K, Ar

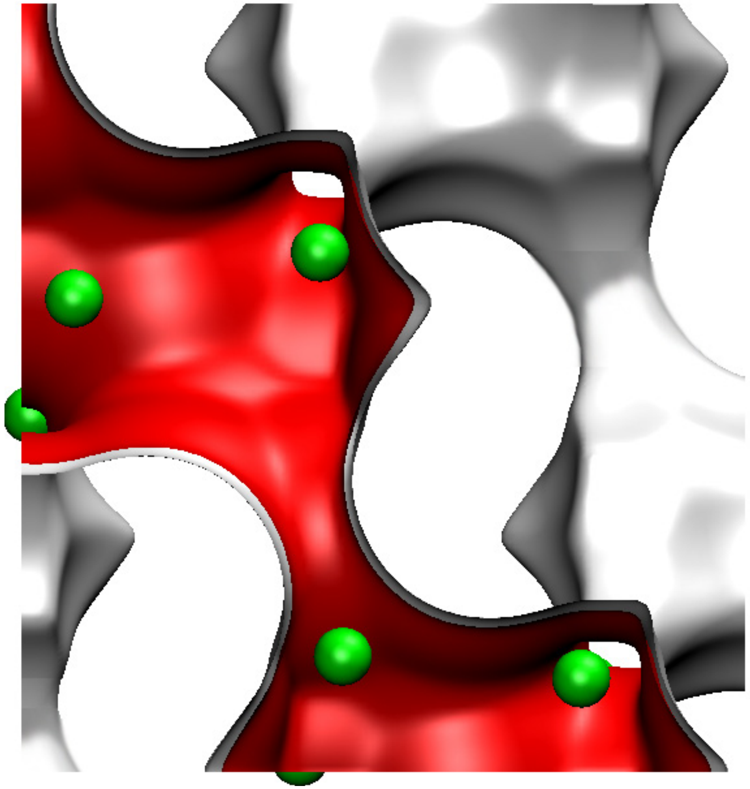

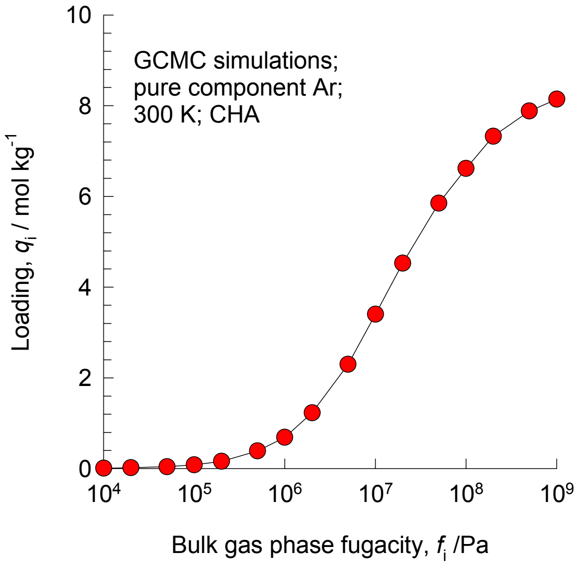
GCMC simulations;
pure component Ar;
300 K; CHA
Loading, q_i / mol kg^{-1}
Bulk gas phase fugacity, f_i /Pa
0
2
4
6
8
10
10^4
10^5
10^6
10^7
10^8
10^9

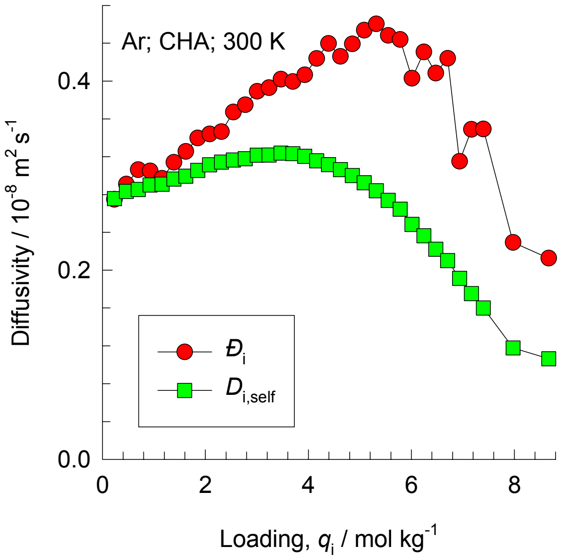
Ar; CHA; 300 K
Diffusivity / 10^{-8} m^2 s^{-1}
Loading, q_i / mol kg^{-1}
$Đ_i$
$D_{i,self}$
0.0
0.2
0.4
0
2
4
6
8

CHA, 300 K, Ar, sensitivity to force field perturbations

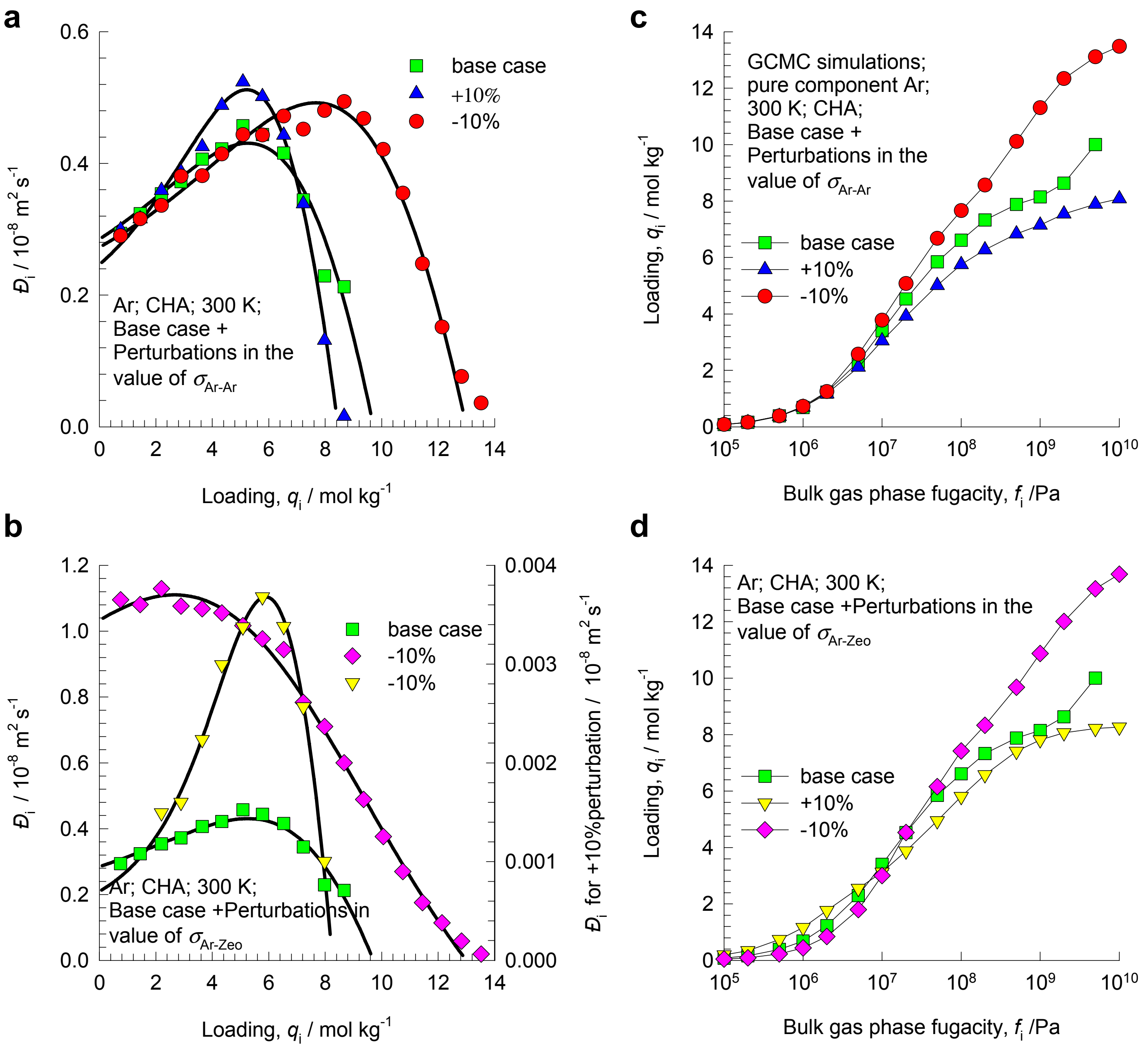

CHA, 300 K, Kr

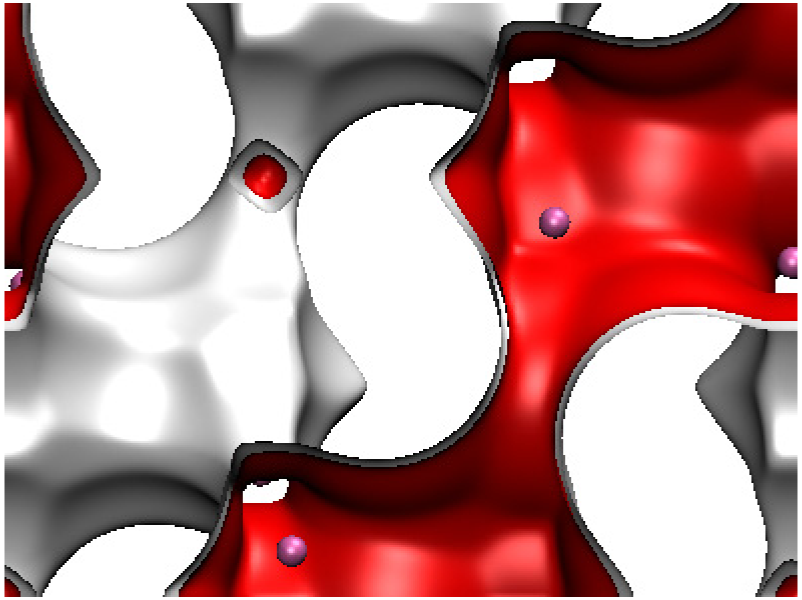

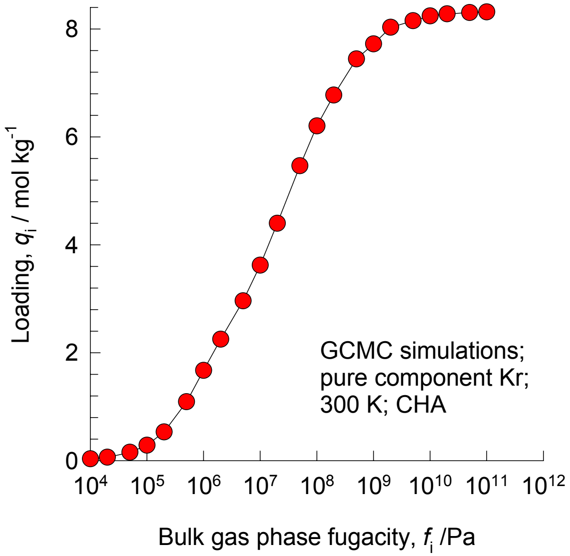

Loading, q_i / mol kg^{-1}
0
2
4
6
8
10^4
10^5
10^6
10^7
10^8
10^9
10^{10}
10^{11}
10^{12}
Bulk gas phase fugacity, f_i /Pa
GCMC simulations;
pure component Kr;
300 K; CHA

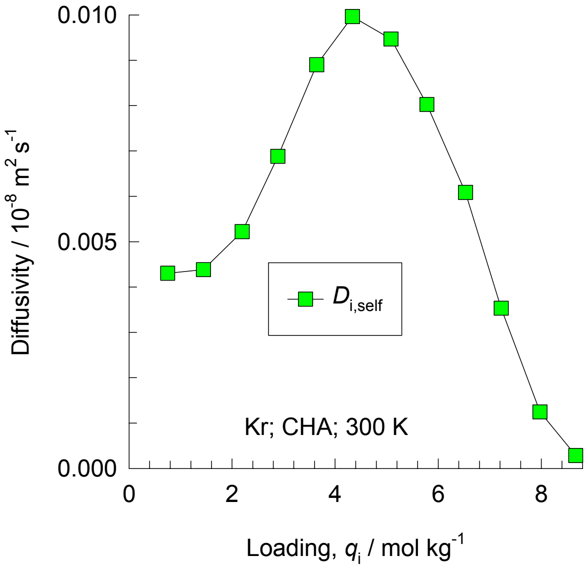

Diffusivity / 10^{-8} m^2 s^{-1}
0.010
0.005
0.000
0
2
4
6
8
Loading, q_i / mol kg^{-1}
$D_{i,self}$
Kr; CHA; 300 K

CHA, 300 K, Ne

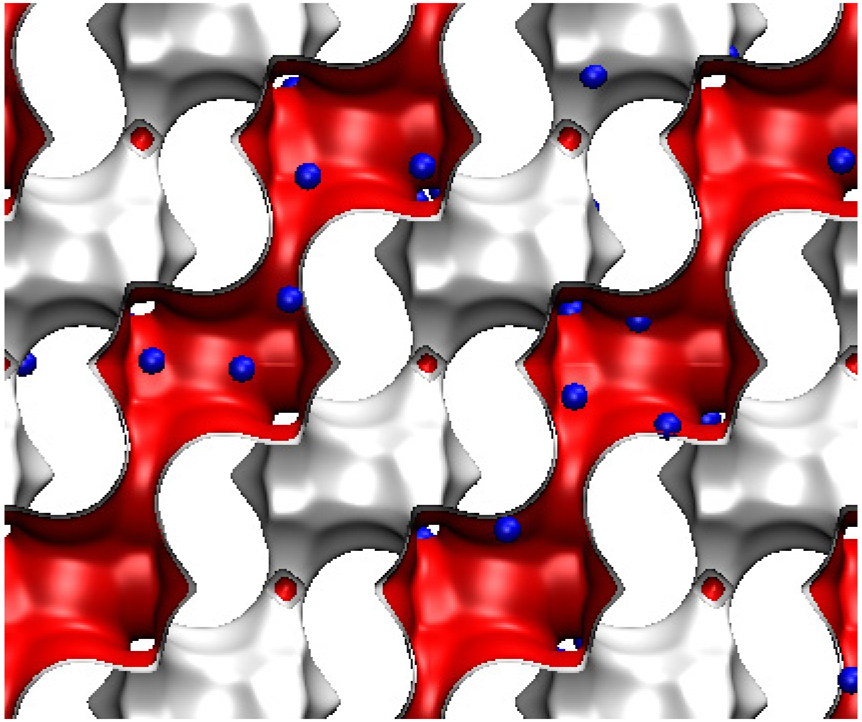

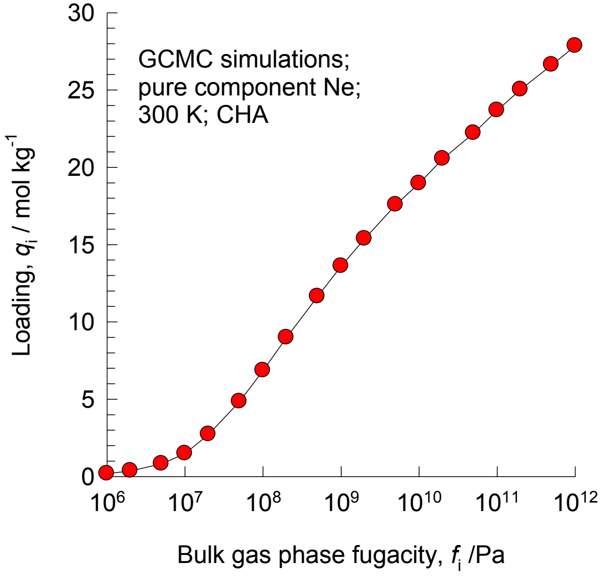
GCMC simulations;
pure component Ne;
300 K; CHA
Loading, q_i / mol kg^{-1}
0
5
10
15
20
25
30
10^6
10^7
10^8
10^9
10^{10}
10^{11}
10^{12}
Bulk gas phase fugacity, f_i /Pa

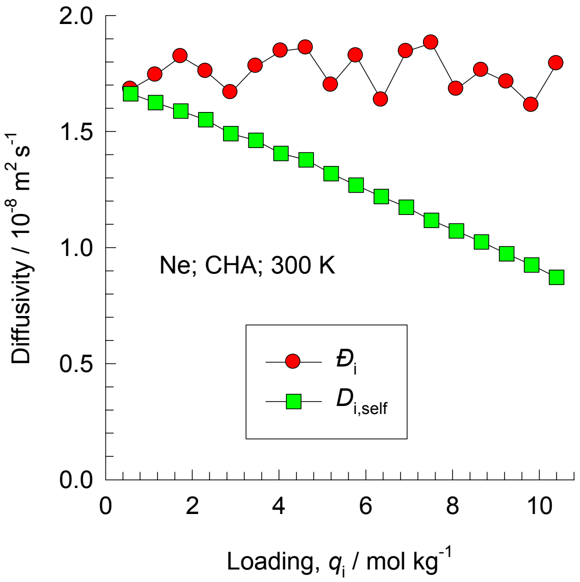
Diffusivity / 10^{-8} m^2 s^{-1}
0.0
0.5
1.0
1.5
2.0
0
2
4
6
8
10
Loading, q_i / mol kg^{-1}
Ne; CHA; 300 K
$Đ_i$
$D_{i,self}$

CHA, 300 K, He

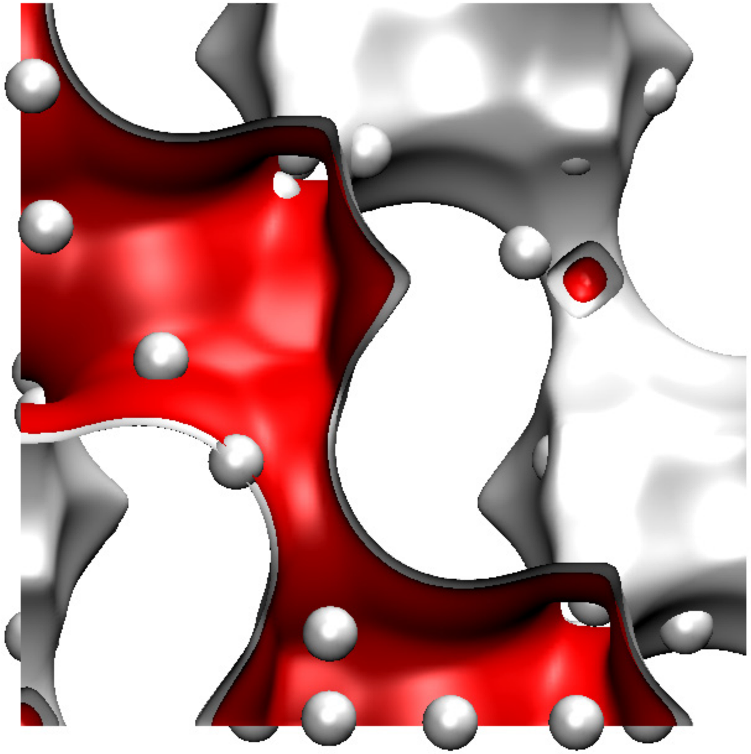

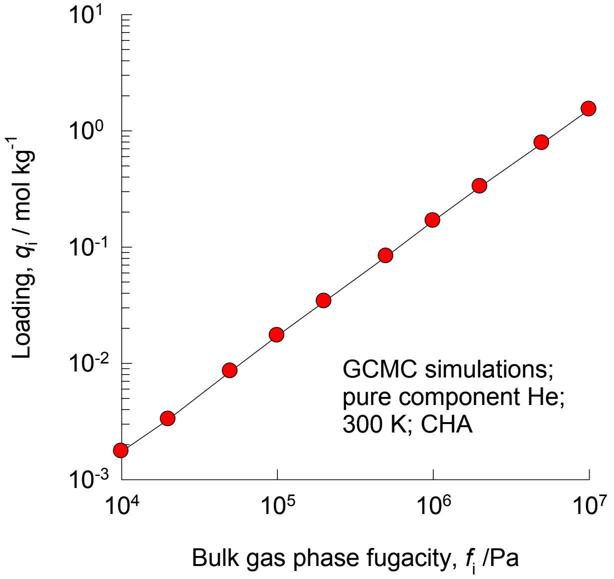

Loading, q_i / mol kg^{-1}
10^1
10^0
10^{-1}
10^{-2}
10^{-3}
10^4
10^5
10^6
10^7
Bulk gas phase fugacity, f_i /Pa
GCMC simulations;
pure component He;
300 K; CHA

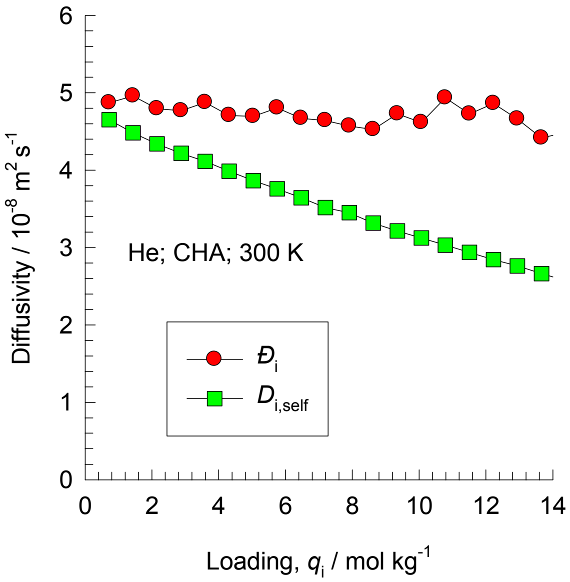

Diffusivity / 10^{-8} m^2 s^{-1}
6
5
4
3
2
1
0
He; CHA; 300 K
$Đ_i$
$D_{i,\text{self}}$
0
2
4
6
8
10
12
14
Loading, q_i / mol kg^{-1}

CHA, 300 K, H2

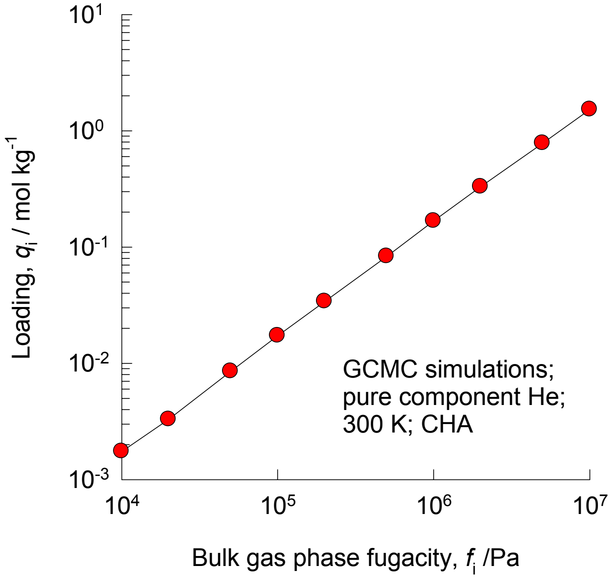
10^1
10^0
10^{-1}
10^{-2}
10^{-3}
Loading, q_i / mol kg^{-1}
GCMC simulations;
pure component He;
300 K; CHA
10^4
10^5
10^6
10^7
Bulk gas phase fugacity, f_i /Pa

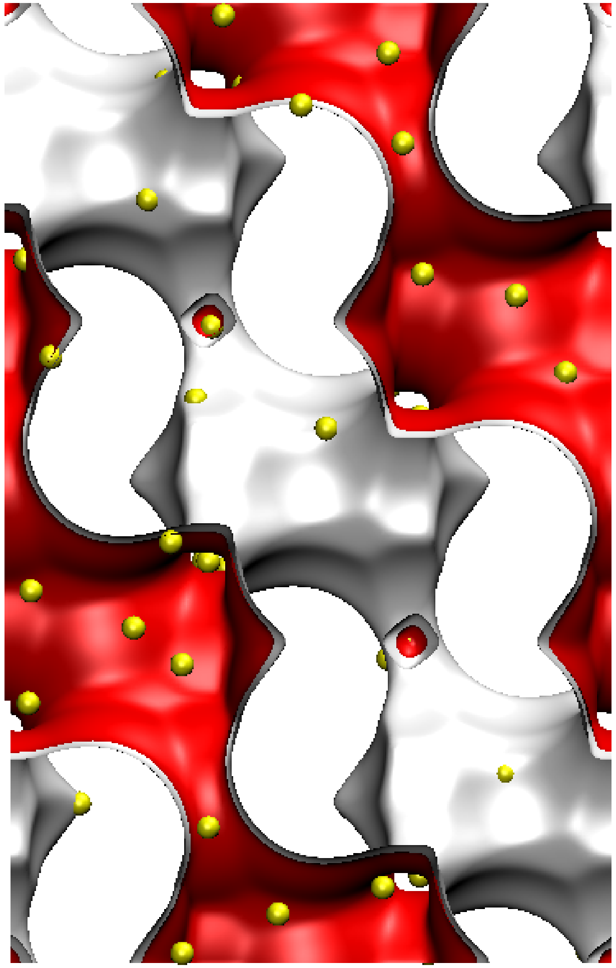

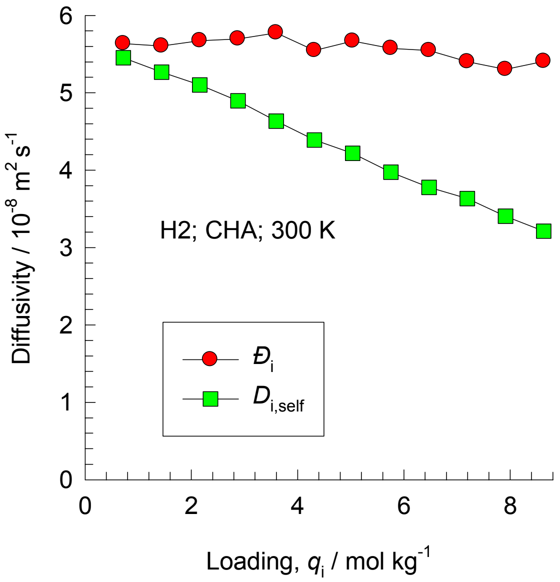
6
5
4
3
2
1
0
Diffusivity / 10^{-8} m^2 s^{-1}
H2; CHA; 300 K
$Đ_i$
$D_{i,self}$
0
2
4
6
8
Loading, q_i / mol kg^{-1}

DDR, 300 K, CH4

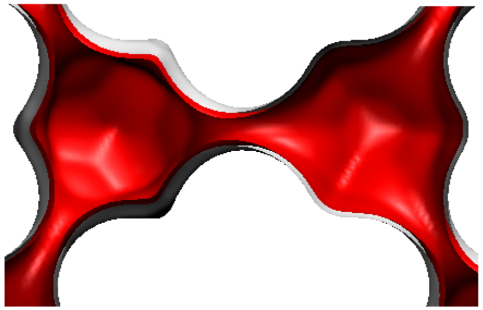

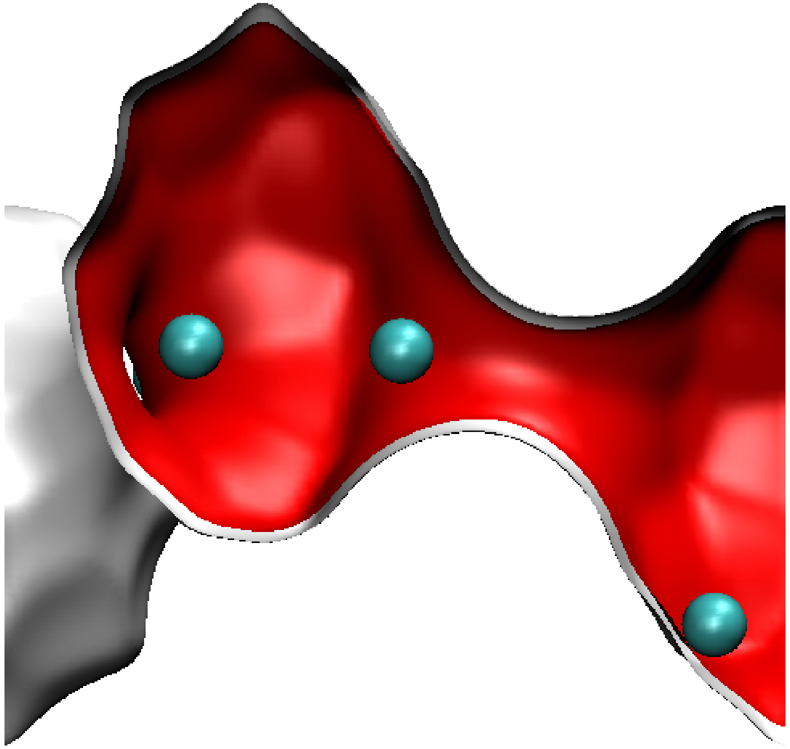

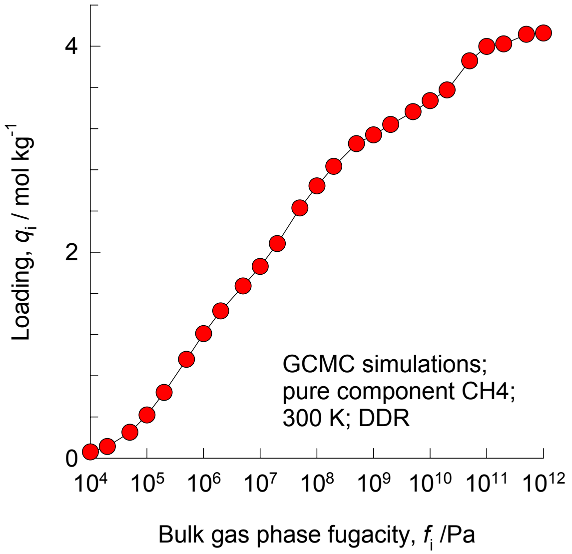

Loading, q_i / mol kg^{-1}
0
2
4
10^4
10^5
10^6
10^7
10^8
10^9
10^{10}
10^{11}
10^{12}
Bulk gas phase fugacity, f_i /Pa
GCMC simulations;
pure component CH4;
300 K; DDR

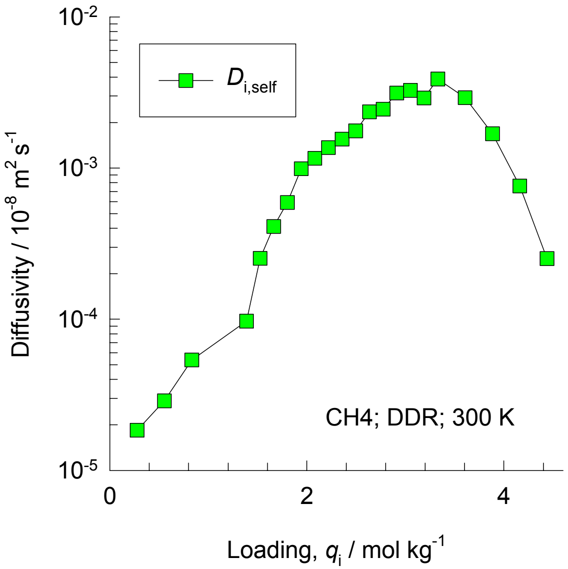

Diffusivity / 10^{-8} m^2 s^{-1}
10^{-2}
10^{-3}
10^{-4}
10^{-5}
$D_{i,self}$
CH4; DDR; 300 K
0
2
4
Loading, q_i / mol kg^{-1}

DDR, 300 K, CO2

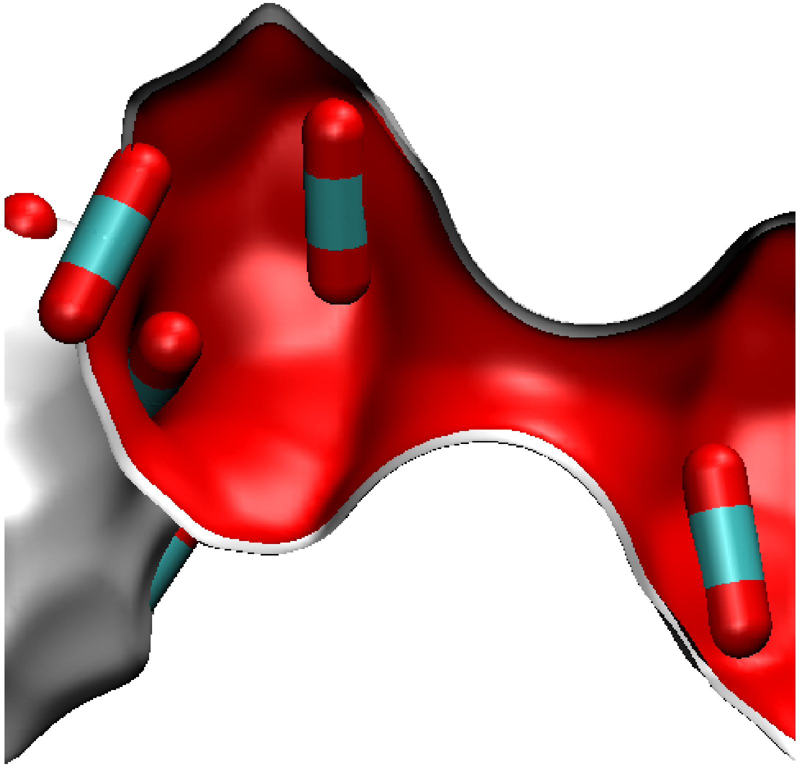

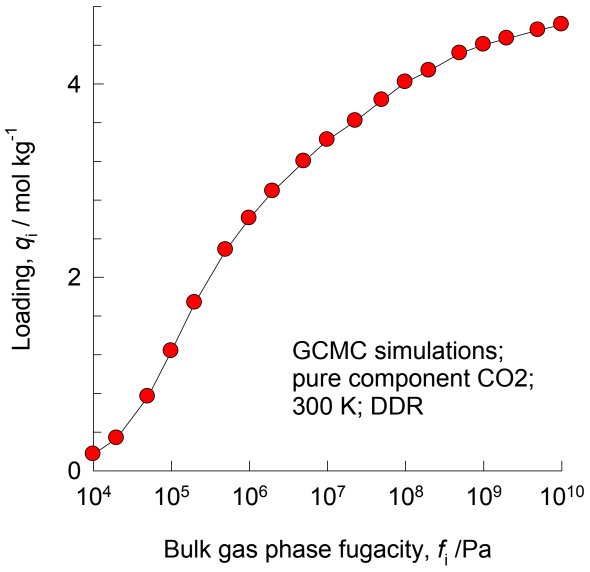
Loading, q_i / mol kg^{-1}
0
2
4
10^4
10^5
10^6
10^7
10^8
10^9
10^{10}
Bulk gas phase fugacity, f_i /Pa
GCMC simulations;
pure component CO2;
300 K; DDR

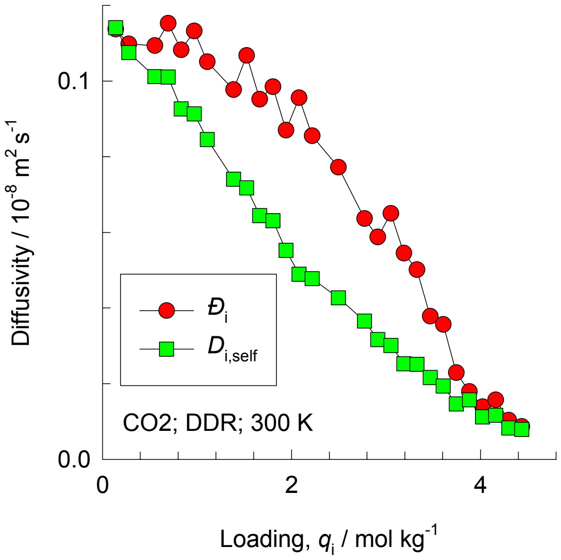
Diffusivity / 10^{-8} m^2 s^{-1}
0.0
0.1
0
2
4
Loading, q_i / mol kg^{-1}
$Đ_i$
$D_{i,self}$
CO2; DDR; 300 K

DDR, 300 K, N2

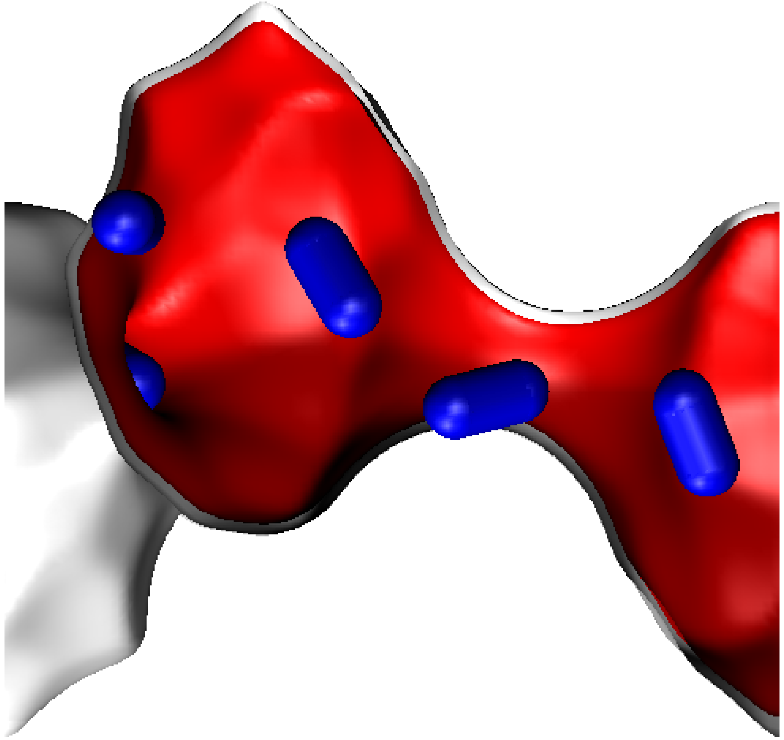

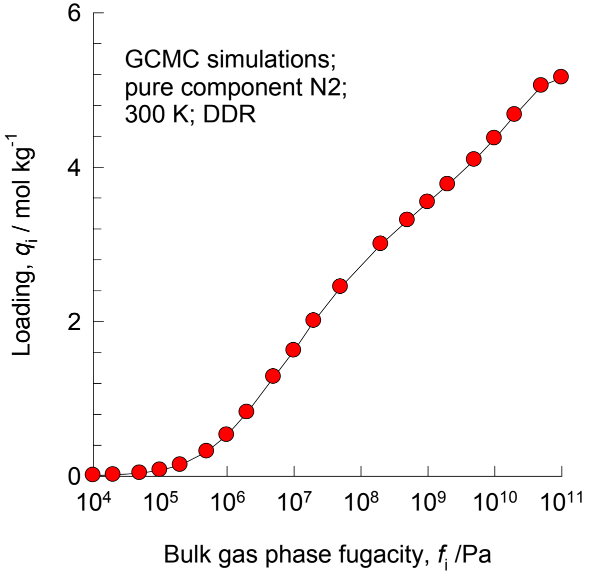

GCMC simulations;
pure component N2;
300 K; DDR
Loading, q_i / mol kg^{-1}
0
2
4
6
10^4
10^5
10^6
10^7
10^8
10^9
10^{10}
10^{11}
Bulk gas phase fugacity, f_i /Pa

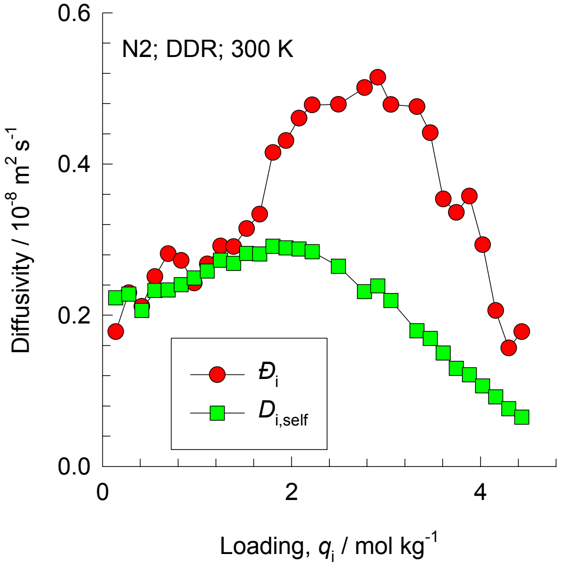

N2; DDR; 300 K
Diffusivity / 10^{-8} m^2 s^{-1}
0.0
0.2
0.4
0.6
0
2
4
$Đ_i$
$D_{i,self}$
Loading, q_i / mol kg^{-1}

DDR, 300 K, Ar

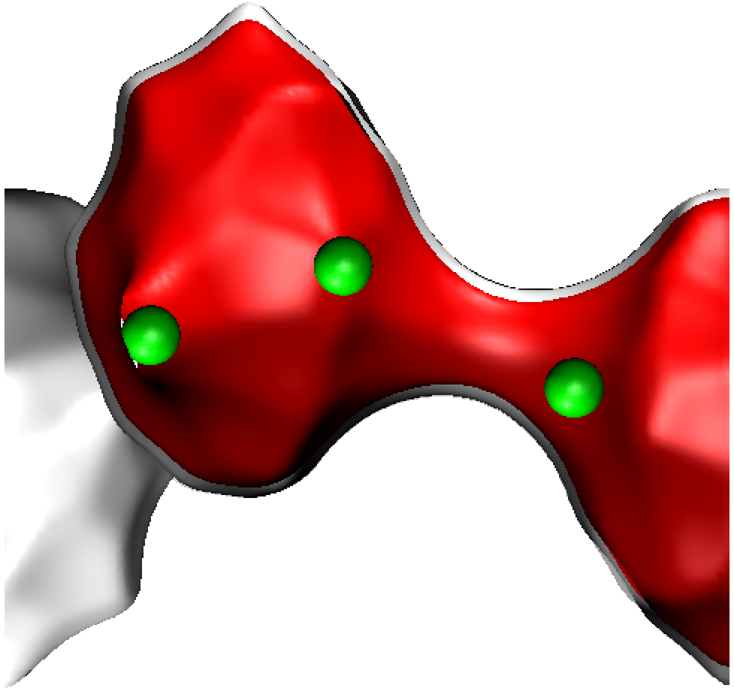

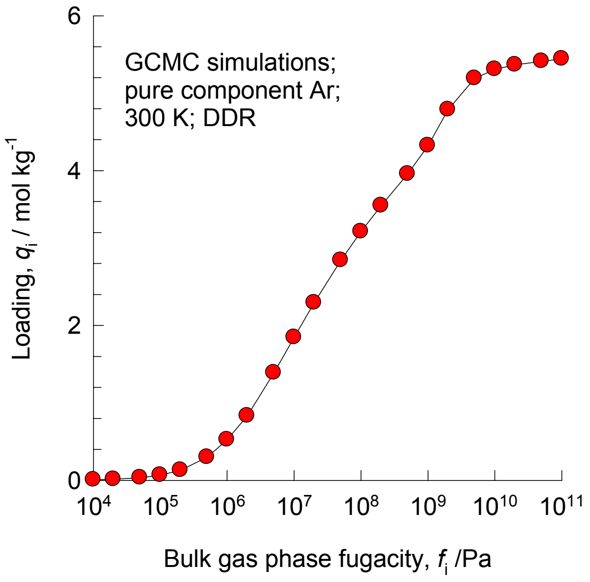
GCMC simulations;
pure component Ar;
300 K; DDR
Loading, q_i / mol kg^{-1}
Bulk gas phase fugacity, f_i /Pa
0
2
4
6
10^4
10^5
10^6
10^7
10^8
10^9
10^{10}
10^{11}

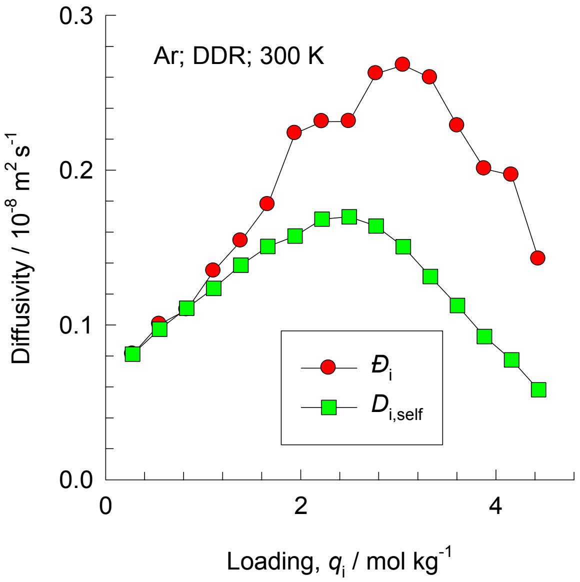
Ar; DDR; 300 K
Diffusivity / 10^{-8} m^2 s^{-1}
Loading, q_i / mol kg^{-1}
$Đ_i$
$D_{i,self}$
0.0
0.1
0.2
0.3
0
2
4

DDR, 300 K, Kr

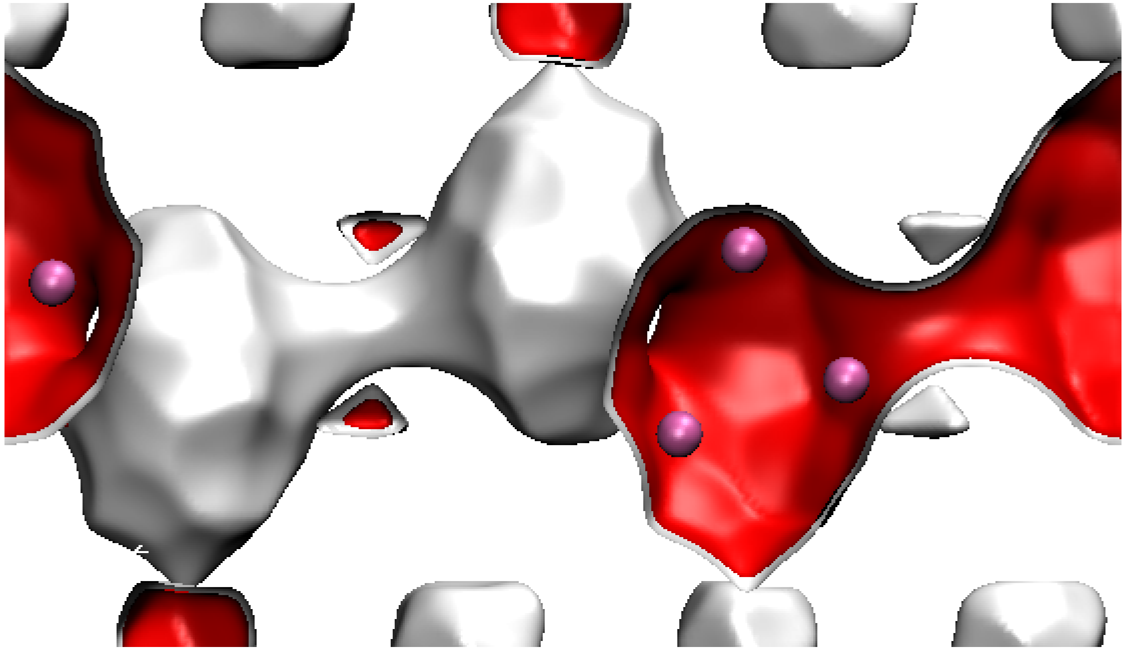

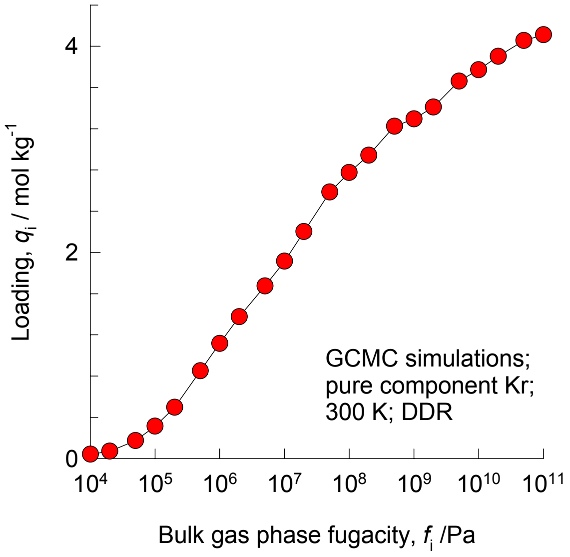

Loading, q_i / mol kg^{-1}
0
2
4
10^4
10^5
10^6
10^7
10^8
10^9
10^{10}
10^{11}
Bulk gas phase fugacity, f_i /Pa
GCMC simulations;
pure component Kr;
300 K; DDR

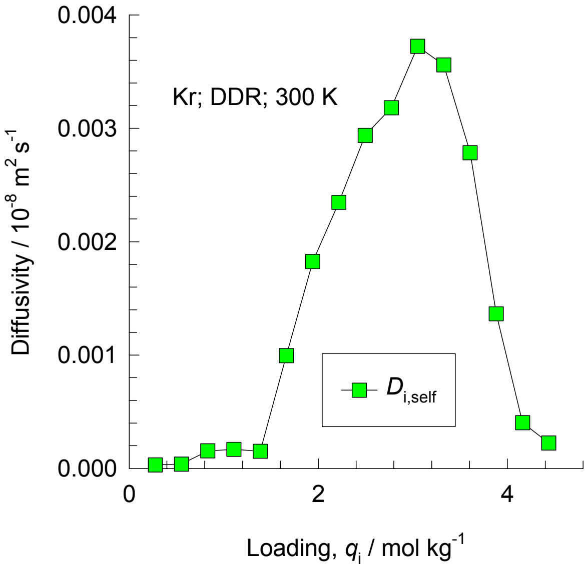

Diffusivity / 10^{-8} m^2 s^{-1}
0.000
0.001
0.002
0.003
0.004
0
2
4
Loading, q_i / mol kg^{-1}
Kr; DDR; 300 K
$D_{i,self}$

DDR, 300 K, Ne

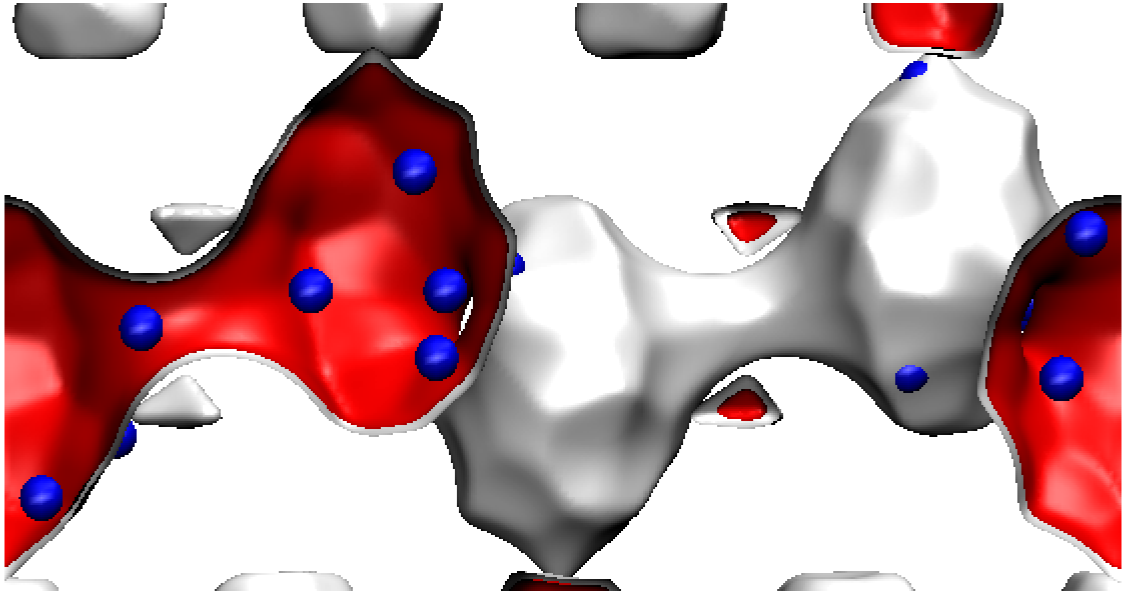

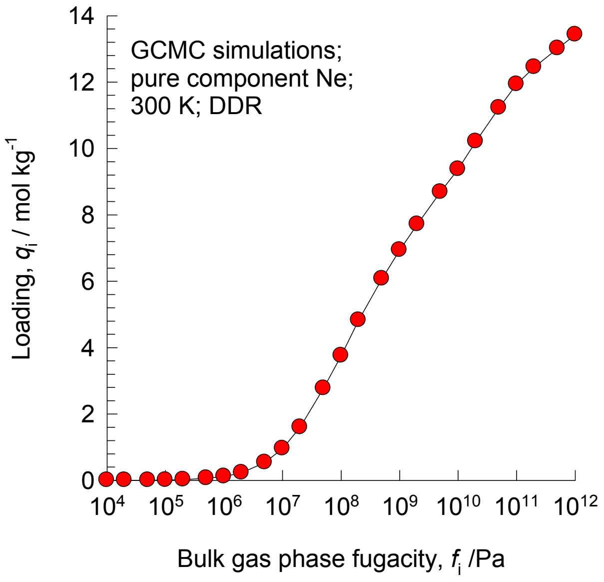
GCMC simulations;
pure component Ne;
300 K; DDR
Loading, q_i / mol kg^{-1}
Bulk gas phase fugacity, f_i /Pa
0
2
4
6
8
10
12
14
10^4
10^5
10^6
10^7
10^8
10^9
10^{10}
10^{11}
10^{12}

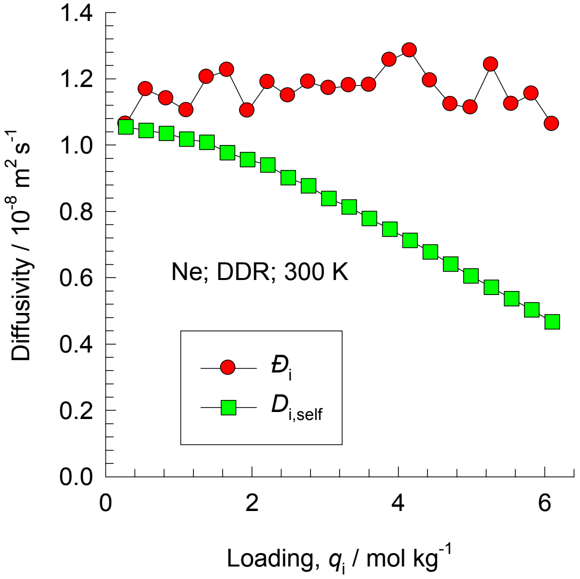
Ne; DDR; 300 K
Diffusivity / 10^{-8} m^2 s^{-1}
Loading, q_i / mol kg^{-1}
$Đ_i$
$D_{i,self}$
0.0
0.2
0.4
0.6
0.8
1.0
1.2
1.4
0
2
4
6

DDR, 300 K, He

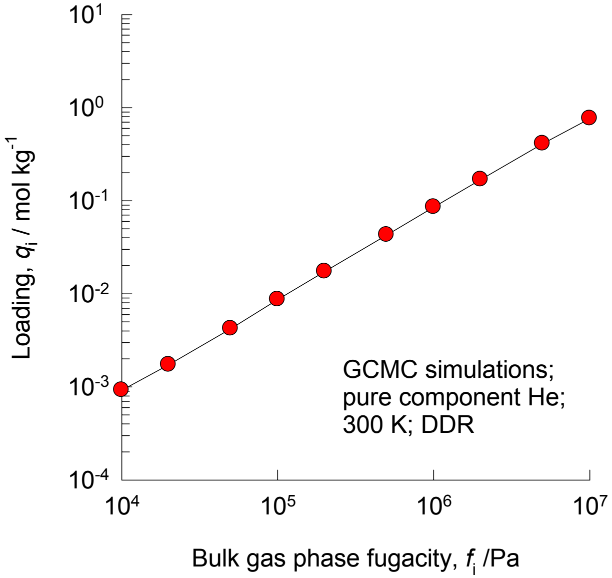
Loading, q_i / mol kg^{-1}
10^{1}
10^{0}
10^{-1}
10^{-2}
10^{-3}
10^{-4}
10^{4}
10^{5}
10^{6}
10^{7}
Bulk gas phase fugacity, f_i /Pa
GCMC simulations;
pure component He;
300 K; DDR

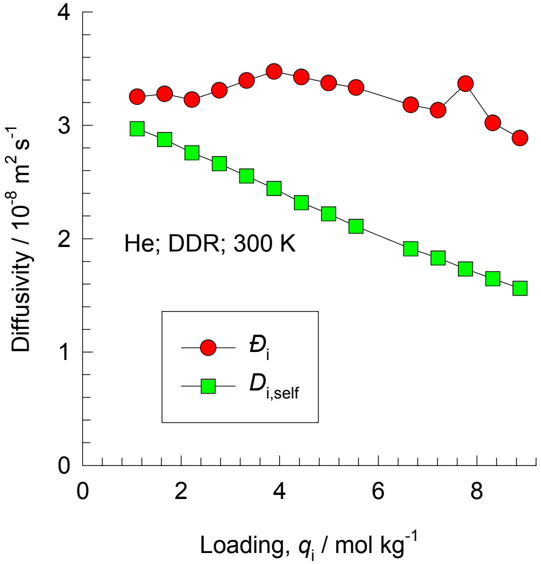
Diffusivity / 10^{-8} m^2 s^{-1}
4
3
2
1
0
0
2
4
6
8
Loading, q_i / mol kg^{-1}
He; DDR; 300 K
$Đ_i$
$D_{i,self}$

DDR, 300 K, H2

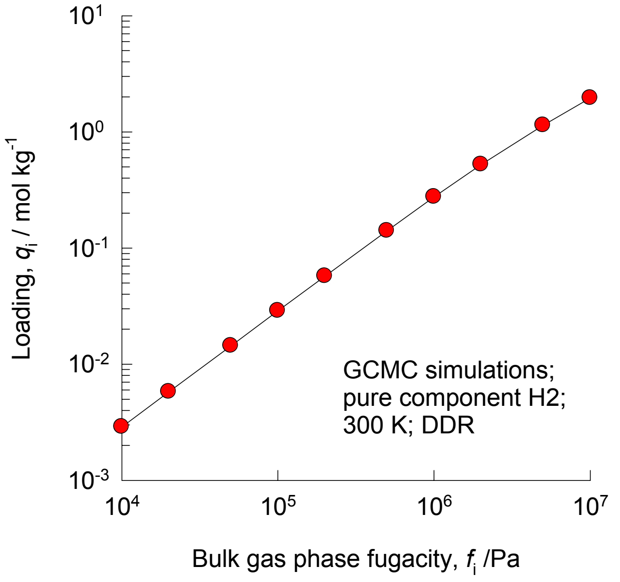
GCMC simulations;
pure component H2;
300 K; DDR
Loading, q_i / mol kg^{-1}
Bulk gas phase fugacity, f_i /Pa
10^{1}
10^{0}
10^{-1}
10^{-2}
10^{-3}
10^{4}
10^{5}
10^{6}
10^{7}

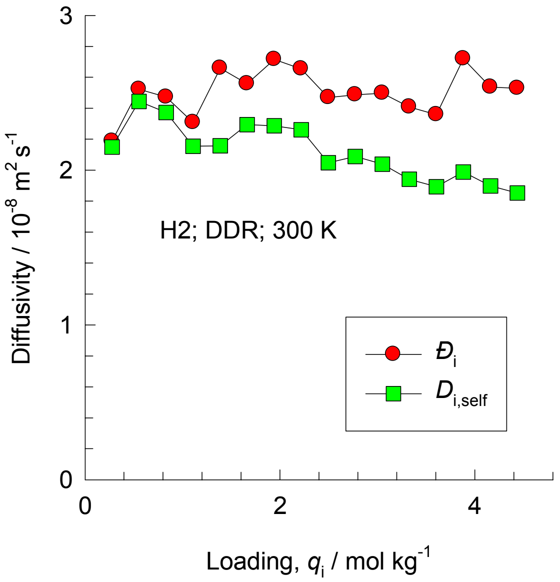
H2; DDR; 300 K
Diffusivity / 10^{-8} m^2 s^{-1}
Loading, q_i / mol kg^{-1}
$Đ_i$
$D_{i,self}$
0
1
2
3
0
2
4

LTA, 300 K, CH4

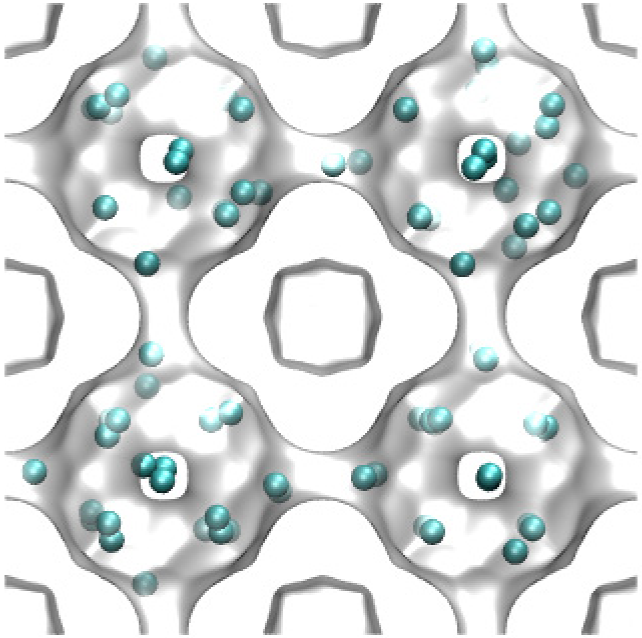

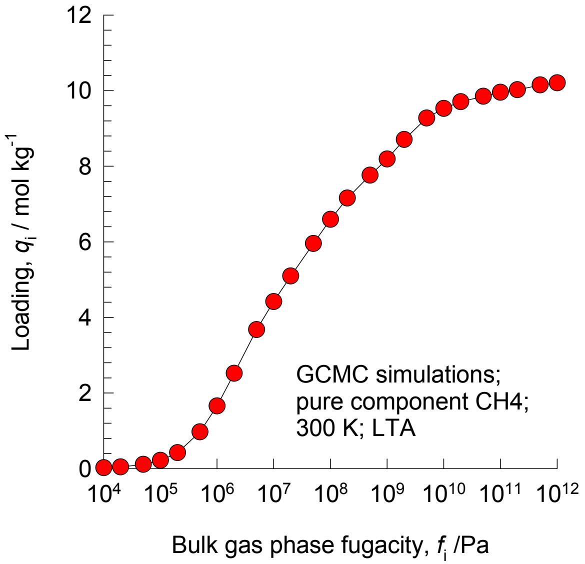

12
10
8
6
4
2
0
Loading, q_i / mol kg^{-1}
10^4
10^5
10^6
10^7
10^8
10^9
10^{10}
10^{11}
10^{12}
Bulk gas phase fugacity, f_i /Pa
GCMC simulations;
pure component CH4;
300 K; LTA

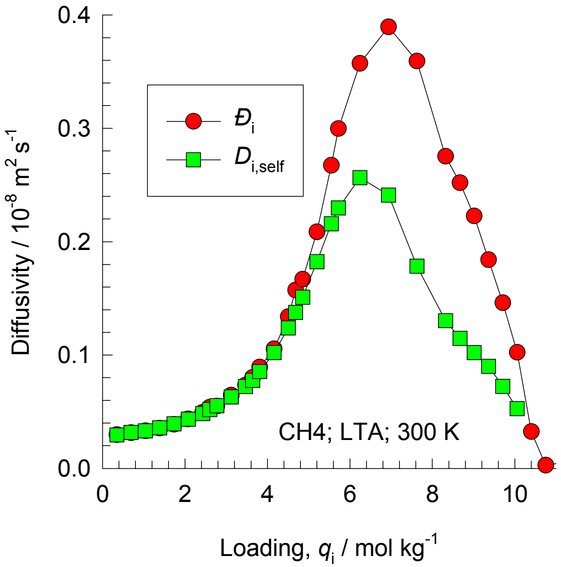

0.4
0.3
0.2
0.1
0.0
Diffusivity / 10^{-8} m^2 s^{-1}
0
2
4
6
8
10
Loading, q_i / mol kg^{-1}
$Đ_i$
$D_{i,self}$
CH4; LTA; 300 K

LTA, 300 K, CO2

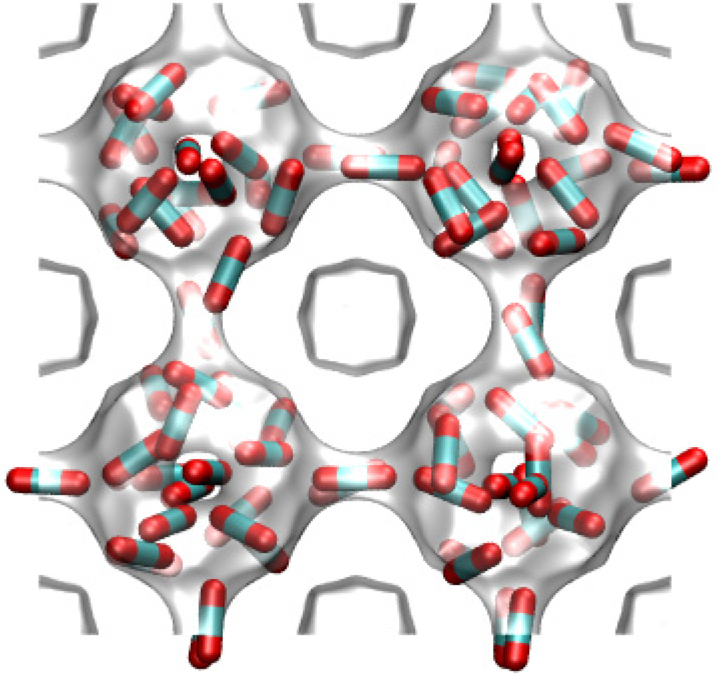

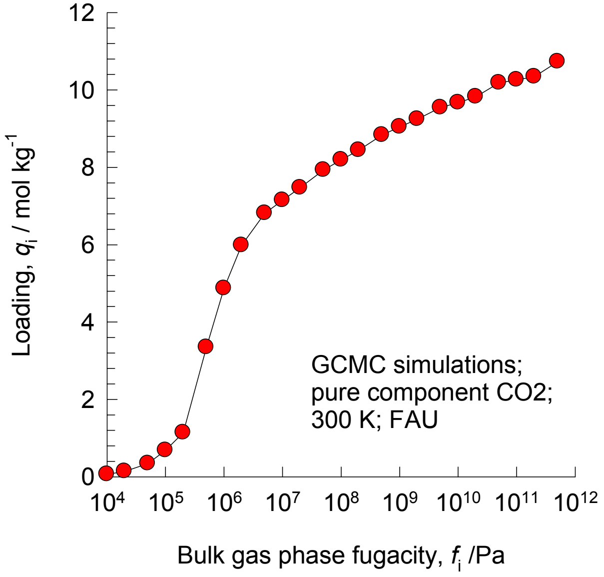
12
10
8
6
4
2
0
Loading, q_i / mol kg^{-1}
10^4
10^5
10^6
10^7
10^8
10^9
10^{10}
10^{11}
10^{12}
Bulk gas phase fugacity, f_i /Pa
GCMC simulations;
pure component CO2;
300 K; FAU

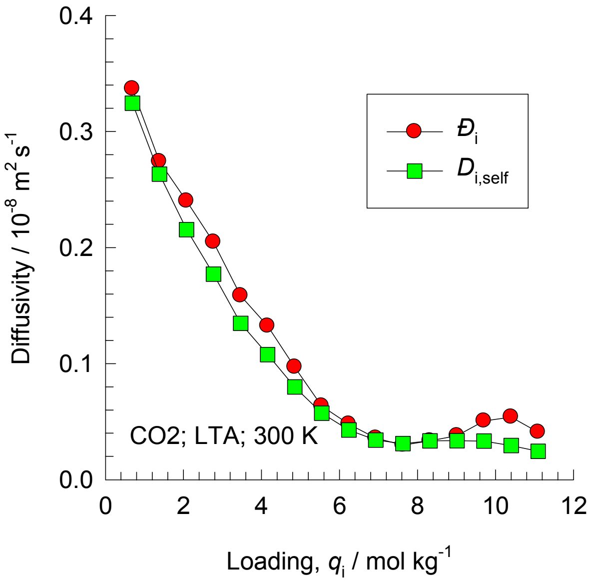
0.4
0.3
0.2
0.1
0.0
Diffusivity / 10^{-8} m^2 s^{-1}
0
2
4
6
8
10
12
Loading, q_i / mol kg^{-1}
$Đ_i$
$D_{i,self}$
CO2; LTA; 300 K

LTA, 300 K, N2

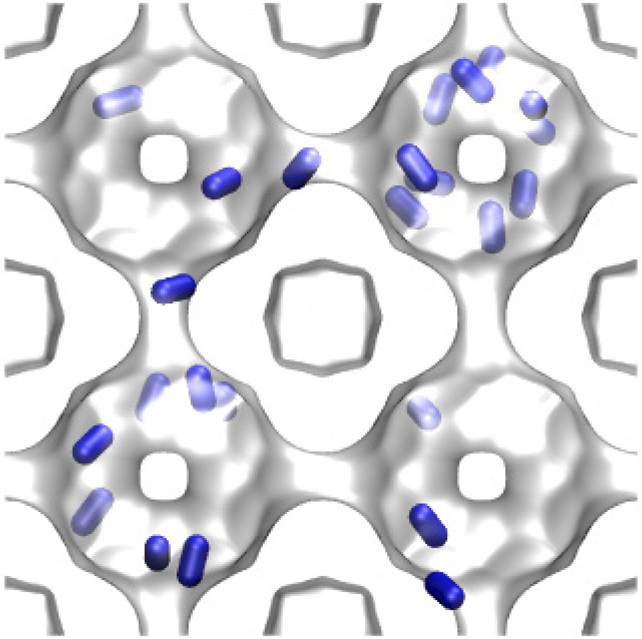

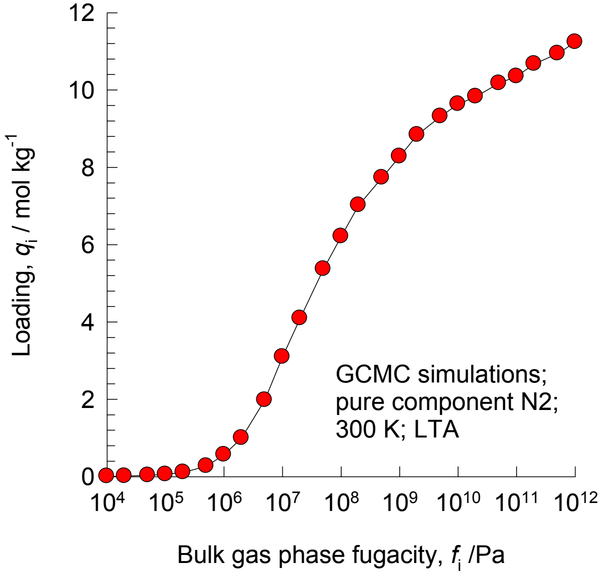
Loading, q_i / mol kg^{-1}
0
2
4
6
8
10
12
10^4
10^5
10^6
10^7
10^8
10^9
10^{10}
10^{11}
10^{12}
Bulk gas phase fugacity, f_i /Pa
GCMC simulations;
pure component N2;
300 K; LTA

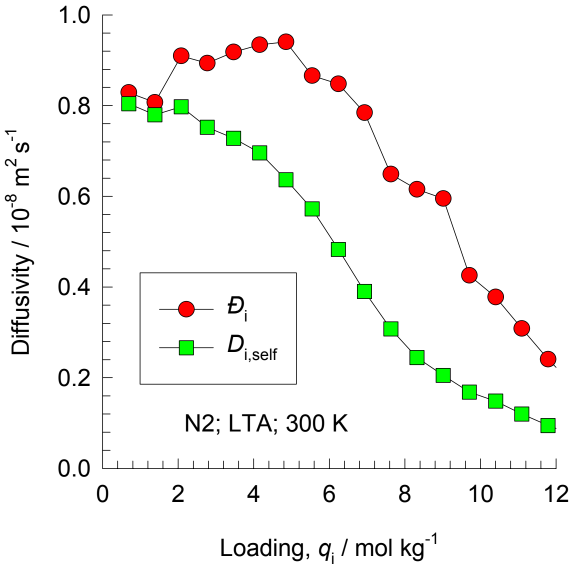
Diffusivity / 10^{-8} m^2 s^{-1}
0.0
0.2
0.4
0.6
0.8
1.0
0
2
4
6
8
10
12
Loading, q_i / mol kg^{-1}
$Đ_i$
$D_{i,self}$
N2; LTA; 300 K

LTA, 300 K, Ar

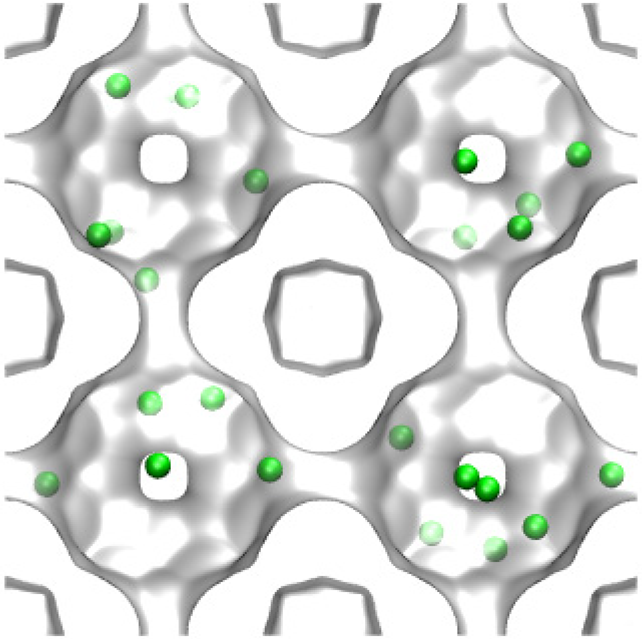

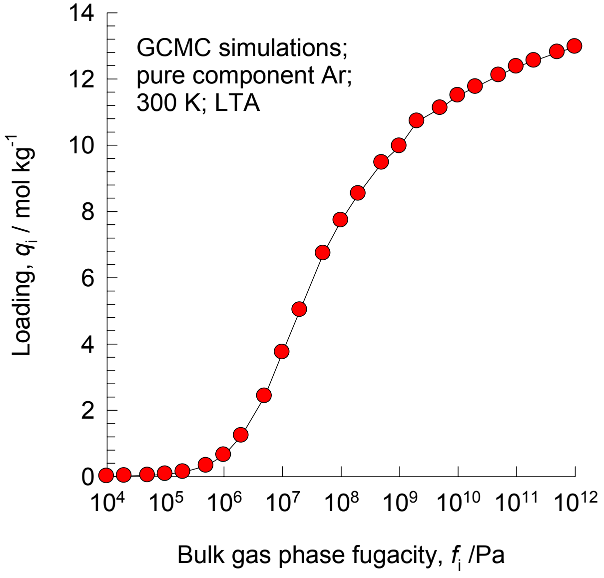
GCMC simulations;
pure component Ar;
300 K; LTA
Loading, q_i / mol kg^{-1}
0
2
4
6
8
10
12
14
10^4
10^5
10^6
10^7
10^8
10^9
10^{10}
10^{11}
10^{12}
Bulk gas phase fugacity, f_i /Pa

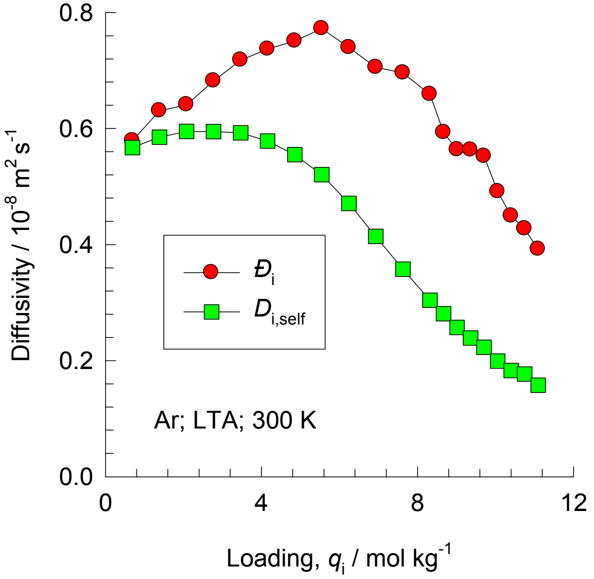
Diffusivity / 10^{-8} m^2 s^{-1}
0.0
0.2
0.4
0.6
0.8
0
4
8
12
Loading, q_i / mol kg^{-1}
$Đ_i$
$D_{i,self}$
Ar; LTA; 300 K

LTA, 300 K, Kr

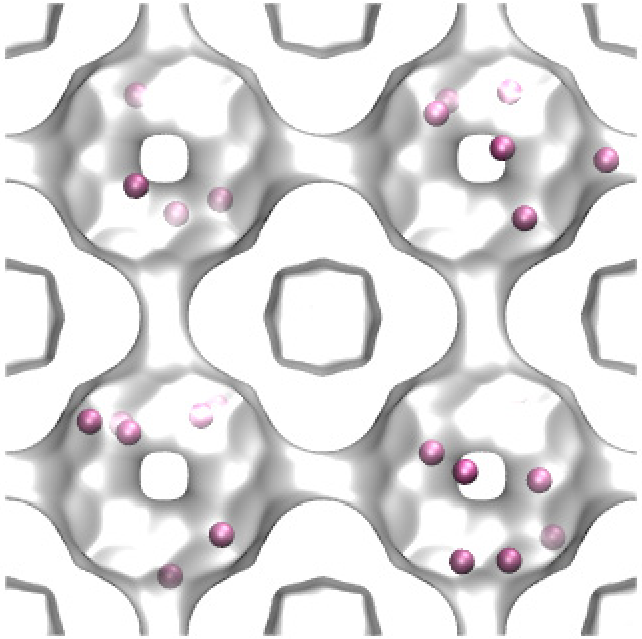

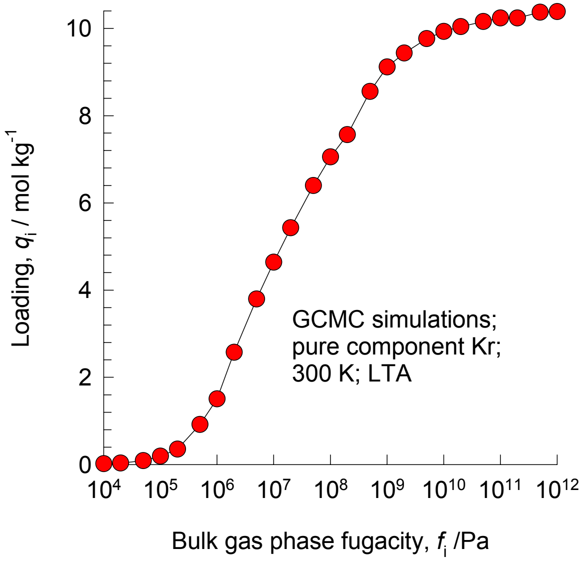

Loading, q_i / mol kg^{-1}
0
2
4
6
8
10
10^4
10^5
10^6
10^7
10^8
10^9
10^{10}
10^{11}
10^{12}
Bulk gas phase fugacity, f_i /Pa
GCMC simulations;
pure component Kr;
300 K; LTA

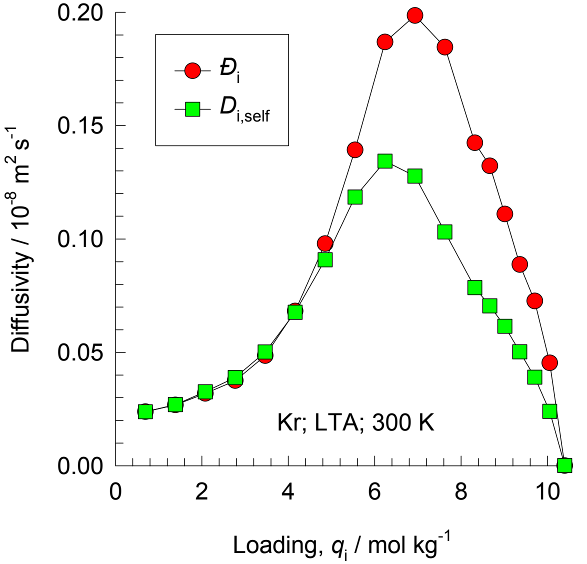

Diffusivity / 10^{-8} m^2 s^{-1}
0.00
0.05
0.10
0.15
0.20
$Đ_i$
$D_{i,self}$
Kr; LTA; 300 K
0
2
4
6
8
10
Loading, q_i / mol kg^{-1}

LTA, 300 K, Ne

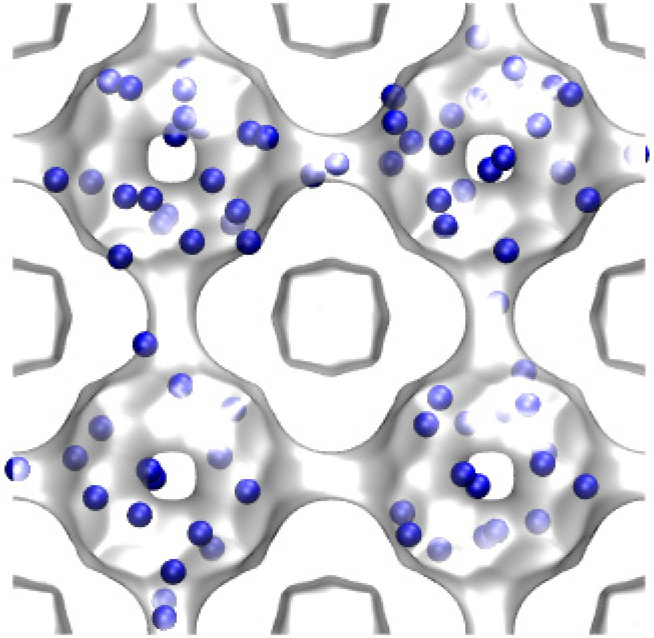

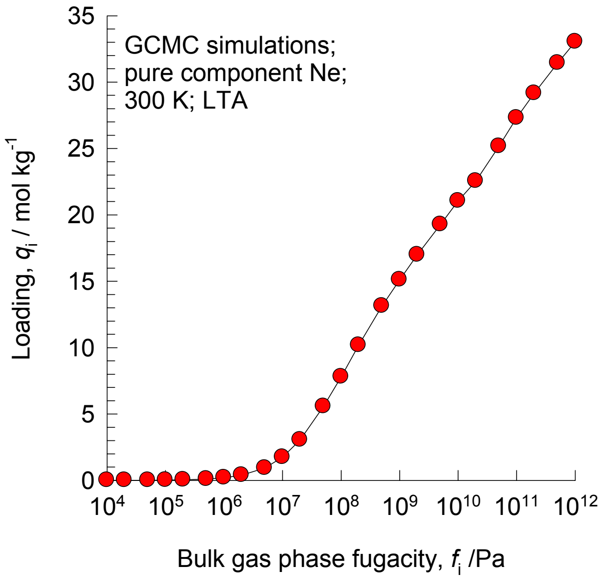
GCMC simulations;
pure component Ne;
300 K; LTA
Loading, q_i / mol kg^{-1}
0
5
10
15
20
25
30
35
10^4
10^5
10^6
10^7
10^8
10^9
10^{10}
10^{11}
10^{12}
Bulk gas phase fugacity, f_i /Pa

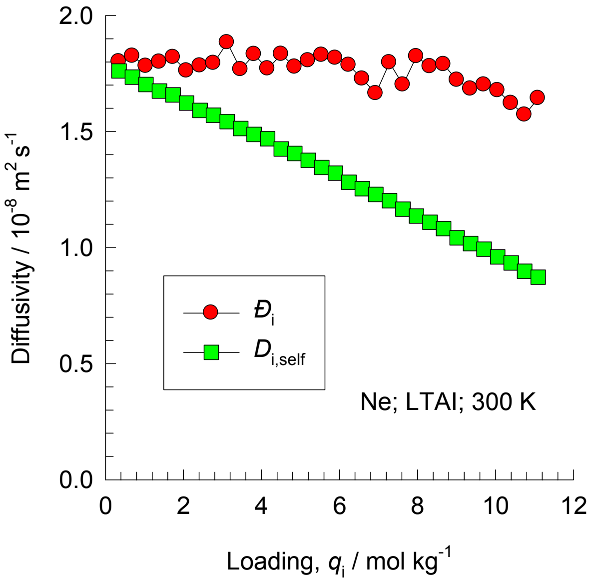
Diffusivity / 10^{-8} m^2 s^{-1}
0.0
0.5
1.0
1.5
2.0
$Đ_i$
$D_{i,self}$
Ne; LTAl; 300 K
0
2
4
6
8
10
12
Loading, q_i / mol kg^{-1}

FAU, 300 K, CH4

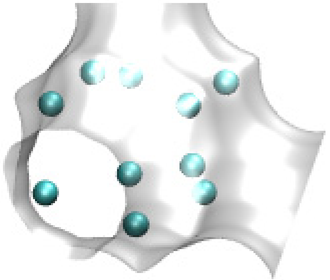

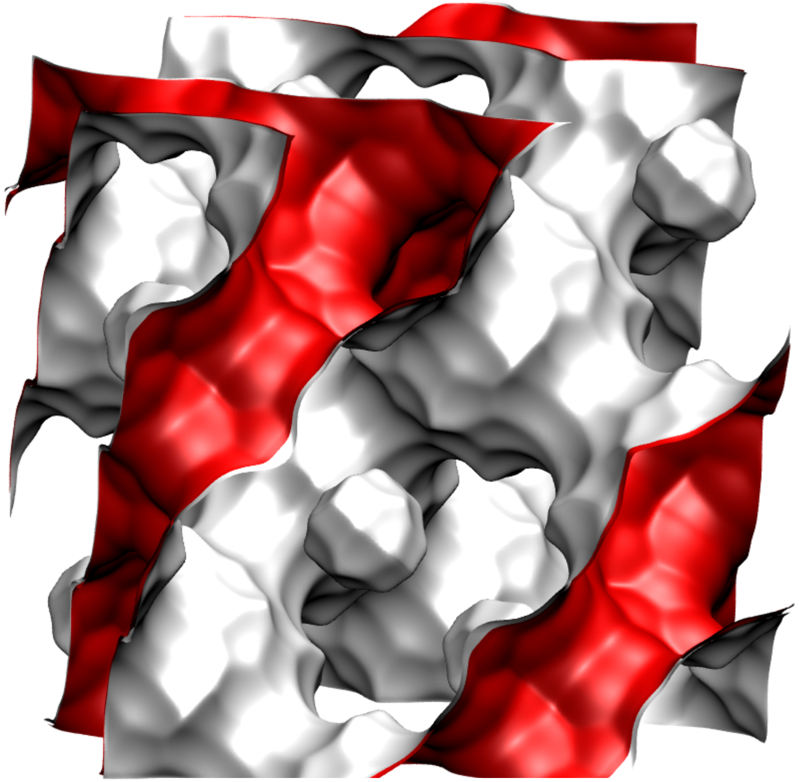

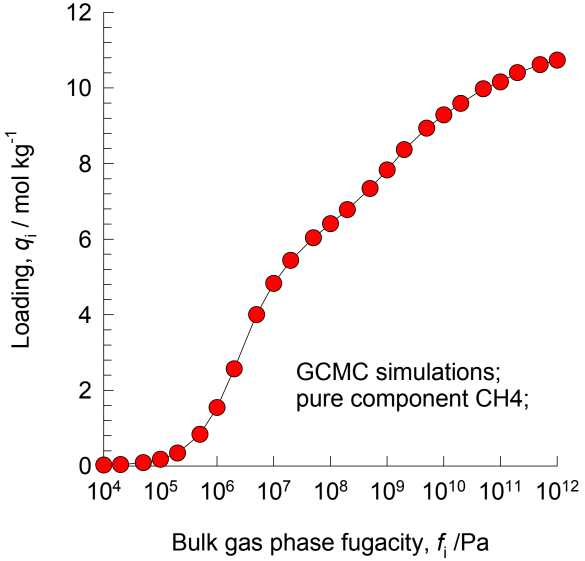
12
10
8
6
4
2
0
Loading, q_i / mol kg^{-1}
10^4
10^5
10^6
10^7
10^8
10^9
10^{10}
10^{11}
10^{12}
Bulk gas phase fugacity, f_i /Pa
GCMC simulations;
pure component CH4;

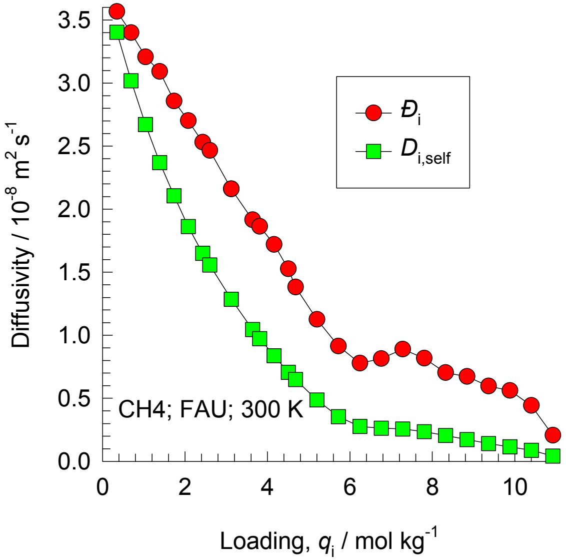
3.5
3.0
2.5
2.0
1.5
1.0
0.5
0.0
Diffusivity / 10^{-8} m^2 s^{-1}
0
2
4
6
8
10
Loading, q_i / mol kg^{-1}
$Đ_i$
$D_{i,self}$
CH4; FAU; 300 K

FAU, 300 K, CO2

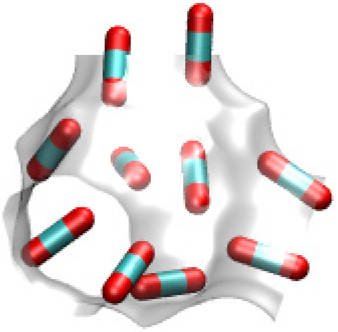

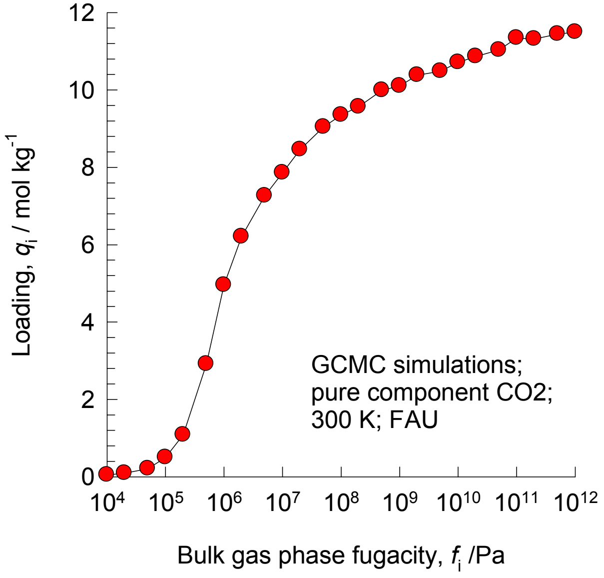
12
10
8
6
4
2
0
Loading, q_i / mol kg^{-1}
10^4 10^5 10^6 10^7 10^8 10^9 10^{10} 10^{11} 10^{12}
Bulk gas phase fugacity, f_i /Pa
GCMC simulations;
pure component CO2;
300 K; FAU

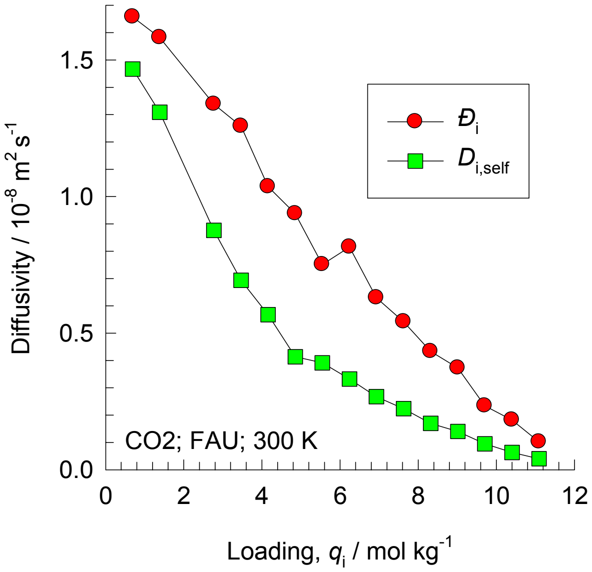
1.5
1.0
0.5
0.0
Diffusivity / 10^{-8} m^2 s^{-1}
0 2 4 6 8 10 12
Loading, q_i / mol kg^{-1}
$Đ_i$
$D_{i,self}$
CO2; FAU; 300 K

FAU, 300 K, N2

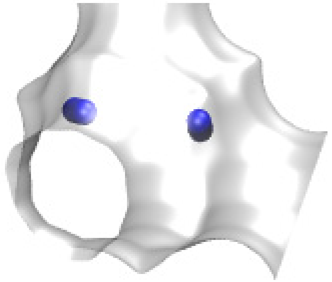

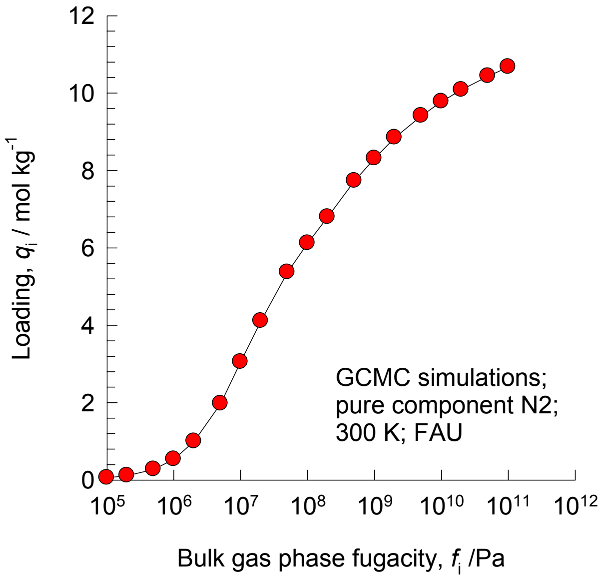
12
10
8
6
4
2
0
Loading, q_i / mol kg^{-1}
10^5
10^6
10^7
10^8
10^9
10^{10}
10^{11}
10^{12}
Bulk gas phase fugacity, f_i /Pa
GCMC simulations;
pure component N2;
300 K; FAU

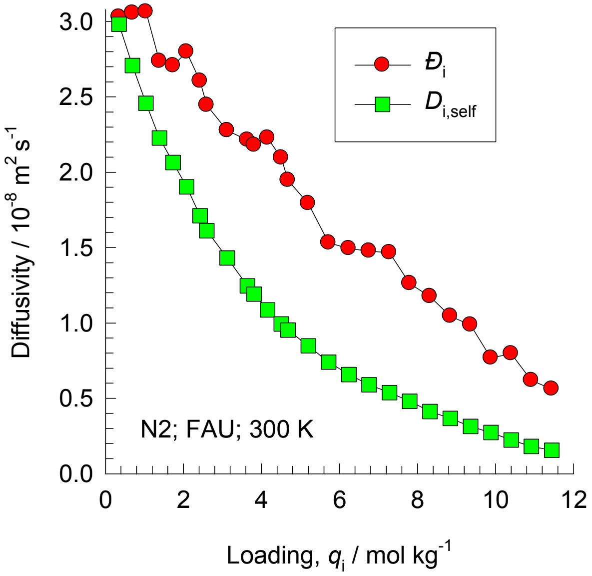
3.0
2.5
2.0
1.5
1.0
0.5
0.0
Diffusivity / 10^{-8} m^2 s^{-1}
0
2
4
6
8
10
12
Loading, q_i / mol kg^{-1}
$Đ_i$
$D_{i,self}$
N2; FAU; 300 K

FAU, 300 K, Ar

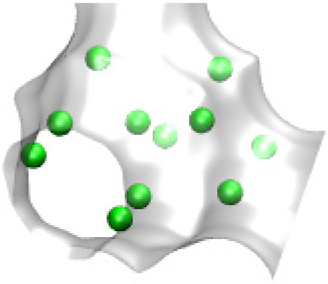

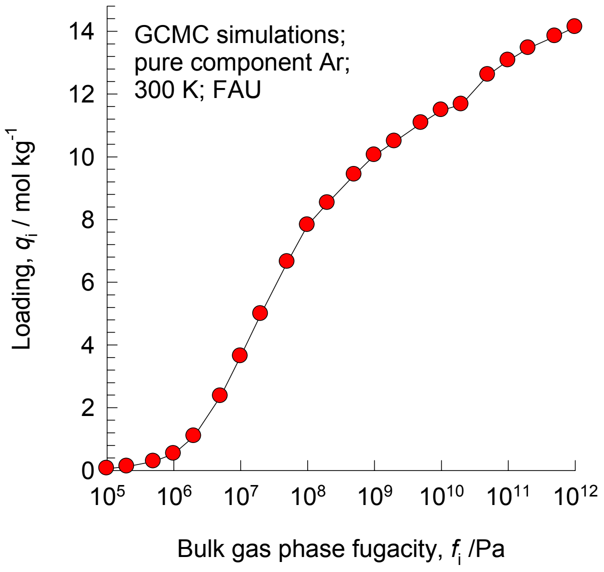
GCMC simulations;
pure component Ar;
300 K; FAU
Loading, q_i / mol kg^{-1}
0
2
4
6
8
10
12
14
10^5
10^6
10^7
10^8
10^9
10^{10}
10^{11}
10^{12}
Bulk gas phase fugacity, f_i /Pa

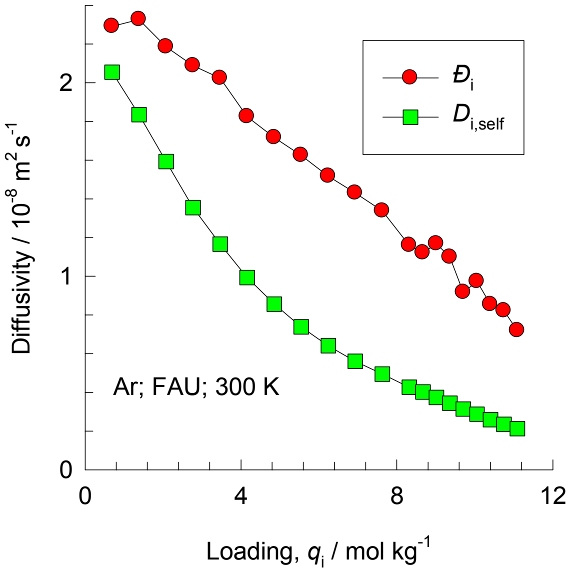
$Đ_i$
$D_{i,self}$
Ar; FAU; 300 K
Diffusivity / 10^{-8} m^2 s^{-1}
0
1
2
0
4
8
12
Loading, q_i / mol kg^{-1}

FAU, 300 K, Kr

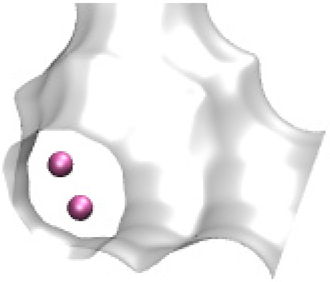

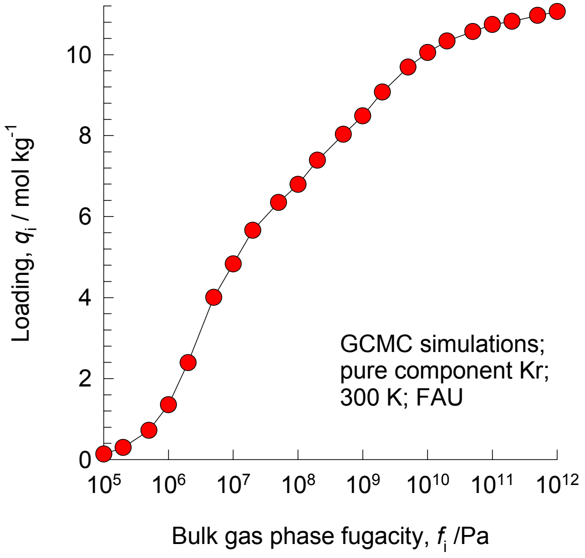

Loading, q_i / mol kg^{-1}
0
2
4
6
8
10
10^5
10^6
10^7
10^8
10^9
10^{10}
10^{11}
10^{12}
Bulk gas phase fugacity, f_i /Pa
GCMC simulations;
pure component Kr;
300 K; FAU

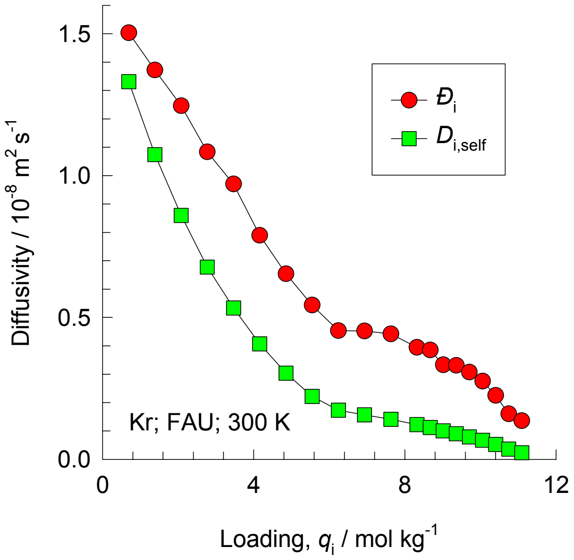

Diffusivity / 10^{-8} m^2 s^{-1}
0.0
0.5
1.0
1.5
0
4
8
12
Loading, q_i / mol kg^{-1}
$Đ_i$
$D_{i,self}$
Kr; FAU; 300 K

FAU, 300 K, Ne

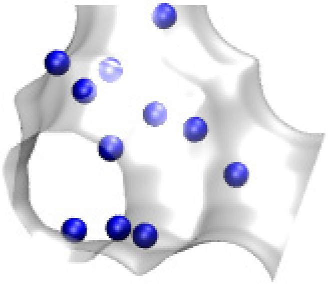

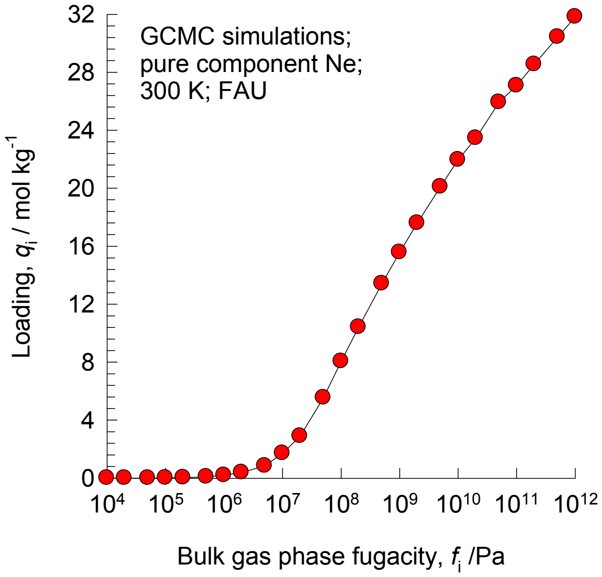
GCMC simulations;
pure component Ne;
300 K; FAU
Loading, q_i / mol kg^{-1}
0
4
8
12
16
20
24
28
32
10^4
10^5
10^6
10^7
10^8
10^9
10^{10}
10^{11}
10^{12}
Bulk gas phase fugacity, f_i /Pa

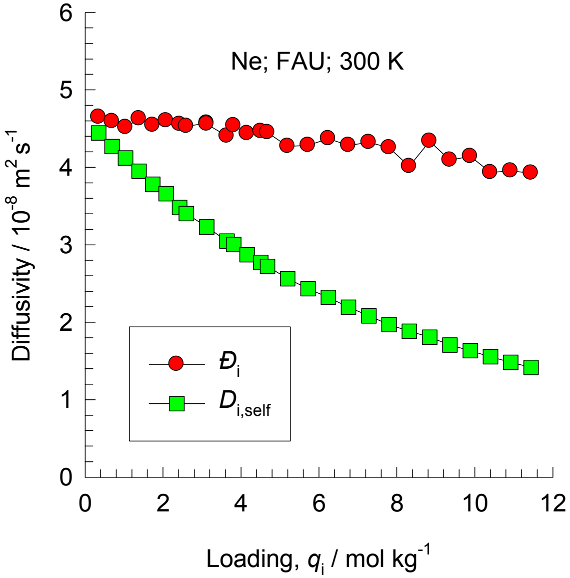
Ne; FAU; 300 K
Diffusivity / 10^{-8} m^2 s^{-1}
0
1
2
3
4
5
6
0
2
4
6
8
10
12
Loading, q_i / mol kg^{-1}
$Đ_i$
$D_{i,self}$

AFI, 300 K, CH4

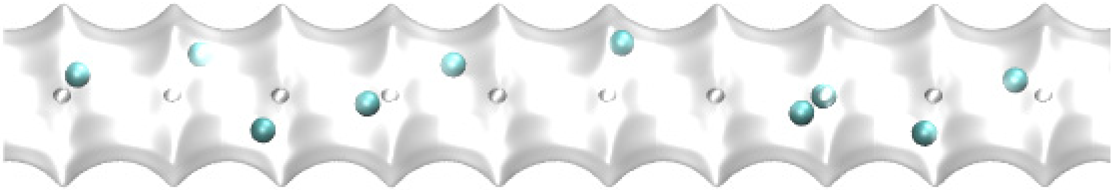

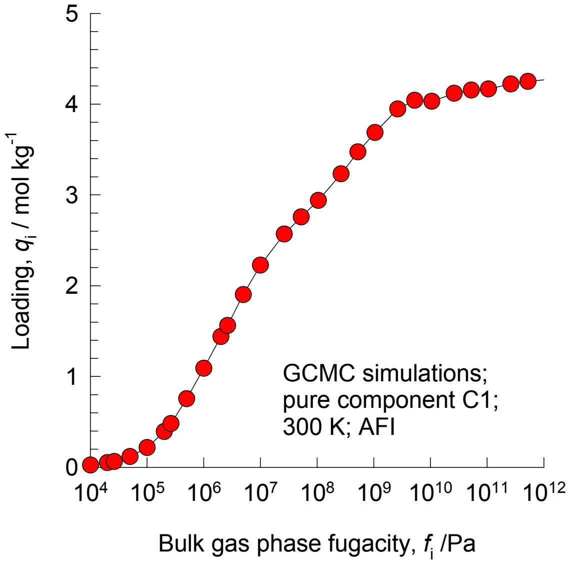

Loading, q_i / mol kg^{-1}
0
1
2
3
4
5
10^4
10^5
10^6
10^7
10^8
10^9
10^{10}
10^{11}
10^{12}
Bulk gas phase fugacity, f_i /Pa
GCMC simulations;
pure component C1;
300 K; AFI

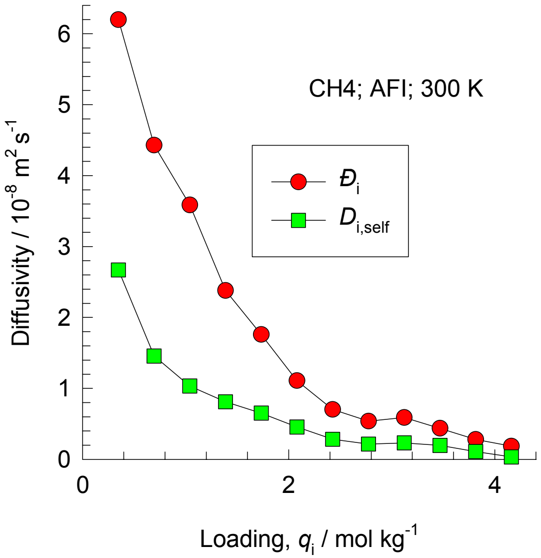

Diffusivity / 10^{-8} m^2 s^{-1}
0
1
2
3
4
5
6
0
2
4
Loading, q_i / mol kg^{-1}
CH4; AFI; 300 K
$Đ_i$
$D_{i,self}$

AFI, 300 K, CO2

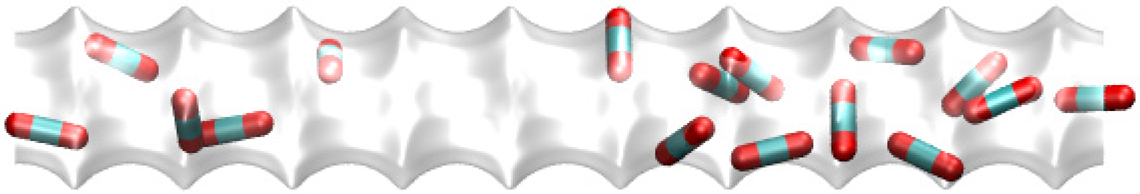

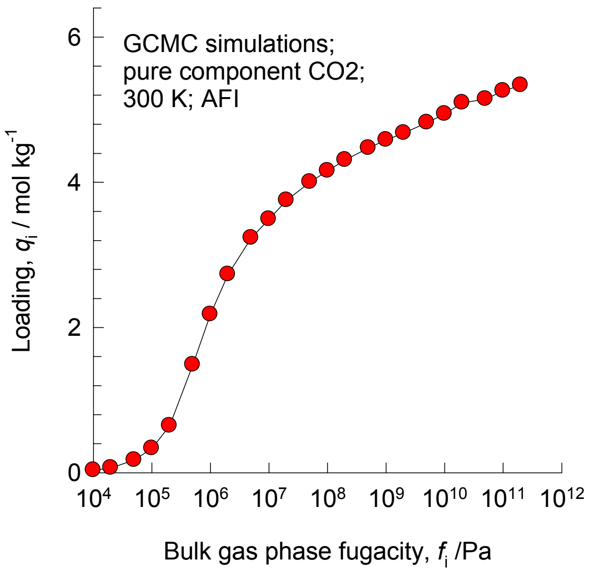
GCMC simulations;
pure component CO2;
300 K; AFI
Loading, q_i / mol kg^{-1}
0
2
4
6
10^4
10^5
10^6
10^7
10^8
10^9
10^{10}
10^{11}
10^{12}
Bulk gas phase fugacity, f_i /Pa

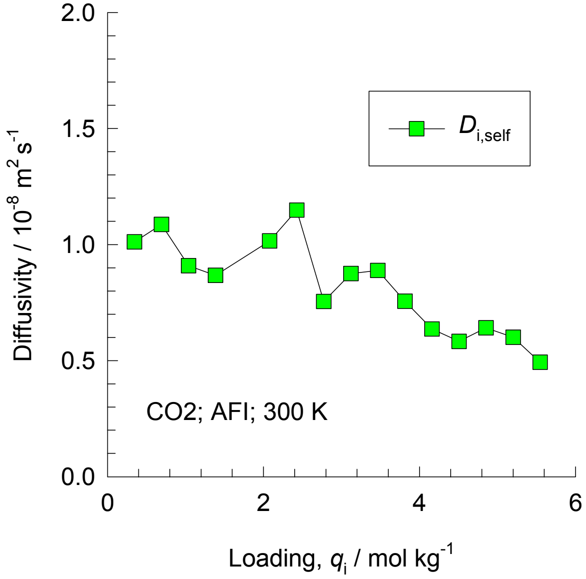
$D_{i,self}$
CO2; AFI; 300 K
Diffusivity / 10^{-8} m^2 s^{-1}
0.0
0.5
1.0
1.5
2.0
0
2
4
6
Loading, q_i / mol kg^{-1}

AFI, 300 K, N2

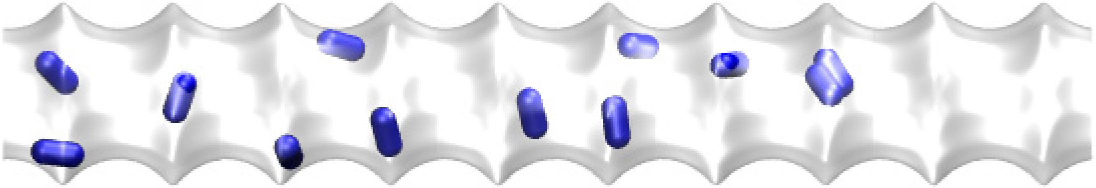

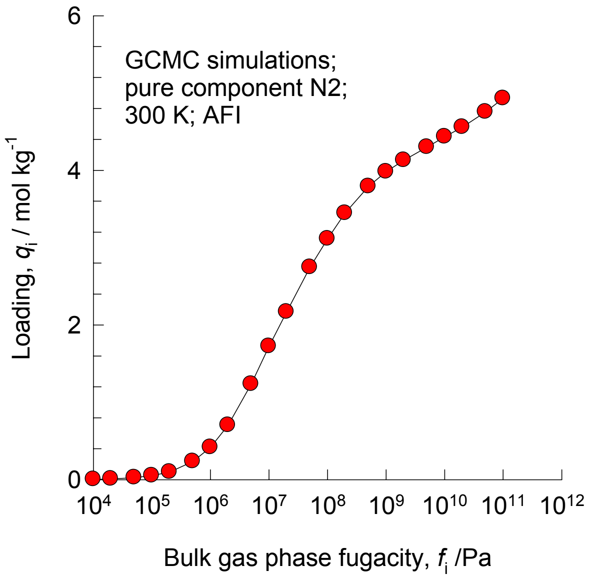
GCMC simulations;
pure component N2;
300 K; AFI
Loading, q_i / mol kg^{-1}
0
2
4
6
10^4
10^5
10^6
10^7
10^8
10^9
10^{10}
10^{11}
10^{12}
Bulk gas phase fugacity, f_i /Pa

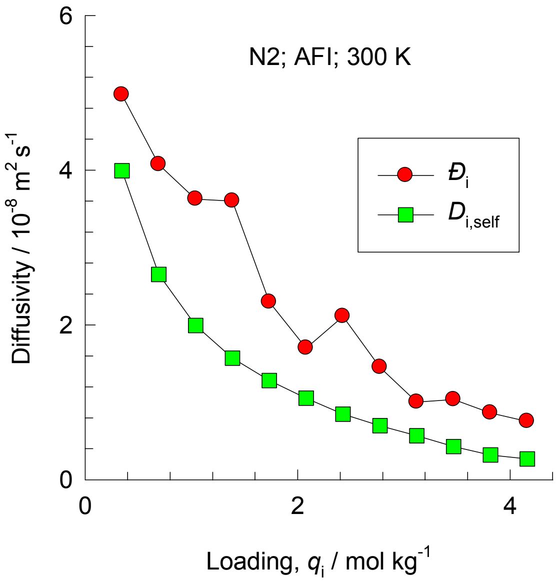
N2; AFI; 300 K
Diffusivity / 10^{-8} m^2 s^{-1}
0
2
4
6
Đ$_i$
$D_{i,self}$
0
2
4
Loading, q_i / mol kg^{-1}

AFI, 300 K, Ar

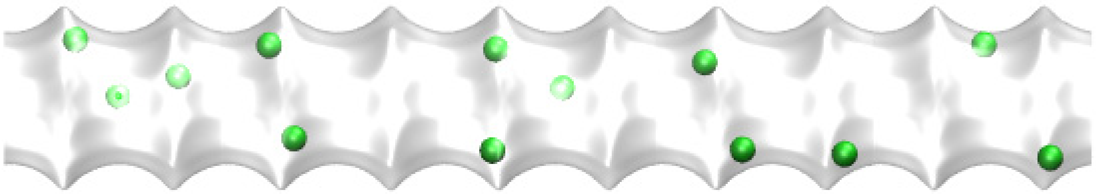

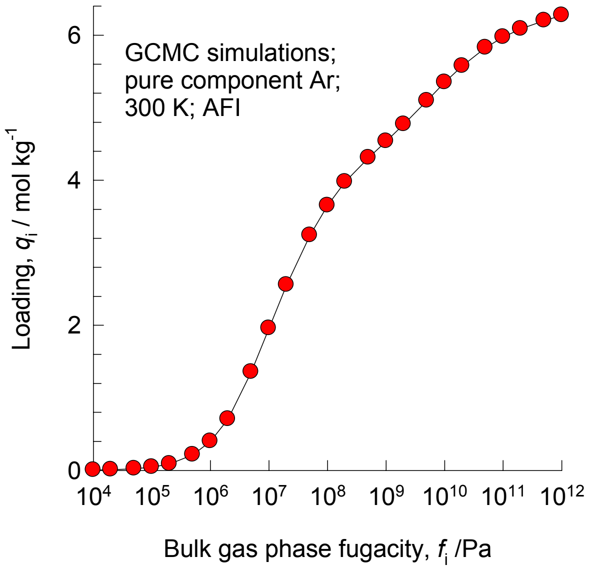
GCMC simulations;
pure component Ar;
300 K; AFI
Loading, q_i / mol kg^{-1}
0
2
4
6
10^4
10^5
10^6
10^7
10^8
10^9
10^{10}
10^{11}
10^{12}
Bulk gas phase fugacity, f_i /Pa

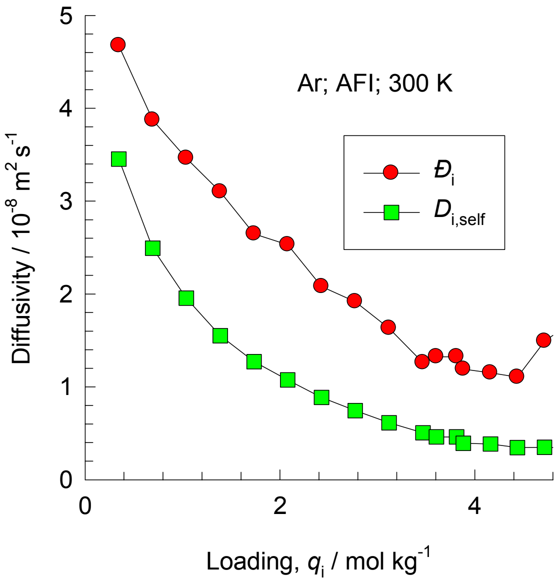
Ar; AFI; 300 K
$Đ_i$
$D_{i,self}$
Diffusivity / 10^{-8} m^2 s^{-1}
0
1
2
3
4
5
0
2
4
Loading, q_i / mol kg^{-1}

AFI, 300 K, Kr

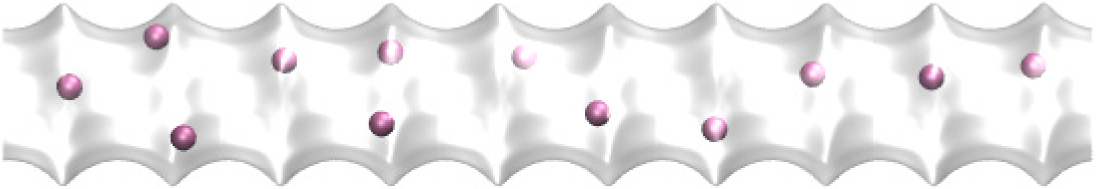

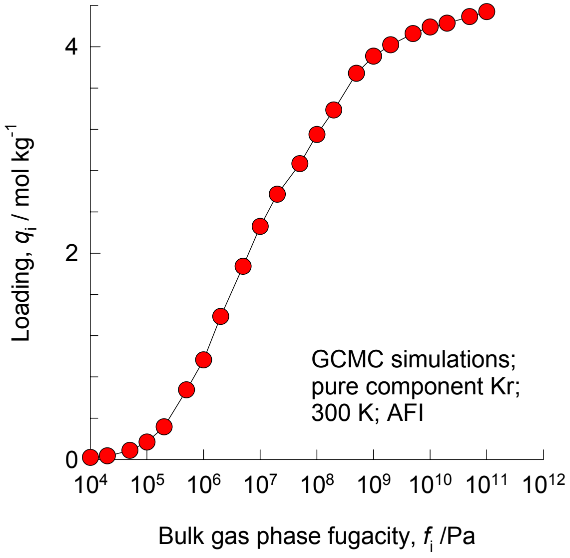

Loading, q_i / mol kg^{-1}
0
2
4
10^4
10^5
10^6
10^7
10^8
10^9
10^{10}
10^{11}
10^{12}
Bulk gas phase fugacity, f_i /Pa
GCMC simulations;
pure component Kr;
300 K; AFI

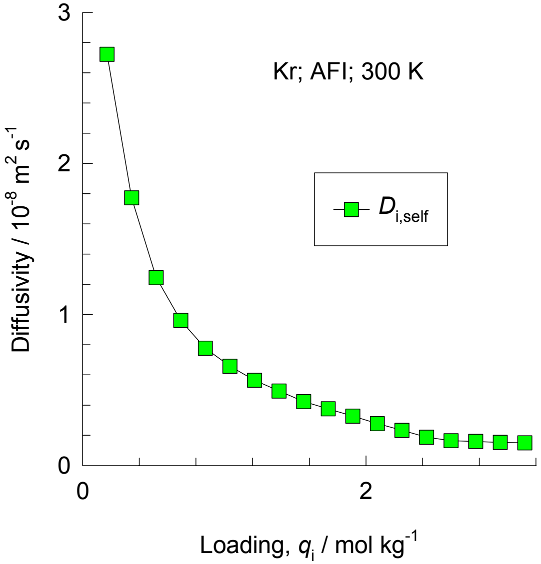

Diffusivity / 10^{-8} m^2 s^{-1}
0
1
2
3
0
2
Loading, q_i / mol kg^{-1}
Kr; AFI; 300 K
$D_{i,self}$

AFI, 300 K, Ne

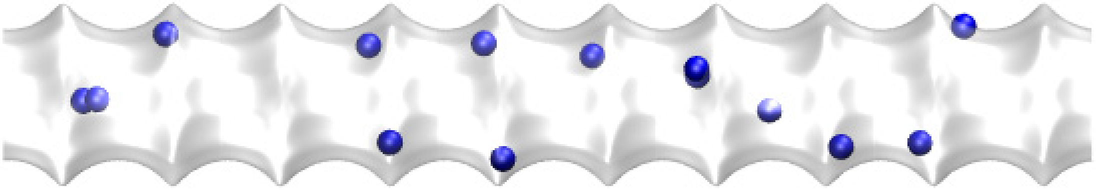

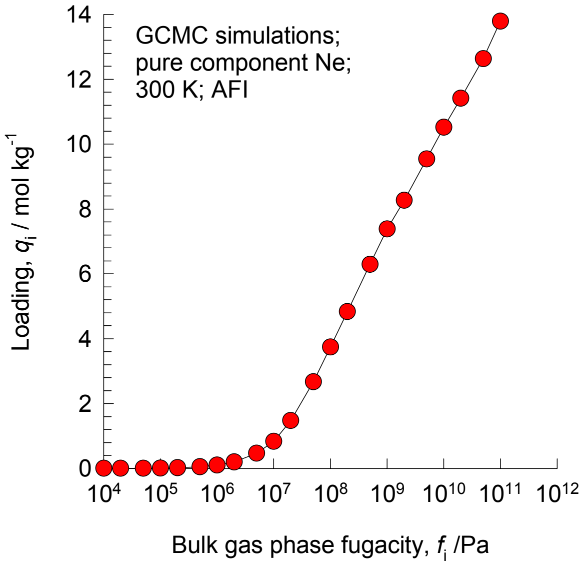

GCMC simulations;
pure component Ne;
300 K; AFI
Loading, q_i / mol kg^{-1}
0
2
4
6
8
10
12
14
10^4
10^5
10^6
10^7
10^8
10^9
10^{10}
10^{11}
10^{12}
Bulk gas phase fugacity, f_i /Pa

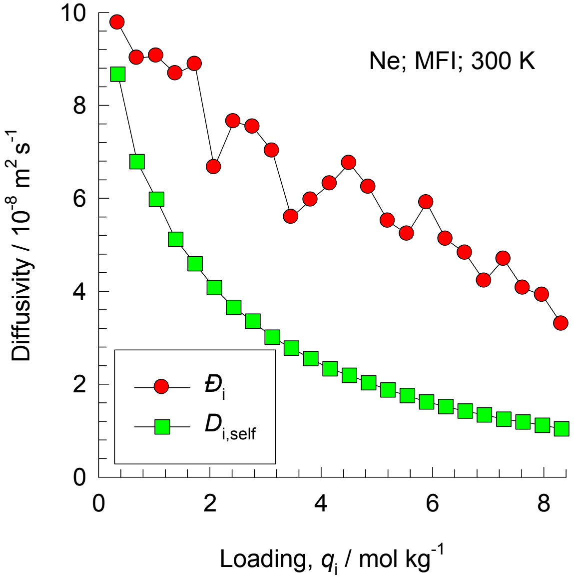

Ne; MFI; 300 K
Diffusivity / 10^{-8} m^2 s^{-1}
0
2
4
6
8
10
$Đ_i$
$D_{i,self}$
0
2
4
6
8
Loading, q_i / mol kg^{-1}

AFI, 300 K, He

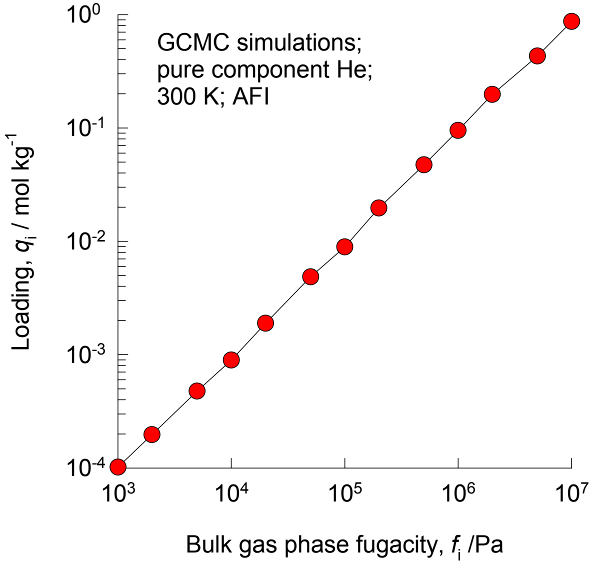
GCMC simulations;
pure component He;
300 K; AFI
Loading, q_i / mol kg^{-1}
10^0
10^{-1}
10^{-2}
10^{-3}
10^{-4}
10^3
10^4
10^5
10^6
10^7
Bulk gas phase fugacity, f_i /Pa

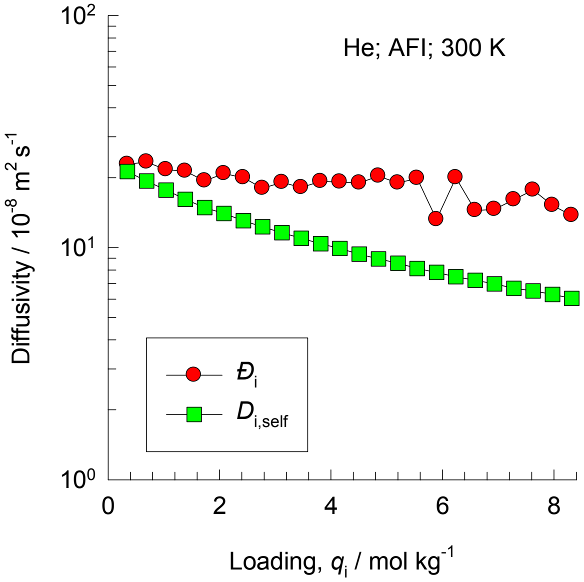
He; AFI; 300 K
Diffusivity / 10^{-8} m^2 s^{-1}
10^2
10^1
10^0
$Đ_i$
$D_{i,self}$
0
2
4
6
8
Loading, q_i / mol kg^{-1}

AFI, 300 K, H2

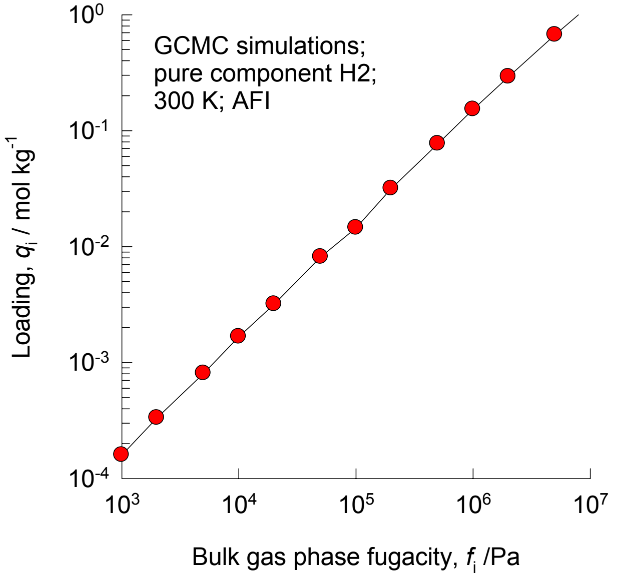
GCMC simulations;
pure component H2;
300 K; AFI
Loading, q_i / mol kg^{-1}
10^0
10^{-1}
10^{-2}
10^{-3}
10^{-4}
10^3
10^4
10^5
10^6
10^7
Bulk gas phase fugacity, f_i /Pa

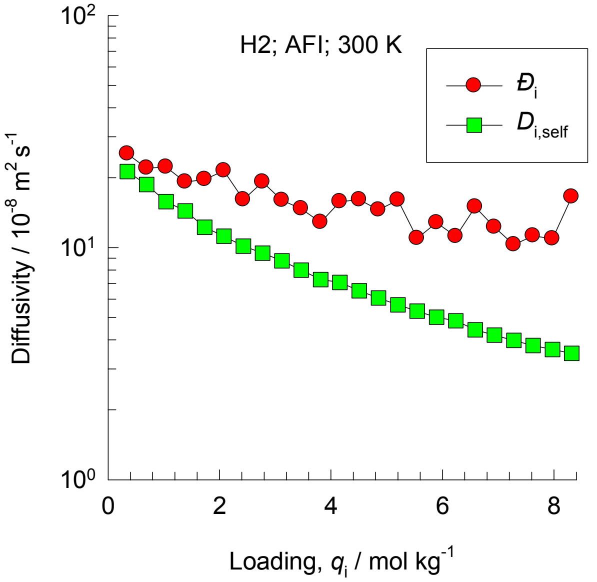
H2; AFI; 300 K
$Đ_i$
$D_{i,self}$
Diffusivity / 10^{-8} m^2 s^{-1}
10^2
10^1
10^0
0
2
4
6
8
Loading, q_i / mol kg^{-1}

MFI, 300 K, CH4

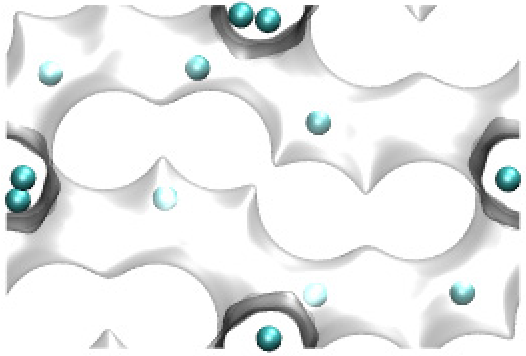

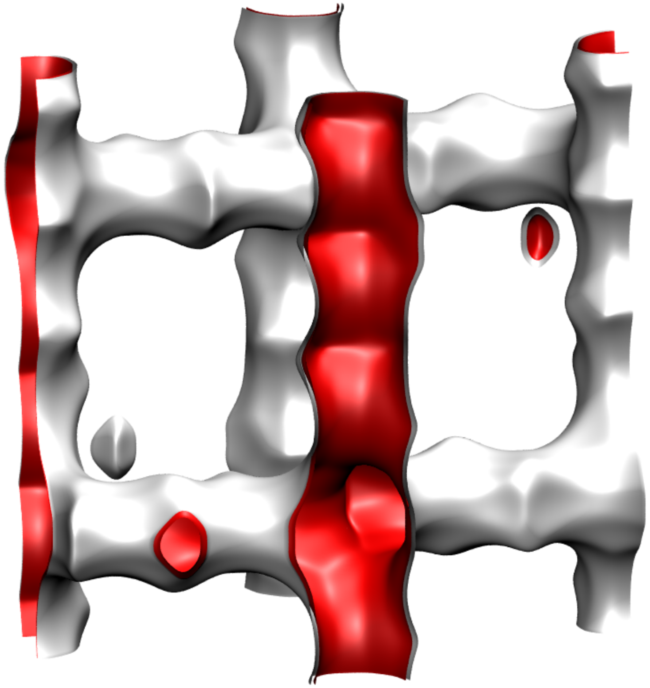

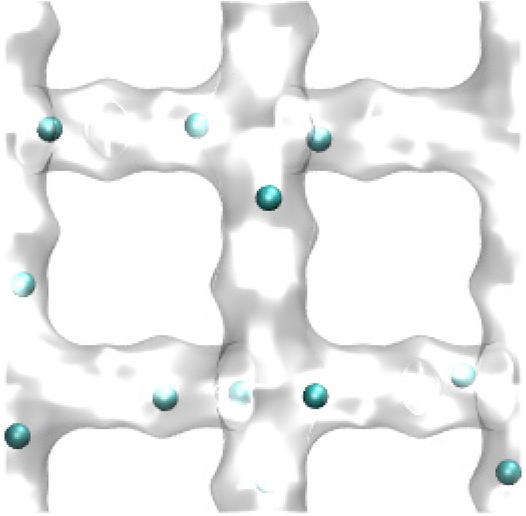

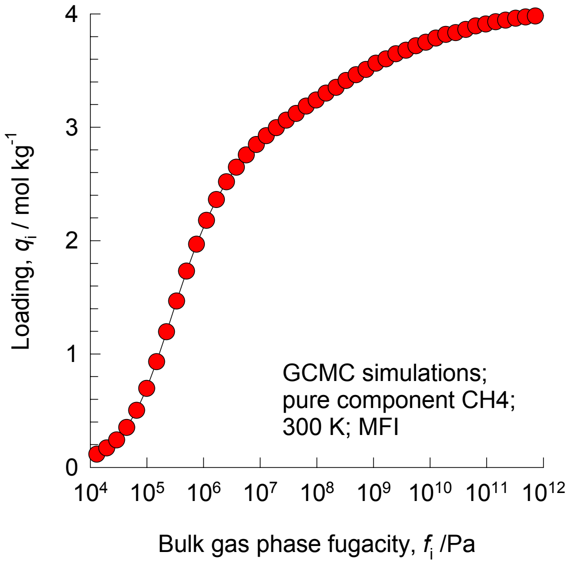
4
3
2
1
0
Loading, q_i / mol kg^{-1}
10^4
10^5
10^6
10^7
10^8
10^9
10^{10}
10^{11}
10^{12}
Bulk gas phase fugacity, f_i /Pa
GCMC simulations;
pure component CH4;
300 K; MFI

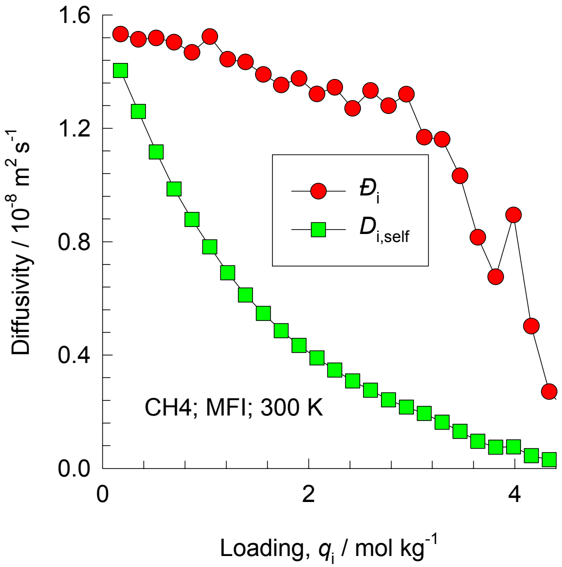
1.6
1.2
0.8
0.4
0.0
Diffusivity / 10^{-8} m^2 s^{-1}
0
2
4
Loading, q_i / mol kg^{-1}
$Đ_i$
$D_{i,self}$
CH4; MFI; 300 K

MFI, 300 K, CO2

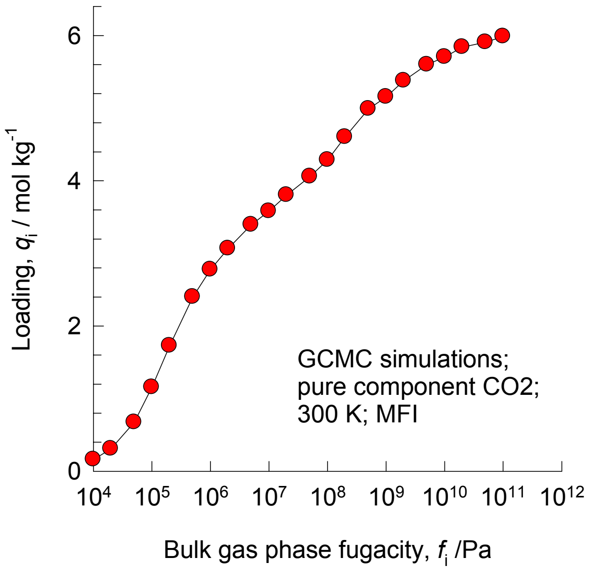

Loading, q_i / mol kg^{-1}
0
2
4
6
10^4
10^5
10^6
10^7
10^8
10^9
10^{10}
10^{11}
10^{12}
Bulk gas phase fugacity, f_i /Pa
GCMC simulations;
pure component CO2;
300 K; MFI

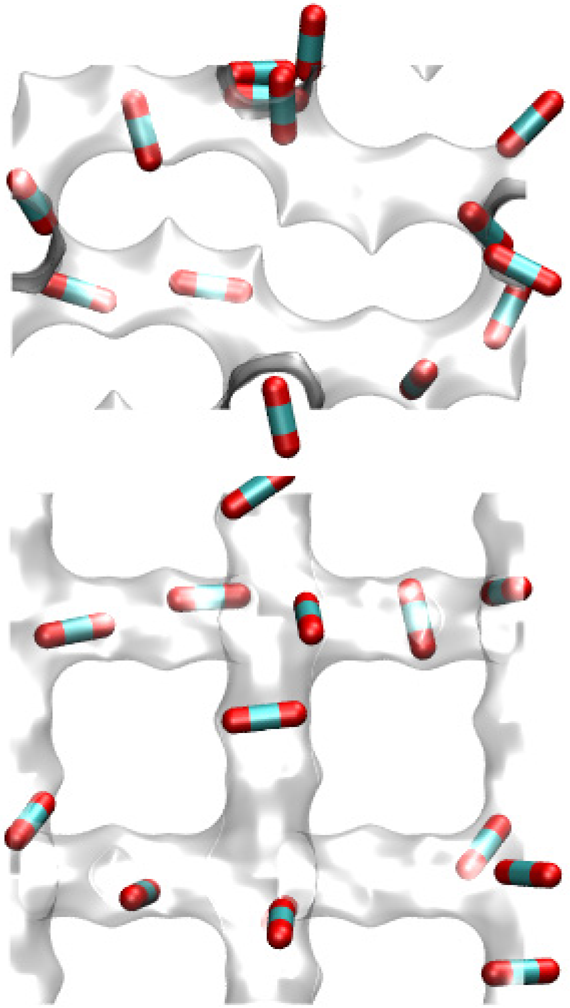

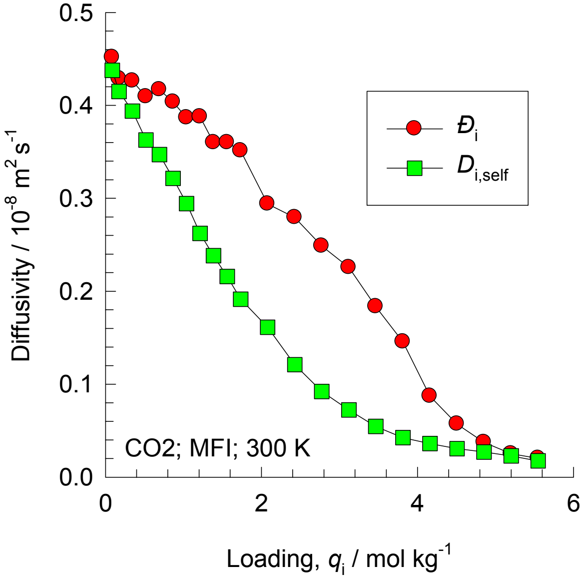

Diffusivity / 10^{-8} m^2 s^{-1}
0.0
0.1
0.2
0.3
0.4
0.5
0
2
4
6
Loading, q_i / mol kg^{-1}
$Đ_i$
$D_{i,self}$
CO2; MFI; 300 K

MFI, 300 K, N2

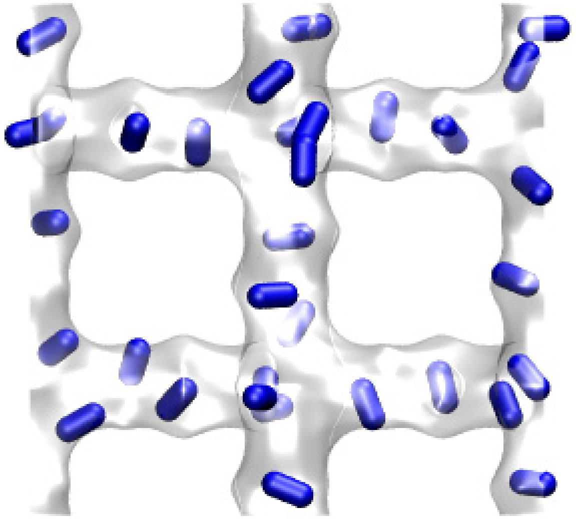

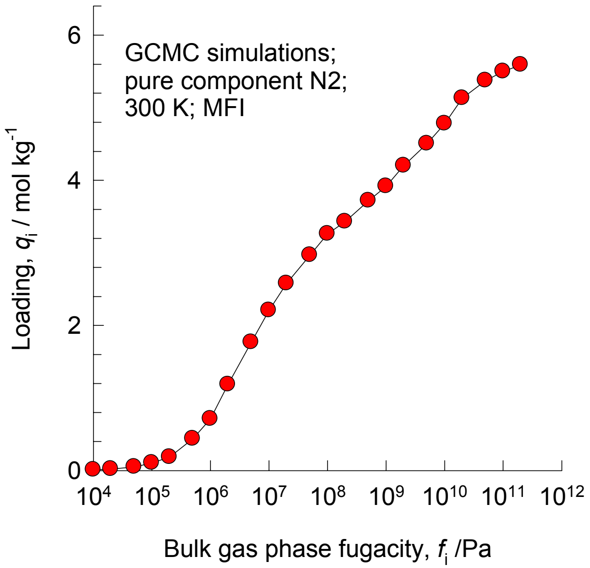
GCMC simulations;
pure component N2;
300 K; MFI
Loading, q_i / mol kg^{-1}
0
2
4
6
10^4
10^5
10^6
10^7
10^8
10^9
10^{10}
10^{11}
10^{12}
Bulk gas phase fugacity, f_i /Pa

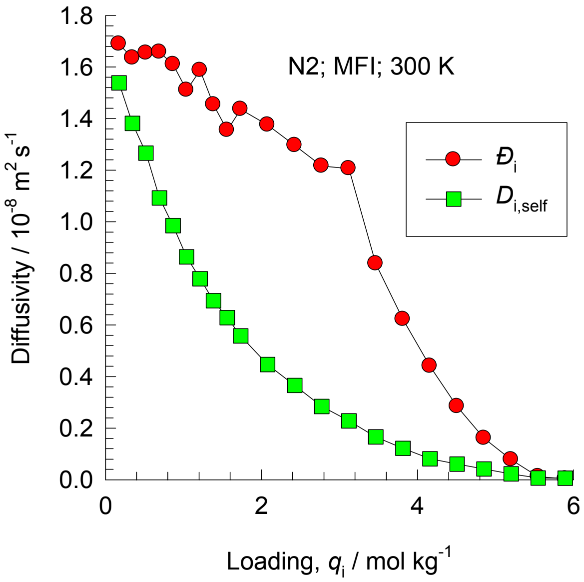
N2; MFI; 300 K
$Đ_i$
$D_{i,self}$
Diffusivity / 10^{-8} m^2 s^{-1}
0.0
0.2
0.4
0.6
0.8
1.0
1.2
1.4
1.6
1.8
0
2
4
6
Loading, q_i / mol kg^{-1}

MFI, 300 K, Ar

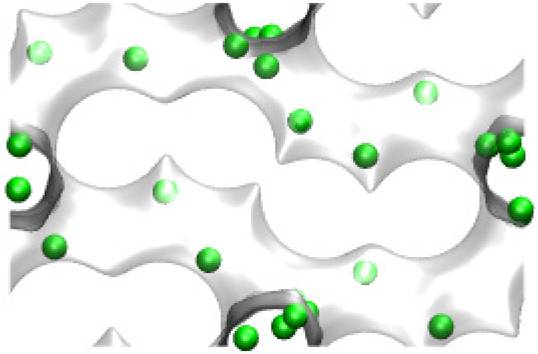

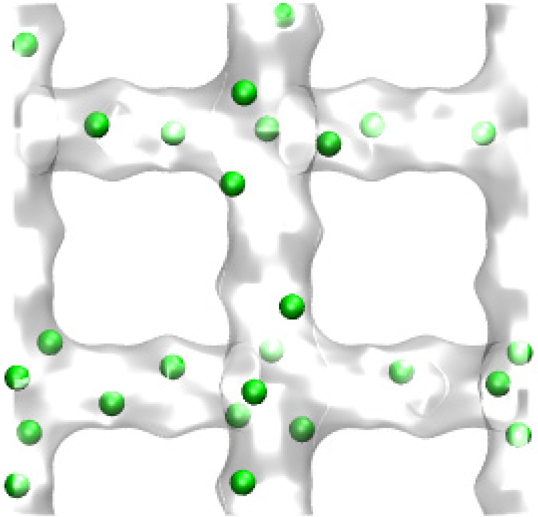

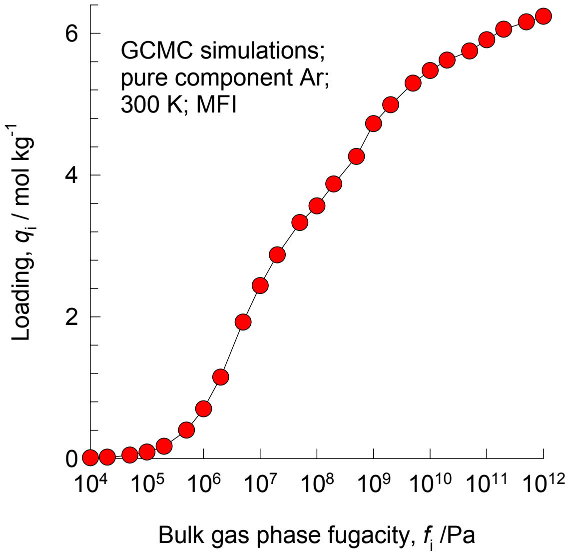
GCMC simulations;
pure component Ar;
300 K; MFI
Loading, q_i / mol kg^{-1}
0
2
4
6
10^4
10^5
10^6
10^7
10^8
10^9
10^{10}
10^{11}
10^{12}
Bulk gas phase fugacity, f_i /Pa

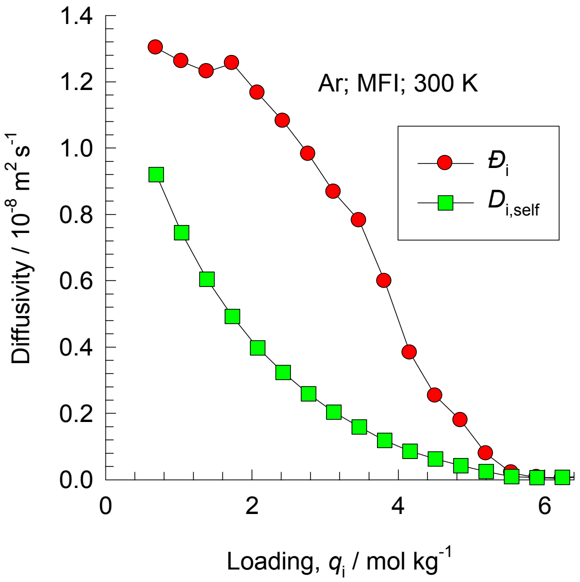
Ar; MFI; 300 K
Đ$_i$
$D_{i,self}$
Diffusivity / 10^{-8} m^2 s^{-1}
0.0
0.2
0.4
0.6
0.8
1.0
1.2
1.4
0
2
4
6
Loading, q_i / mol kg^{-1}

MFI, 300 K, Kr

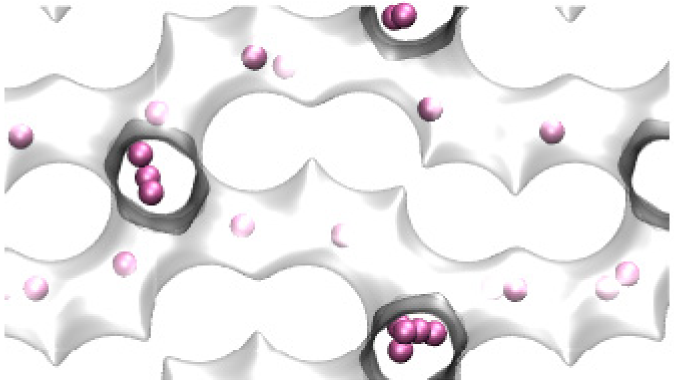

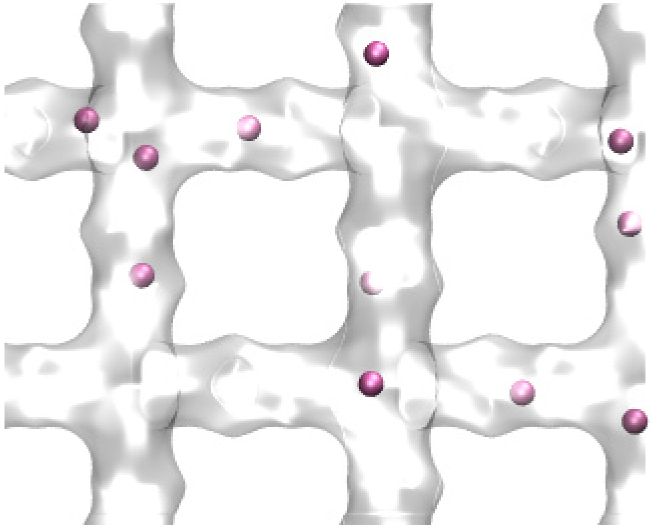

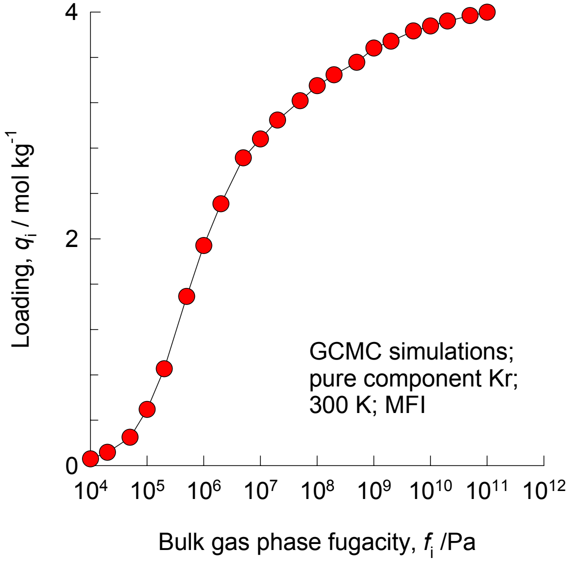
GCMC simulations;
pure component Kr;
300 K; MFI
Loading, q_i / mol kg^{-1}
Bulk gas phase fugacity, f_i /Pa
0
2
4
10^4
10^5
10^6
10^7
10^8
10^9
10^{10}
10^{11}
10^{12}

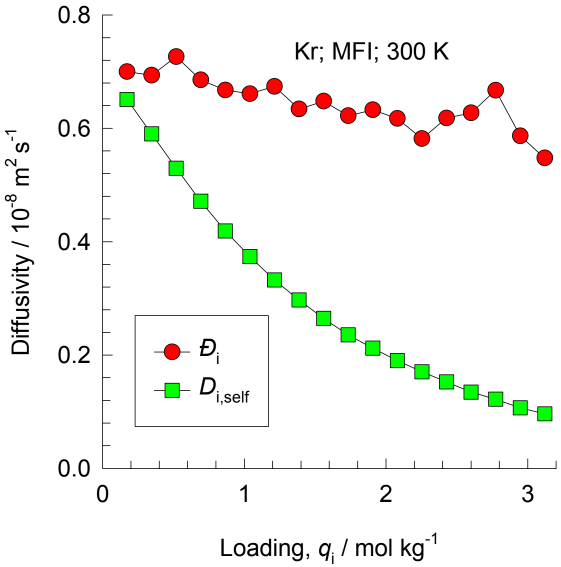
Kr; MFI; 300 K
Diffusivity / 10^{-8} m^2 s^{-1}
Loading, q_i / mol kg^{-1}
$Đ_i$
$D_{i,self}$
0.0
0.2
0.4
0.6
0.8
0
1
2
3

MFI, 300 K, Ne

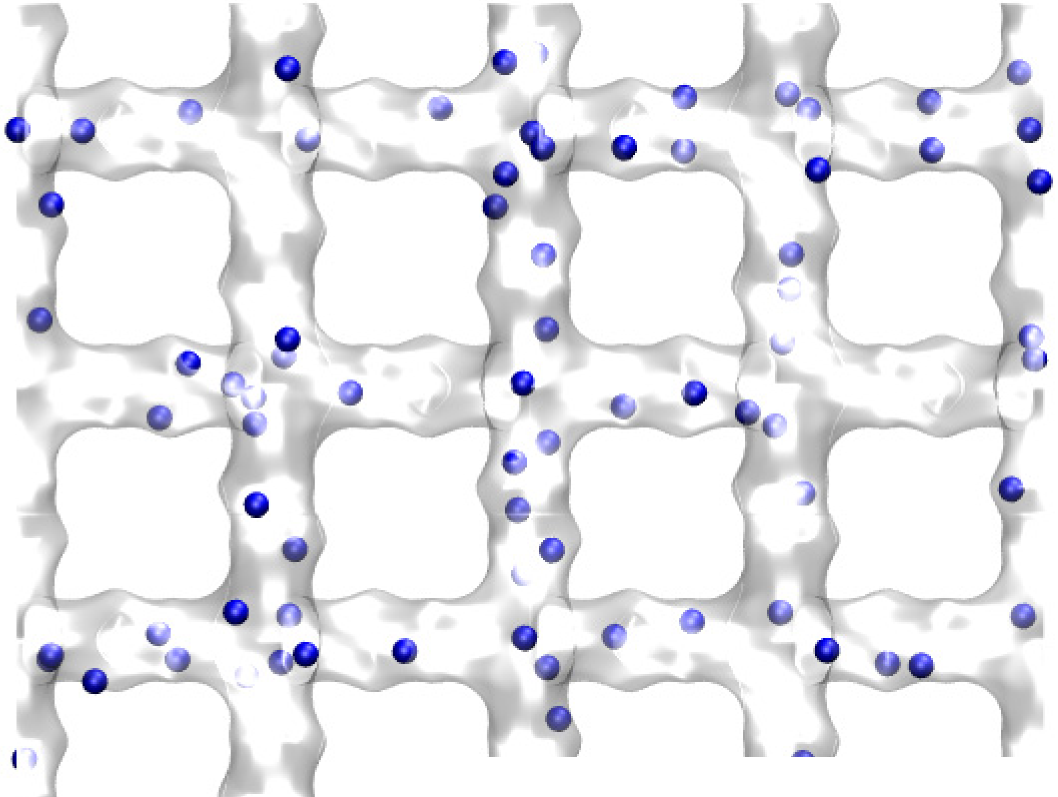

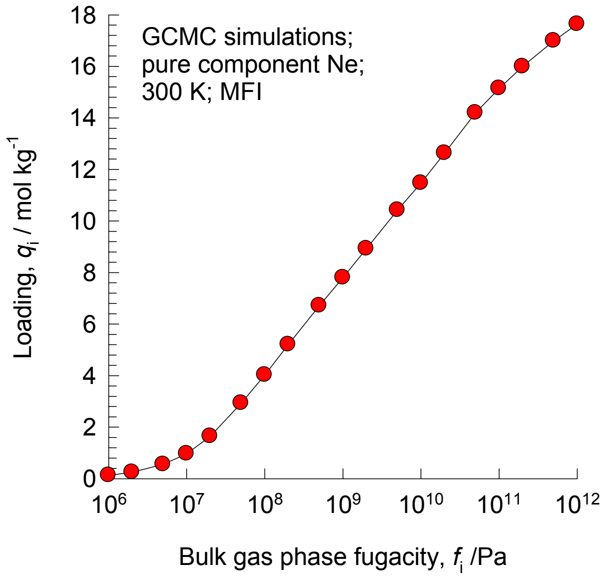
GCMC simulations;
pure component Ne;
300 K; MFI
Loading, q_i / mol kg^{-1}
0
2
4
6
8
10
12
14
16
18
10^6
10^7
10^8
10^9
10^{10}
10^{11}
10^{12}
Bulk gas phase fugacity, f_i /Pa

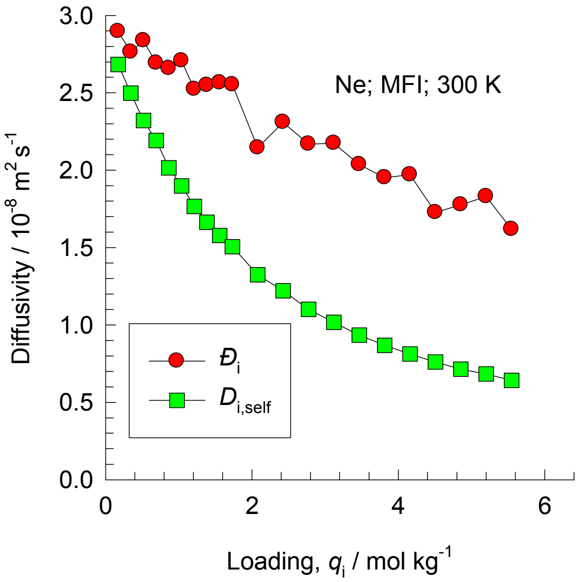
Ne; MFI; 300 K
Diffusivity / 10^{-8} m^2 s^{-1}
0.0
0.5
1.0
1.5
2.0
2.5
3.0
0
2
4
6
Loading, q_i / mol kg^{-1}
$Đ_i$
$D_{i,self}$

MFI, 300 K, He

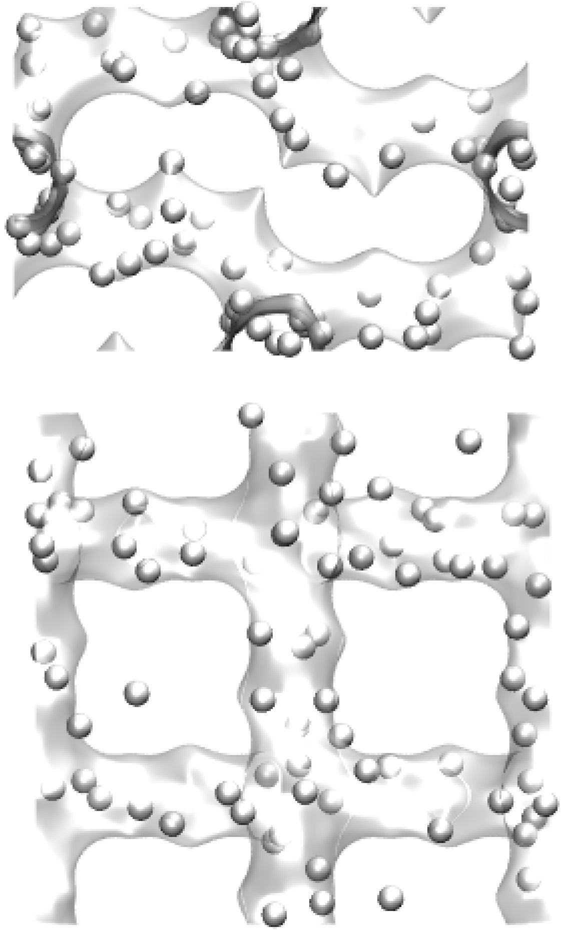

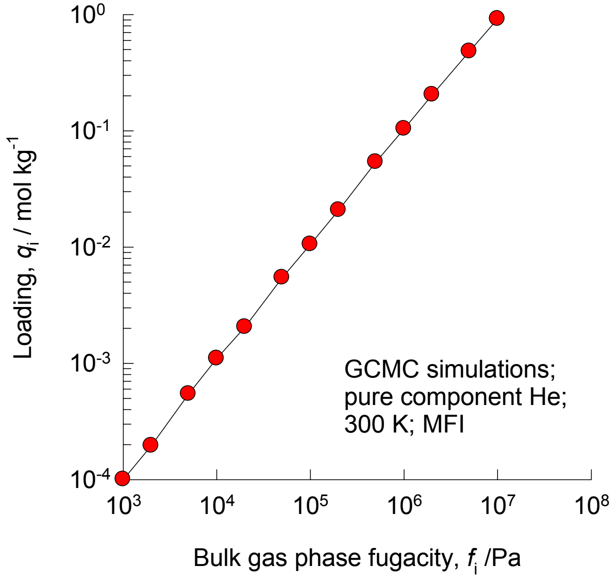

10^0
10^{-1}
10^{-2}
10^{-3}
10^{-4}
Loading, q_i / mol kg^{-1}
10^3
10^4
10^5
10^6
10^7
10^8
Bulk gas phase fugacity, f_i /Pa
GCMC simulations;
pure component He;
300 K; MFI

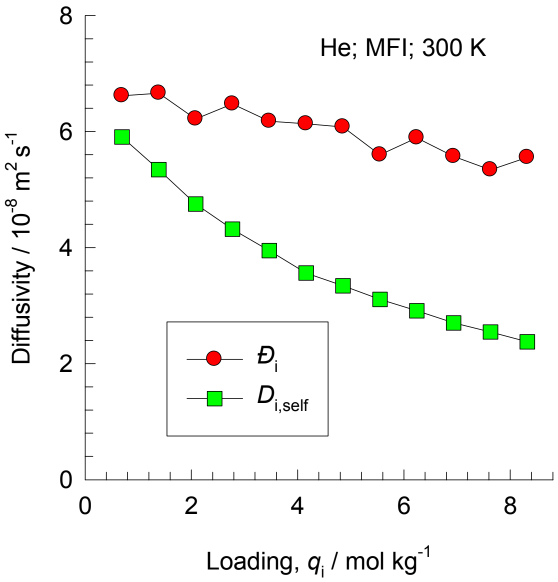

He; MFI; 300 K
Diffusivity / 10^{-8} m^2 s^{-1}
0
2
4
6
8
Loading, q_i / mol kg^{-1}
$Đ_i$
$D_{i,self}$

MFI, 300 K, H2

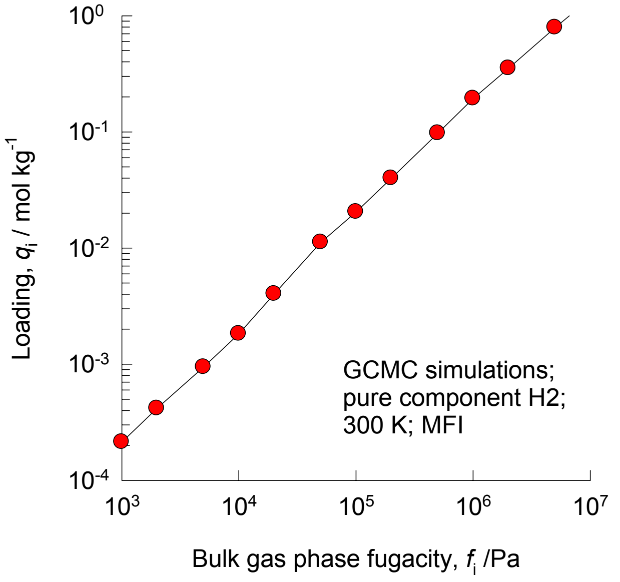

10^0
10^{-1}
10^{-2}
10^{-3}
10^{-4}
Loading, q_i / mol kg^{-1}
10^3
10^4
10^5
10^6
10^7
Bulk gas phase fugacity, f_i /Pa
GCMC simulations;
pure component H2;
300 K; MFI

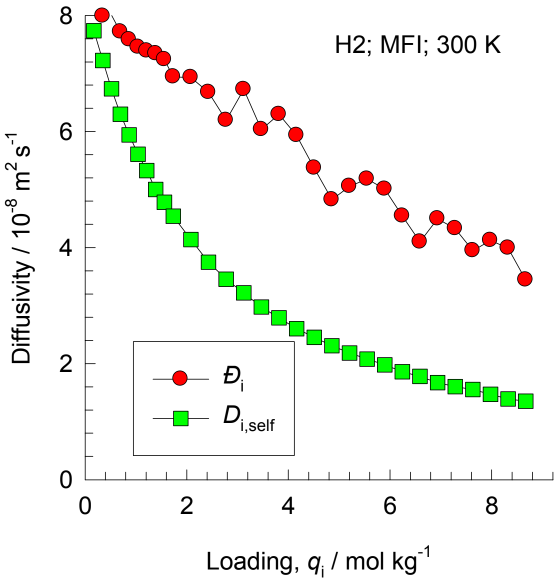

H2; MFI; 300 K
8
6
4
2
0
Diffusivity / 10^{-8} m^2 s^{-1}
0
2
4
6
8
Loading, q_i / mol kg^{-1}
$Đ_i$
$D_{i,self}$

Appendix A3

MD mixture diffusion simulations

Ar-Ne mixtures at 300 K; Self-diffusivities

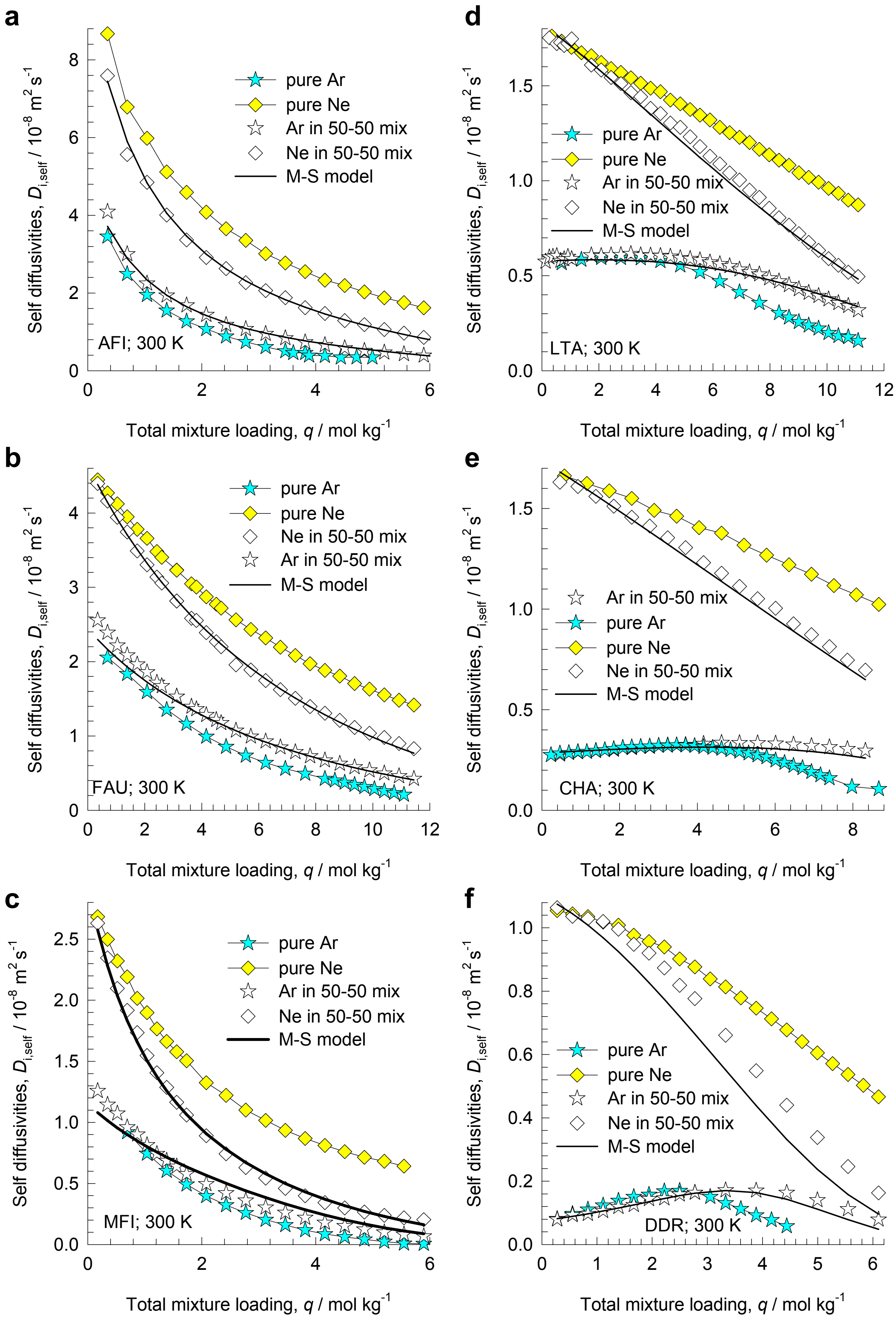

Ar-Ne mixtures at 300 K; M-S diffusivities

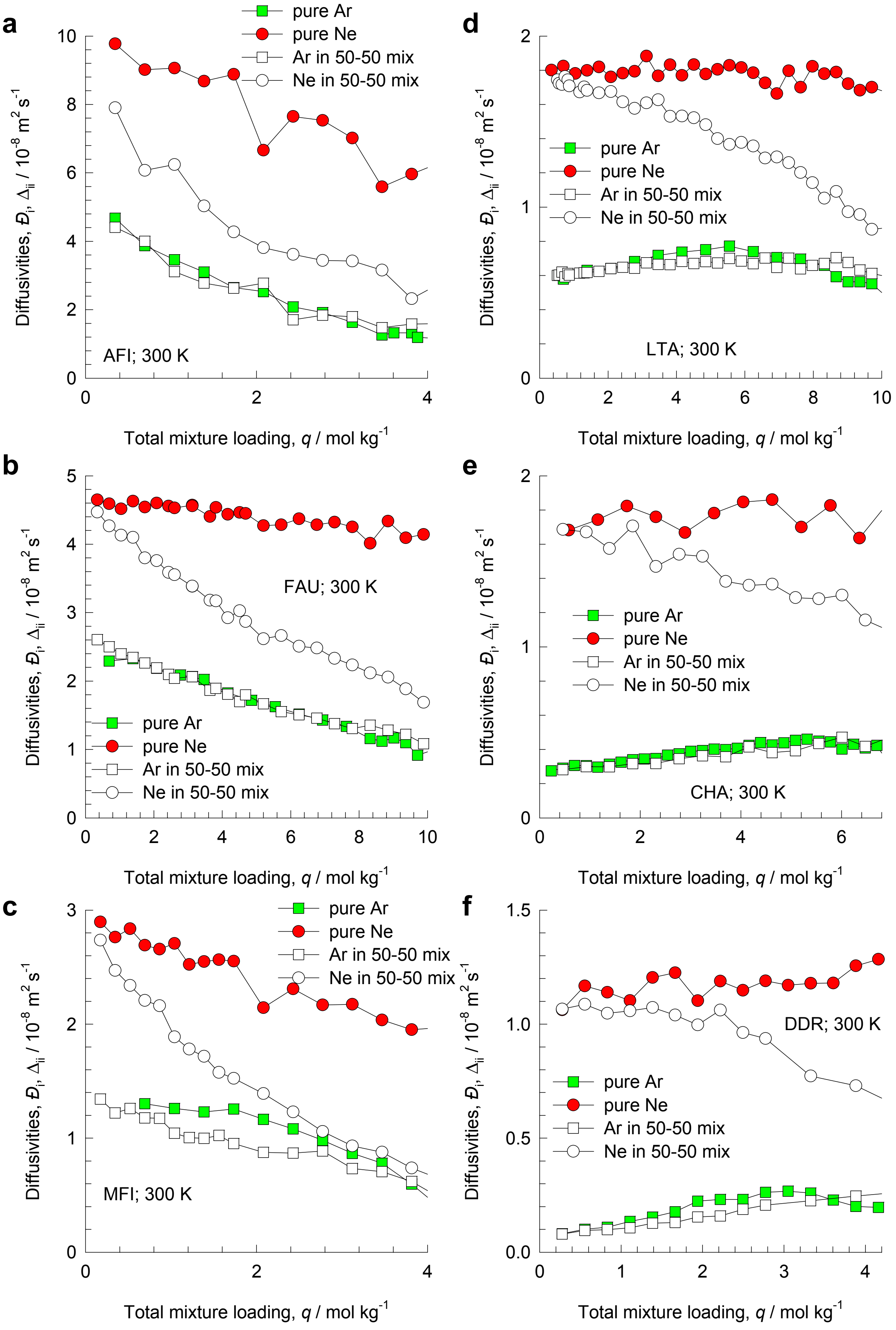

C1-Ar mixtures at 300 K; Self-diffusivities

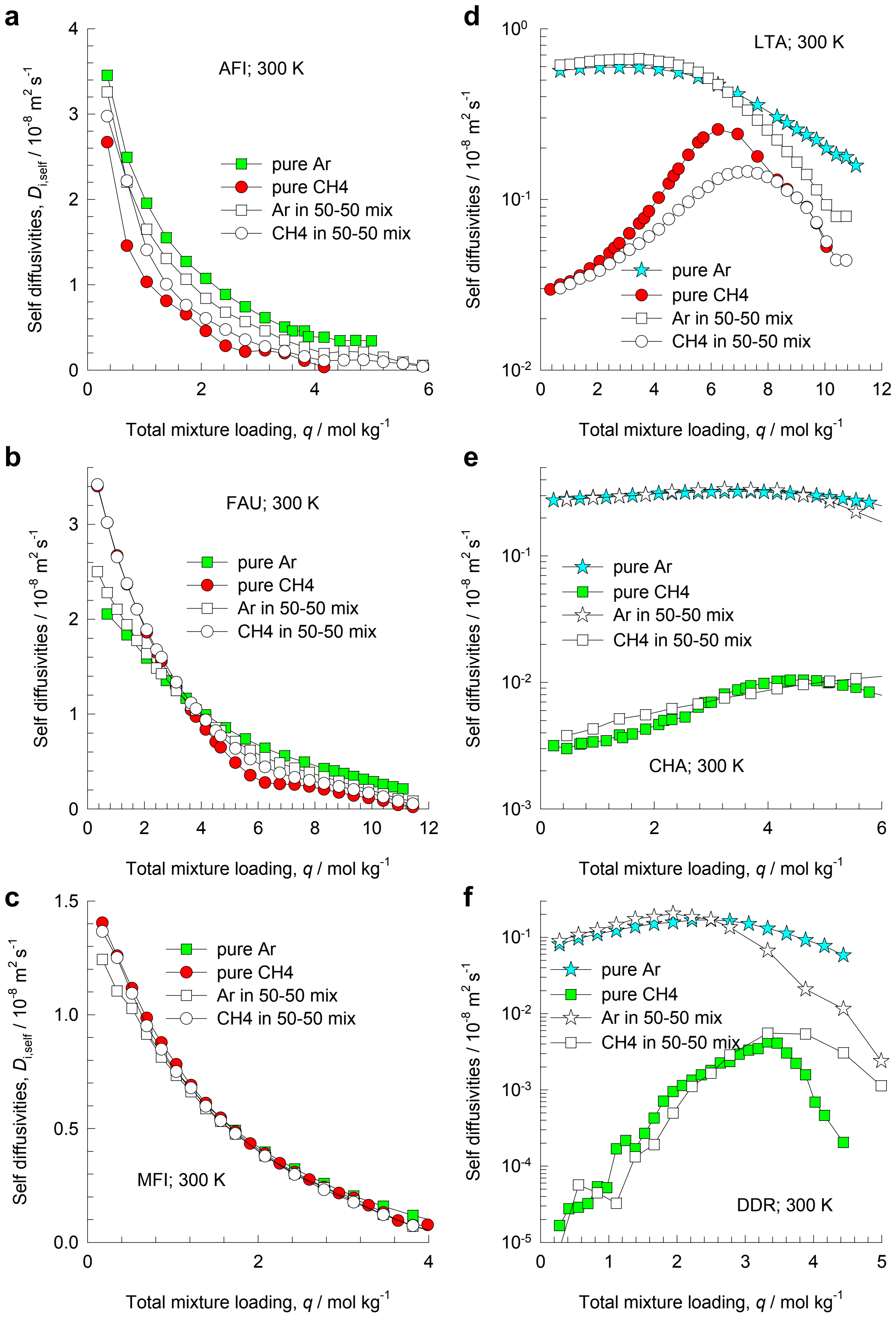

C1-Ar mixtures at 300 K;
M-S diffusivities

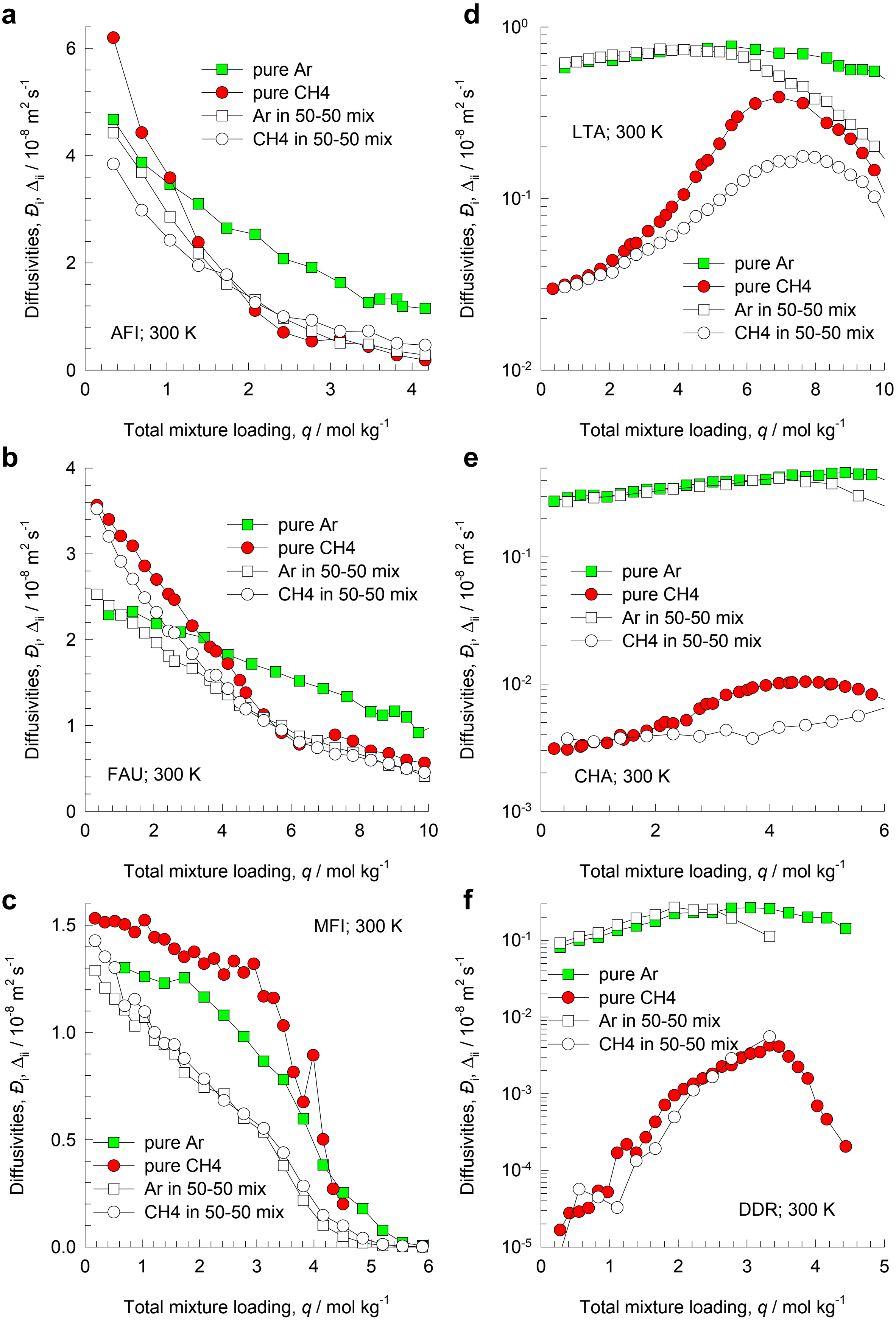

Ar-Kr mixtures in LTA at 300 K; Self and M-S diffusivities

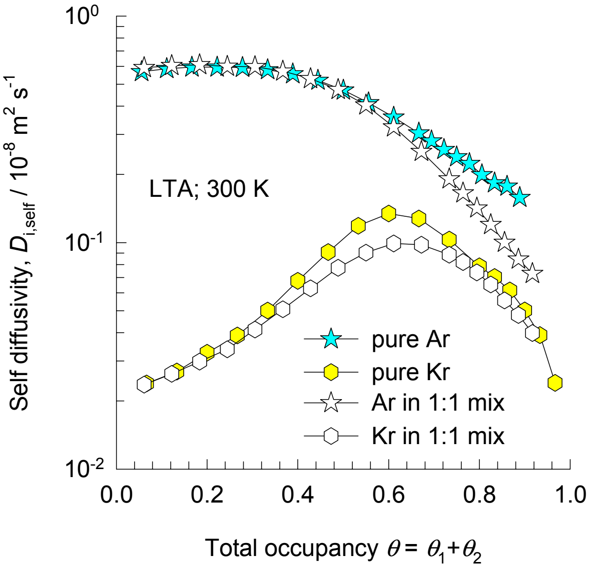

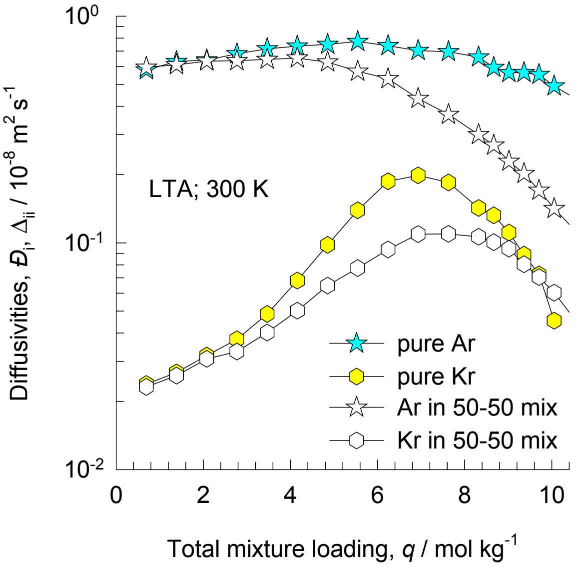

CH4-CO2 mixtures at 300 K; Self-diffusivities

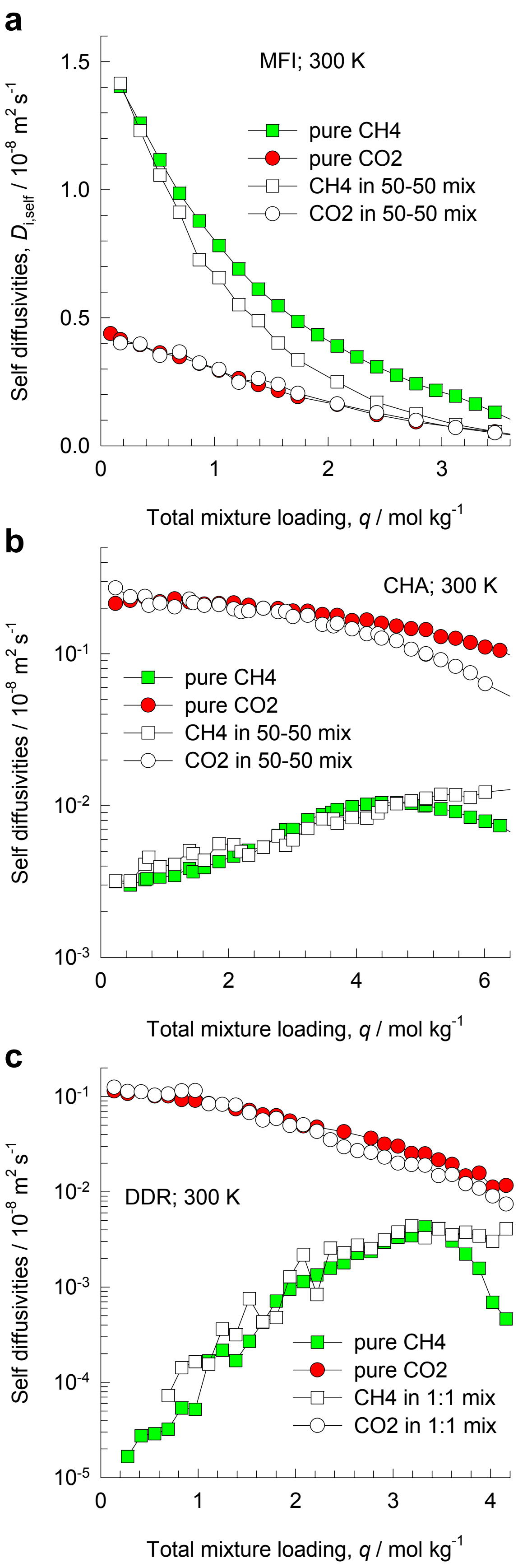

CH4-CO2 mixtures at 300 K; M-S diffusivities

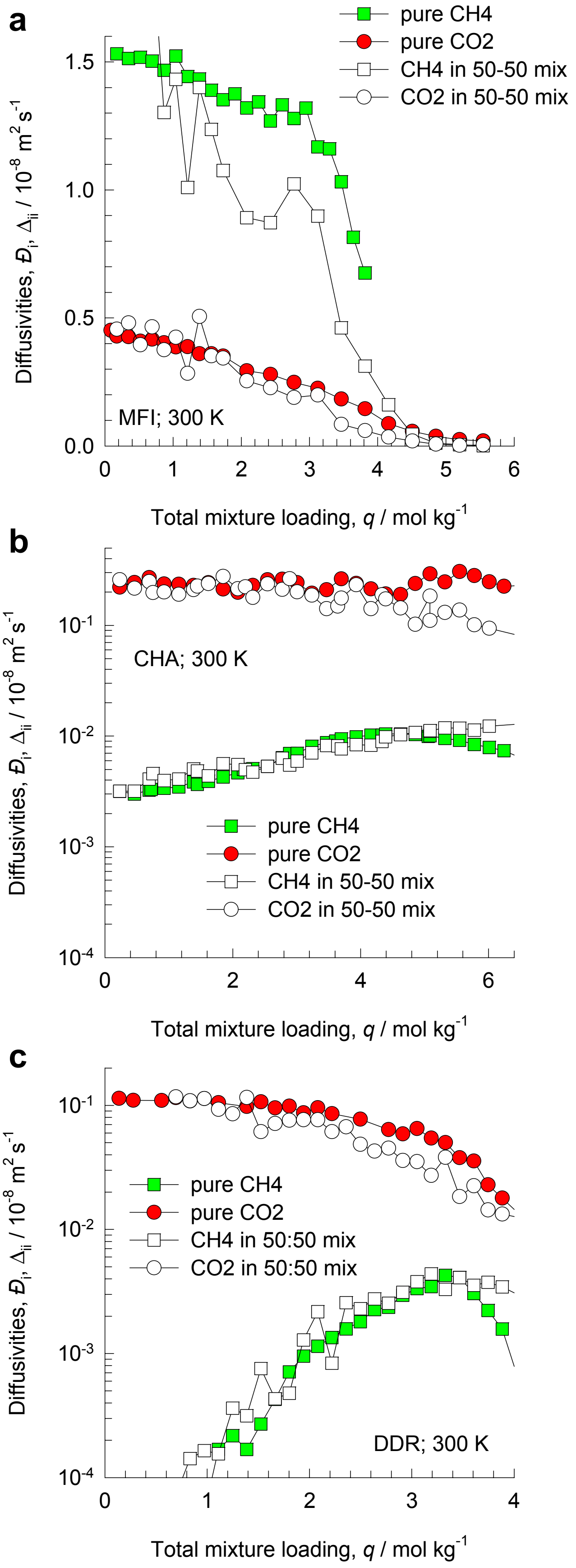

CO2-H2 mixtures at 300 K; Self-diffusivities

a

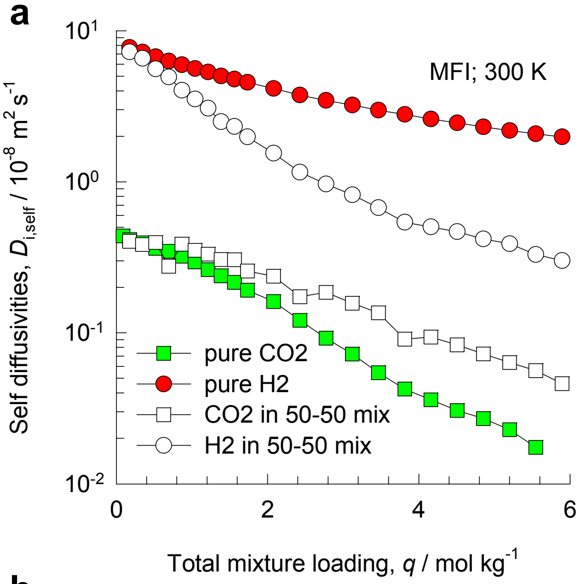

b

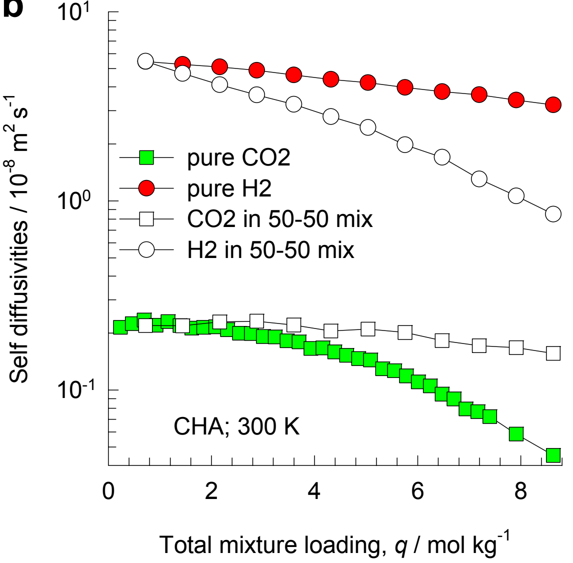

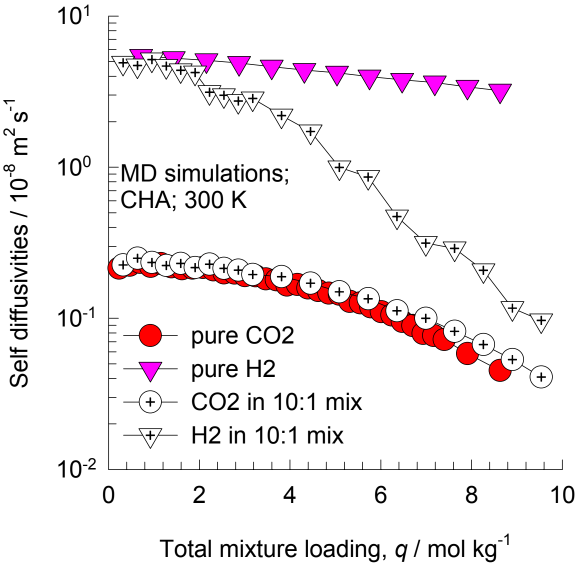

c

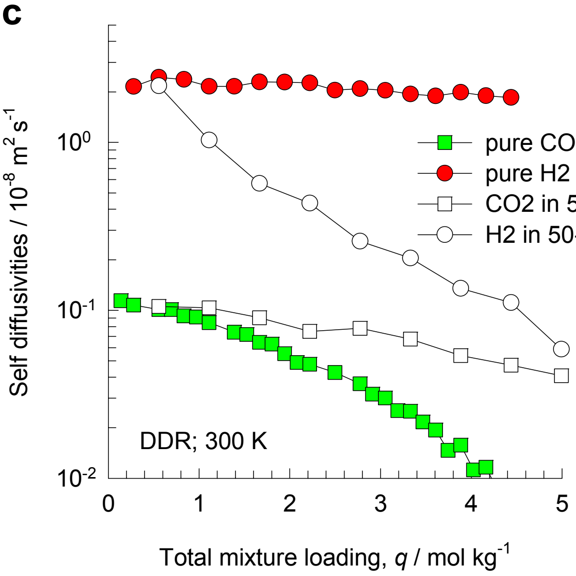

CO2-H2 mixtures in CHA at 300 K;
M-S diffusivities

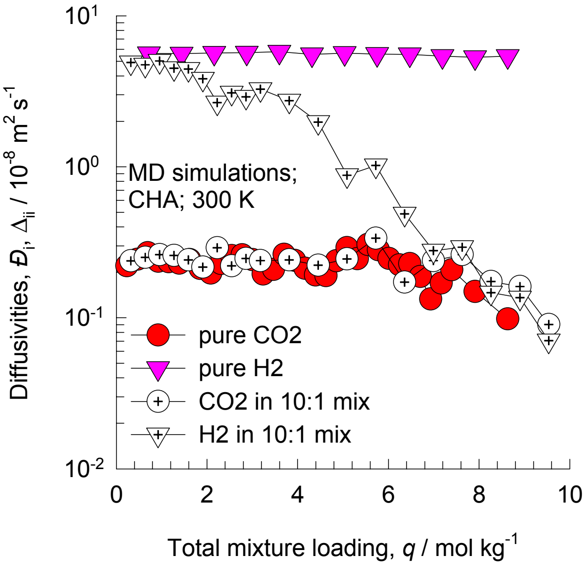

CH4-H2 mixtures at 300 K; Self-diffusivities

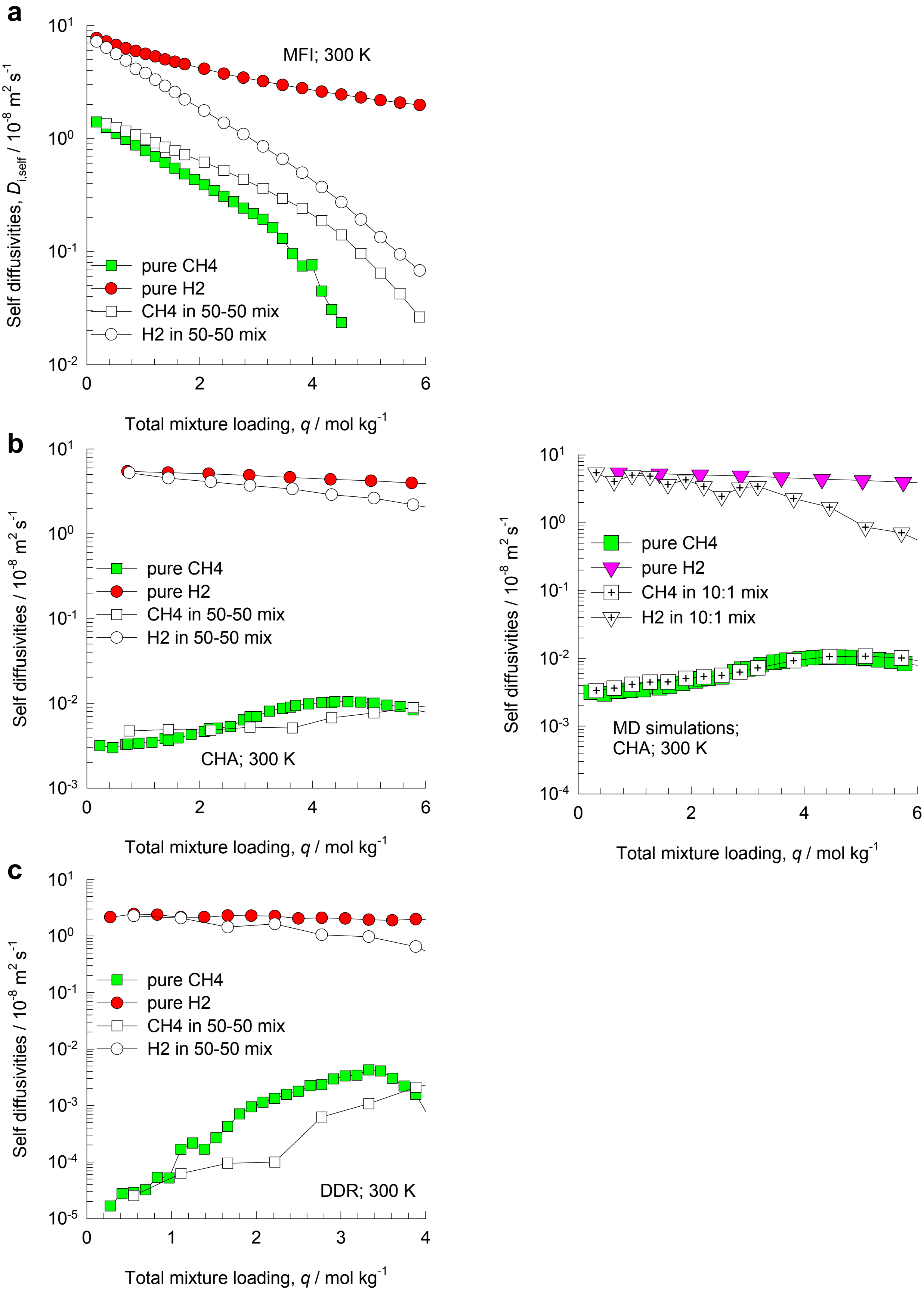

CH4-H2 mixtures at 300 K; M-S diffusivities

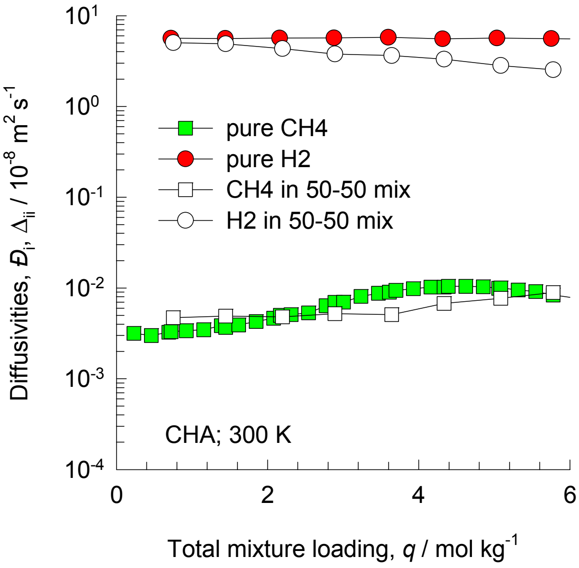

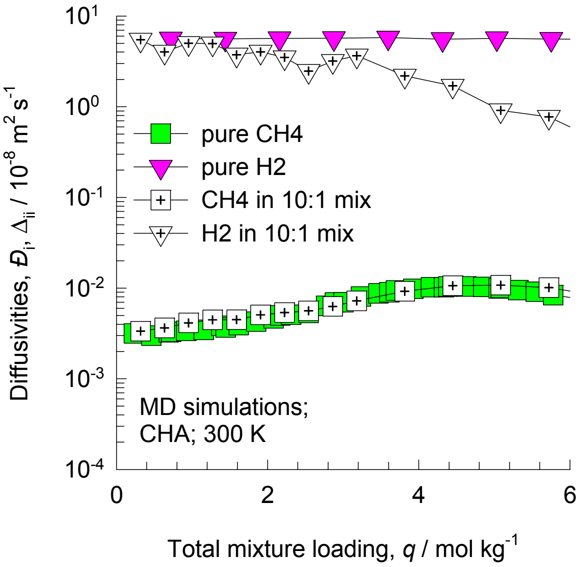

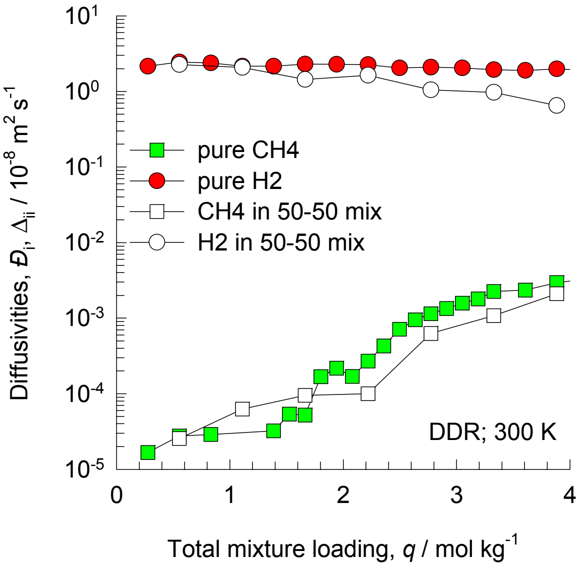

N2-H2 mixtures in CHA at 300 K; Self-diffusivities

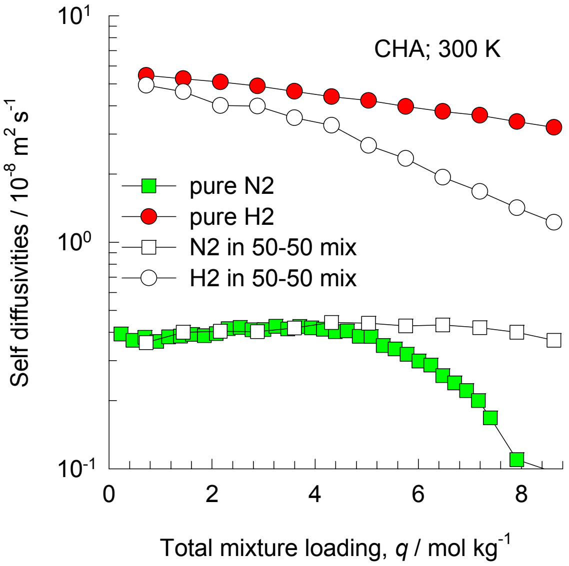

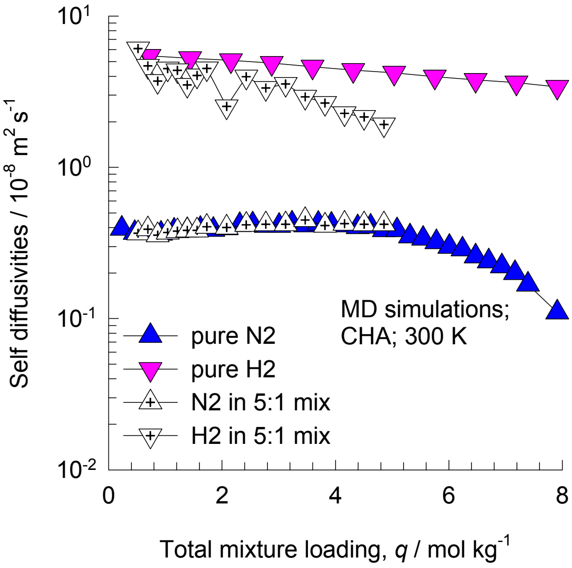

N2-H2 mixtures in CHA at 300 K; M-S diffusivities

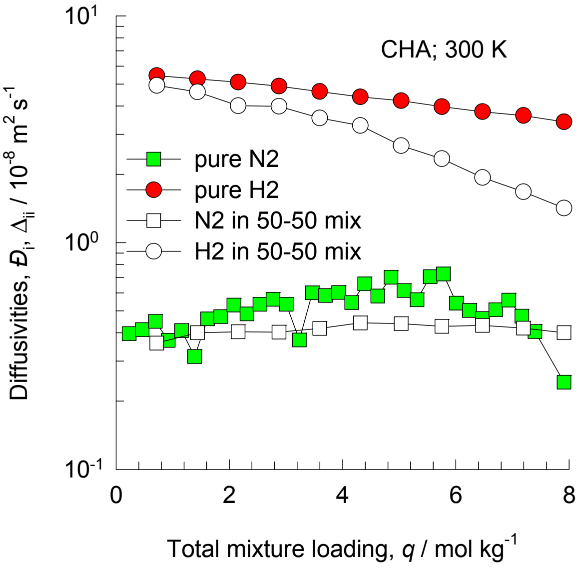

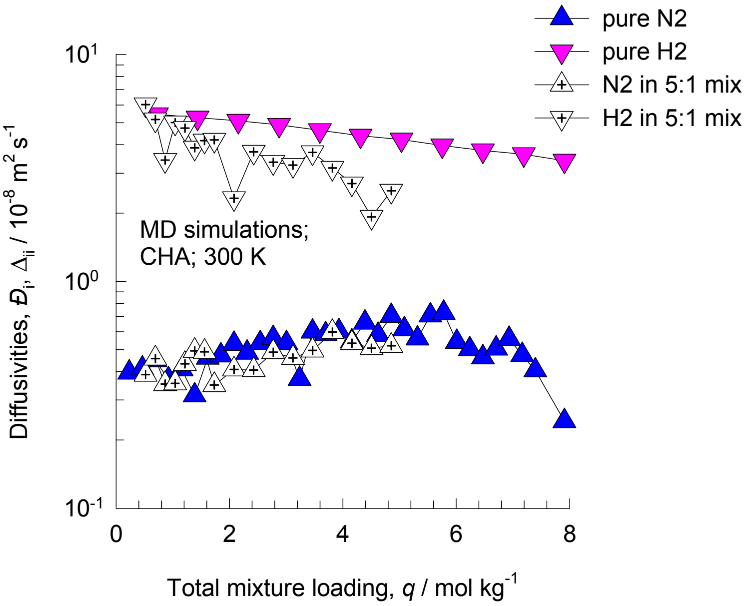

CH4-He mixtures in MFI at 300 K; Self-diffusivities

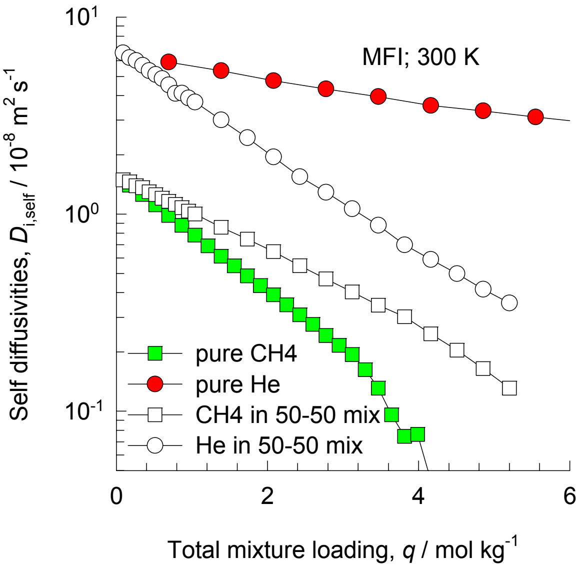

CH4-He mixtures in MFI at 300 K; Self-diffusivities Various mixture compositions

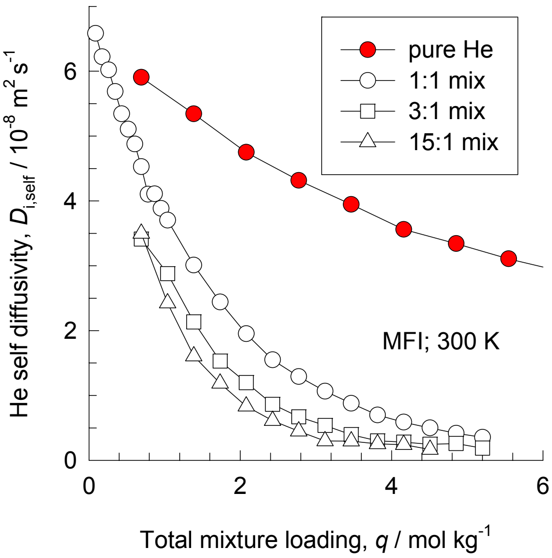

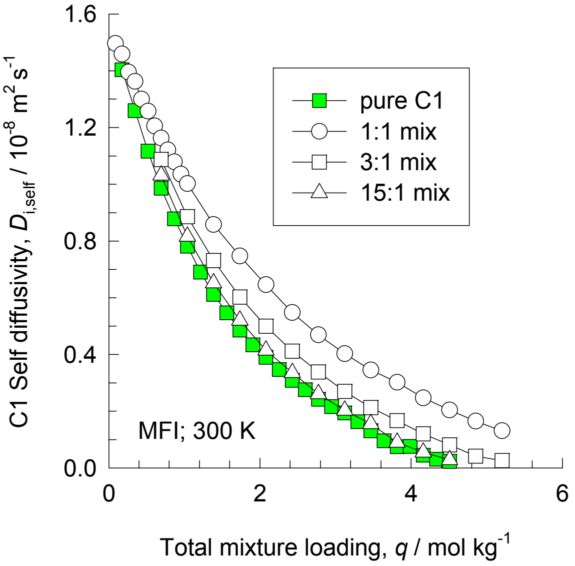

CH4-N2 mixtures at 300 K; Self-diffusivities

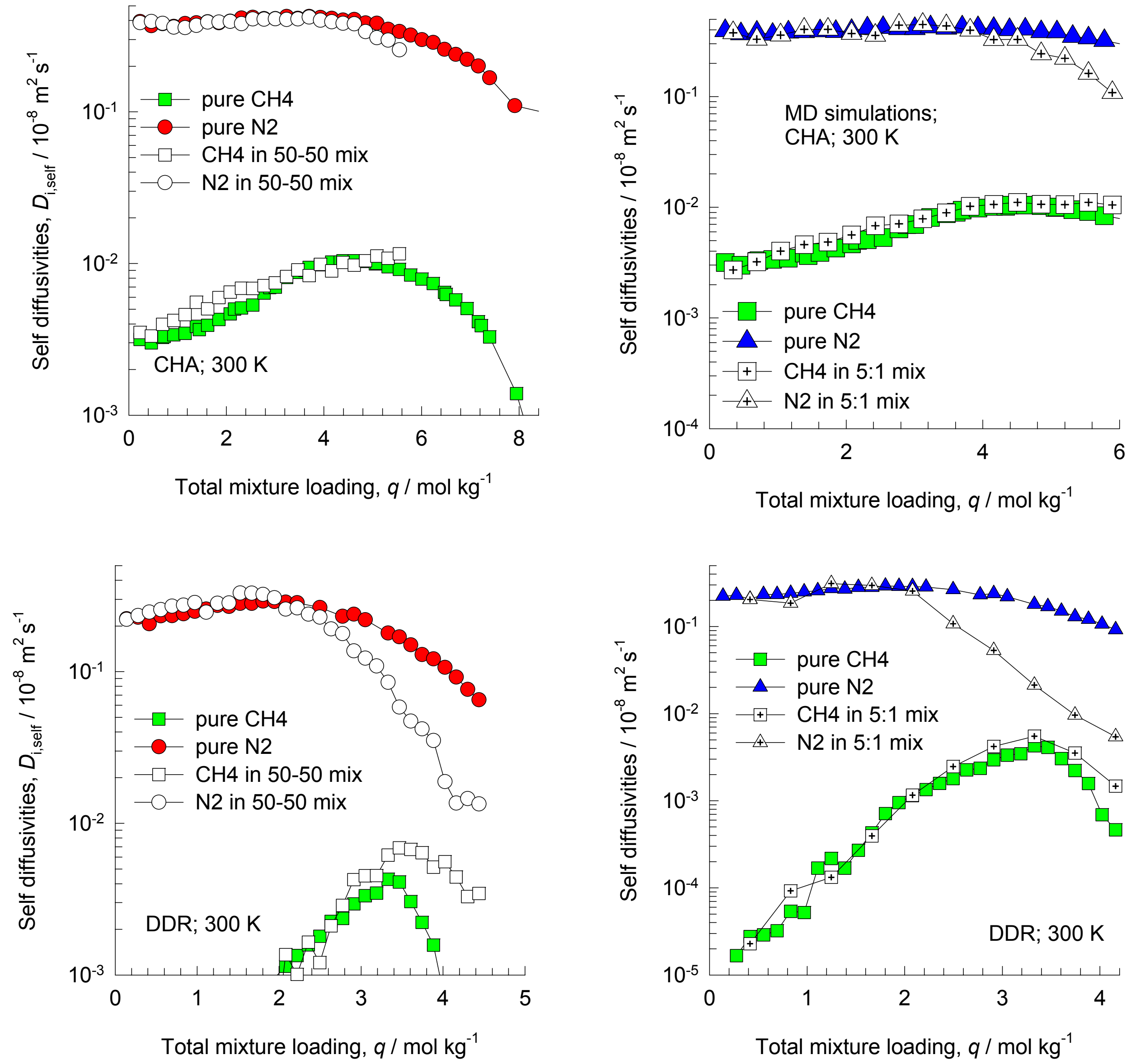

CH4-N2 mixtures at 300 K; M-S diffusivities

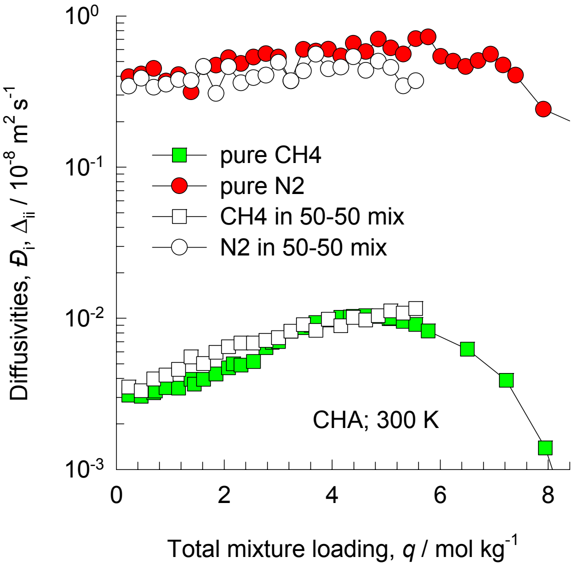

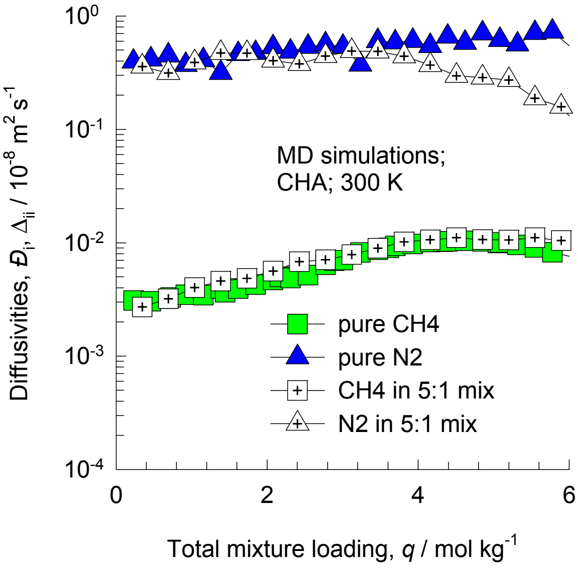

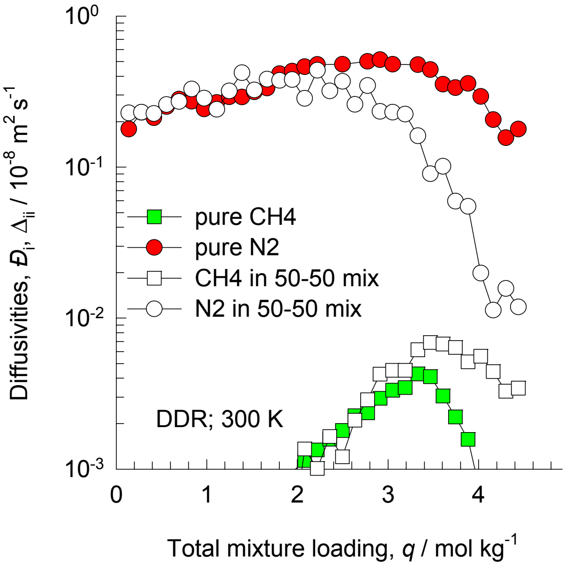

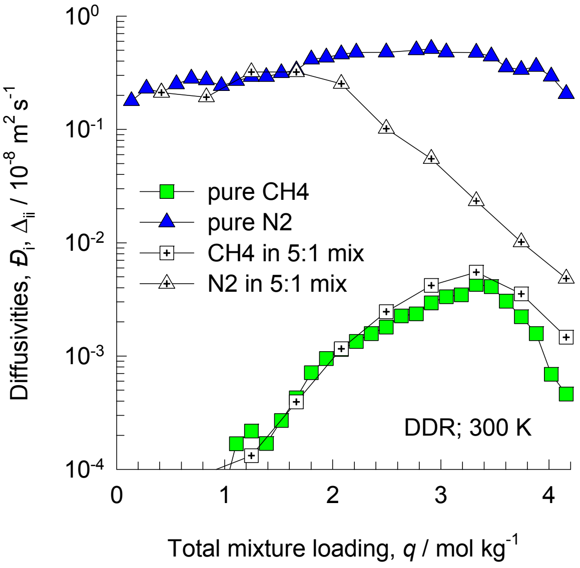

CO2-N2 mixtures in CHA at 300 K; Self- and M-S diffusivities

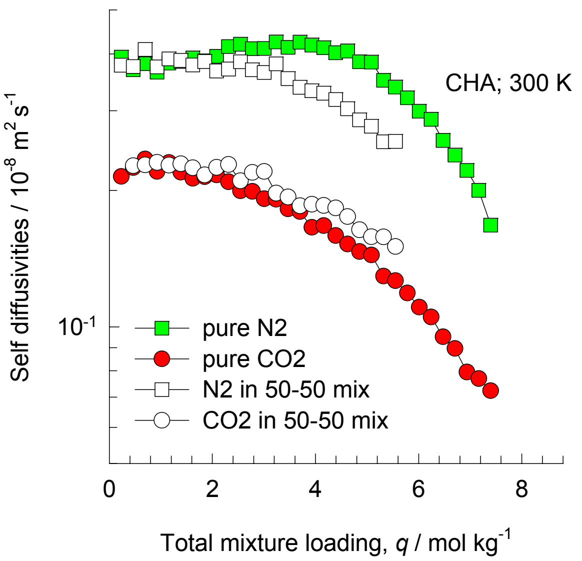

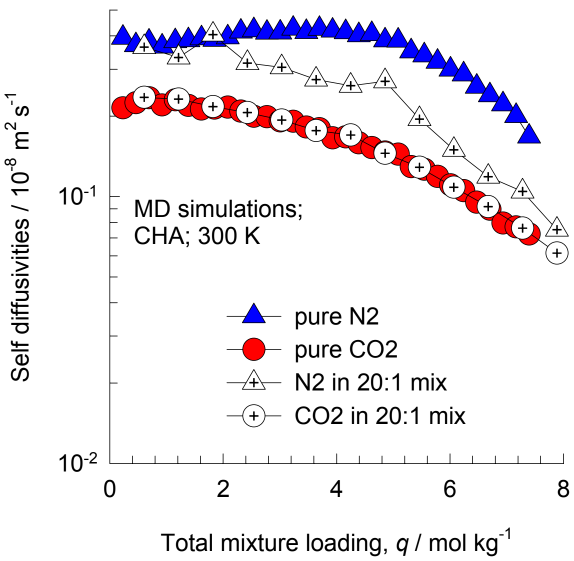

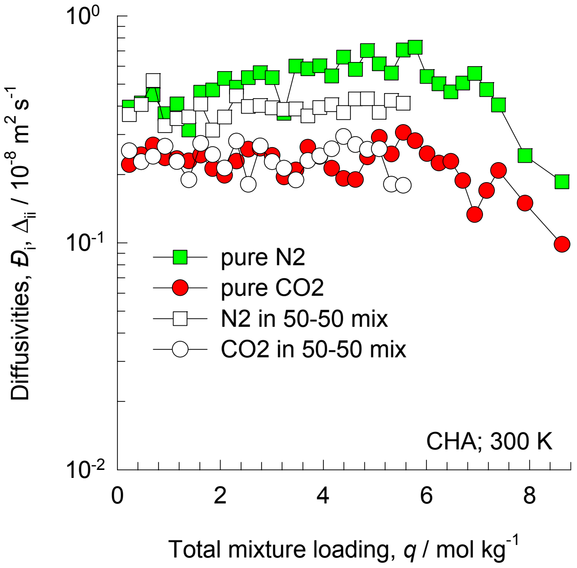

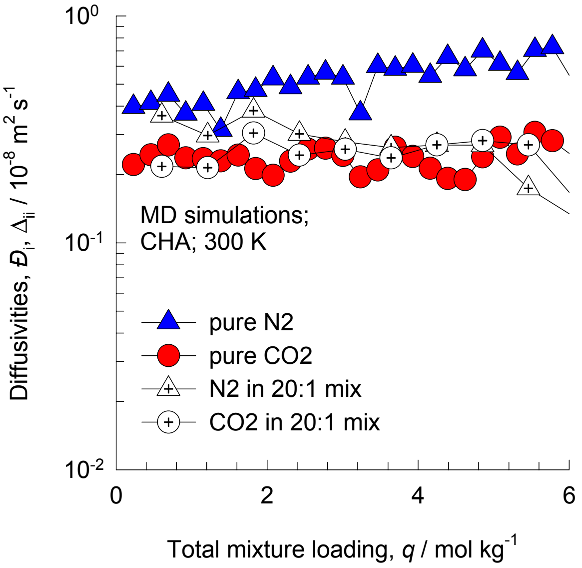

Ar-H2 mixtures at 300 K; Self-diffusivities

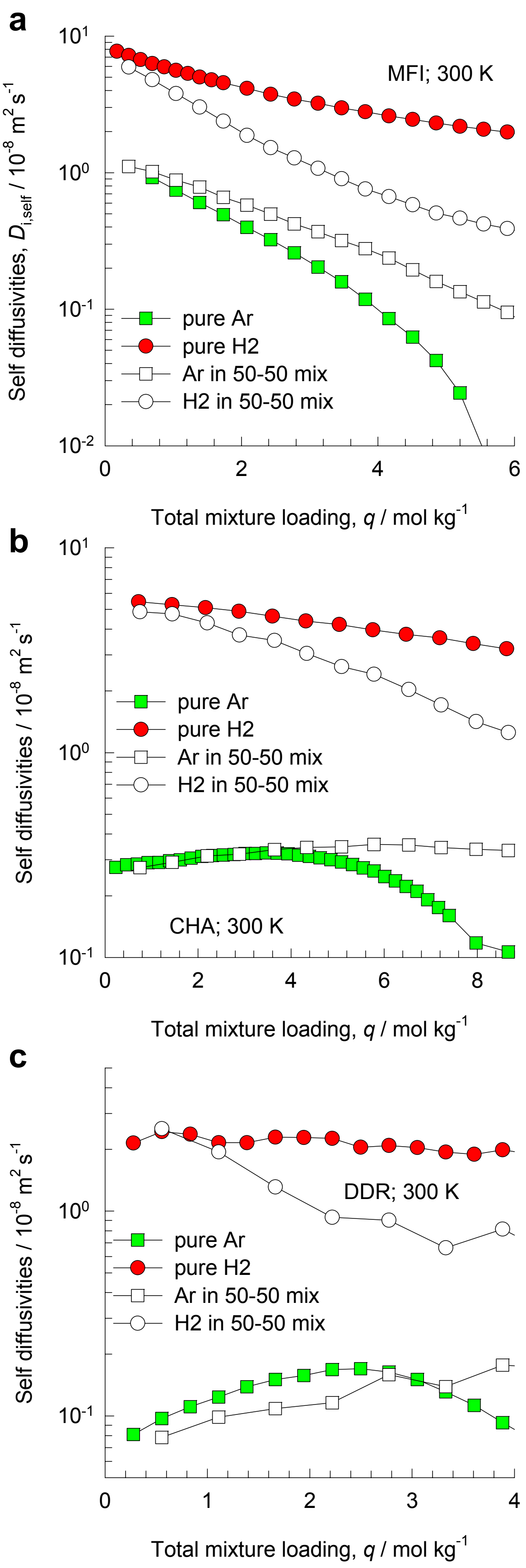

Ar-H2 mixtures at 300 K; M-S diffusivities